School of Molecular and Life Sciences
Department of Chemistry

"Turning A New Leaf"

Development of Spectroscopic Protocols to Study Plant Health

Karina Khambatta

0000-0002-5012-4250

This thesis is presented for the Degree of

Doctor of Philosophy
Curtin University

Declaration

Declaration To the best of my knowledge and belief this thesis contains no material previously published by any other person except where due acknowledgment has been made.

This thesis contains no material which has been accepted for the award of any other degree or diploma in any university.

Signature:

Date: 12/12/2022

Abstract

With an increasing global population, it is important to ensure crop health to provide global food security. Plants are susceptible to several different threats including plant disease and environmental stressors such as soil degradation and rising temperatures associated with climate change. This thesis hopes to address differences seen in plant health, through monitoring and diagnosis of chemical changes that occur as a result of environmental threats.

The wax coating on the surface of plant leaves (epicuticular waxes) holds important physiological functions to protect against plant disease and other environmental stresses. The wax layer is dynamic, changing in chemical and physical properties in response to disease or stress. Studying the composition and distribution of epicuticular waxes on the surface of leaves can, therefore, provide valuable insight into plant fitness and the presence of environmental stressors. Current methods to study plant waxes require extraction of the wax from the leaf surface. This approach reveals substantial insight into chemical composition of plant waxes; but destroys valuable information relating to the spatial distribution of waxes on the leaf surface. The development of analytical methods that can directly image epicuticular waxes on leaves is therefore, sought after to complement existing bulk analyses.

In addition to the chemical composition of the epicuticular wax layer, the micro-nutrient composition of plant leaves can be an important indicator of plant health, e.g., diffusible ions (K^+, Cl^-, Ca^{2+}) and transition metals (Fe, Mn, Cu, Zn). Although bulk levels assessment of these micro-nutrients has been extensively studied in the past, only recently has X-ray fluorescence microscopy made possible *in situ* imaging, which can associate elemental distribution with anatomical features of the leaf. The ability to develop microscopy protocols to study both epicuticular waxes on the leaf surface and also elemental composition of leaves, has much potential to increase our understanding of chemical pathways of crop disease.

Yellow spot is a major fungal disease of wheat impacting grain quality and yield, globally. In Western Australia, yellow spot can cause yield losses of up to 30%. Much research has gone into identification of pathogen secreted toxins and the removal of susceptibility genes from germplasm. However, under favourable conditions, the pathogen can cause major losses to yield. Therefore, improved chemical imaging

techniques offer the capability to better understand disease pathways, which is vital knowledge to subsequently develop strategies to mitigate the effects of disease on crop health.

The research within this PhD aimed to investigate and develop imaging methodology, incorporating infrared microscopy, and X-ray fluorescence microscopy, to gain insight into 1) dynamic response of epicuticular waxes as a result of physical and environmental changes, 2) enable study of mineral nutrient re-distribution during disease progression. In hope that it can then be used by the agricultural and environmental industry sectors to help monitor changes in plant health and fitness. The primary focus of this research was in the context of crop health, but application to preservation of native flora is also plausible.

Acknowledgements

I'd like to take this time to thank everyone who has supported me and been present throughout the duration of my time as a PhD student. For making what otherwise would not have been possible, possible.

A big thankyou to my supervisory team for all the support and insight you have provided me throughout my time. Thankyou Mark for teaching us the world of analytical chemistry and synchrotron science (dating back to undergrad), as well as taking a chance on a novel plant project, you helped me gain a lot of confidence when it came to things like presenting and I am very grateful. To Fatima, thank you for introducing me to the world of wheat and disease! I thoroughly enjoyed working alongside you and thank you for sharing your knowledge with me. To Alan, thankyou for providing us with the copious amounts of eucalyptus plants we used for analysis, as well as your guidance throughout synthesis and gassing segments. To Simon, yes... I know I'm surprised to, thankyou for your moral support throughout the years despite me not being a part of the forensic group you basically adopted me as one of your own. Your continuous check-ups and curiosity was greatly appreciated, alongside your ability as a teaching coordinator; made it a pleasure working alongside you.

To Pimm, Mark, David and Darryl, I'm very grateful for all the help and insight you have provided me, learning the ins and outs of a Synchrotron and being able to work alongside you all, you have definitely ignited one of my passions and interests! To Pimm, thankyou for being our synchrotron Mum, always going out of your way to take care of us and making sure we stay fed alongside all the dances and late-night shenanigans.

To Rhiannon and Ashley, I can't really say all that much here that you don't already know, I am super happy and grateful that I got to meet you both during our university life. Having two extremely loud, obnoxious, social, out there people to push me to the best of my abilities and out of my comfort zone as a little, quiet, and shy Karina are all experiences that I will carry along with me for time to come.

To Chappy and Tomoko, thankyou for being my tech support whether it be with instruments, or teaching labs; but, more importantly for all the conversations regarding life experiences, and associated laughs.

To my family, thank you for the support during the entirety of my university journey. A special thankyou to Mum for always making sure I had tea and food in me despite my own self neglect at times, I can't thank you enough for all you have done. To Dad thanks for providing me with the energy needed to keep on going, and always looking out for me. To Varun, thanks for being the annoyance that you are, I appreciate the late-night gym sessions that we had, and thank you for being a role model in more ways than you realise.

To my stream community, for all the laughs and trolling alongside all the exercise redeems; an experience I will never forget and hopefully continue for a time to come. Zoe, thank you for all the games, beach walks, star gazing, bingsu and resulting laughter (even if it got messy) that we've gotten to share, there's never a dull moment with you around, appreciate you a lot! To Cait, I wouldn't have been able to do any of this if it wasn't for you, you have been a tremendous help in more ways than one and I will be forever grateful.

Finally, I would like to acknowledge the support of the Australian Institute of Nuclear Science and Engineering (AINSE) for the post-graduate research award as well as the Australian Government for providing me a research training program stipend to fund this research.

Publications

This dissertation contains work which has been published in the following peer reviewed journals:

Karina Khambatta, Ashley Hollings, Georgina Sauzier, Lilian M.V.P. Sanglard, Annaleise R. Klein, Mark J. Tobin, Jitraporn Vongsvivut, Mark R. Gibberd, Alan D. Payne, Fatima Naim, Mark J. Hackett (2021) "Wax On, Wax Off": In Vivo Imaging of Plant Physiology and Disease with Fourier Transform Infrared Reflectance Microspectroscopy *Wiley Advance Science*

DOI: https://doi.org/10.1002/advs.202101902

Fatima Naim, Karina Khambatta, Lilian M.V.P. Sanglard, Georgina Sauzier, Julianne Reinhardt, David J. Paterson, Ayalsew Zerihun, Mark J. Hackett, Mark R. Gibberd (2021) Synchrtron X-ray fluorescence microscopy-enabled elemental mapping illuminated the 'battle for nutrients' between plant and pathogen *Journal of Experimental Botony*

DOI: https://doi.org/10.1093/jxb/erab005

Jitraporn Vongsvivut, David Perez-Guaita, Bayden R. Wood, Philip Heraud, Karina Khambatta, David Hartnell, Mark J. Hackett, Mark J. Tobin (2018) Synchrotron macro ATR-FTIR microspectroscopy for high-resolution chemical mapping of single cells *Analyst*

DOI: https://doi.org/10.1039/C8AN01543K

Contribution of Others to Publications from this Thesis

I, Karina Khambatta, contributed conceptualisation, investigation, methodology, visualisation, writing-original draft, writing-review & editing to the following paper:

"Wax On, Wax Off": In Vivo Imaging of Plant Physiology and Disease with Fourier Transform Infrared Reflectance Microspectroscopy

Advanced Science: **https://doi.org/10.1002/advs.202101902**

Karina Khambatta, Ashley Hollings, Georgina Sauzier, Lilian M. V. P. Sanglard, Annaleise R. Klein, Mark J. Tobin, Jitraporn Vongsvivut, Mark R. Gibberd, Alan D. Payne, Fatima Naim, and Mark J. Hackett

I as a Co-Author, endorse that this level of contribution by the candidate indicated above is appropriate.

Ashley Hollings	Signatures redacted for public use
Georgina Sauzier	
Lilian M. V. P. Sanglard	
Annaleise R. Klein	
Mark J. Tobin	
Jitraporn Vongsvivut	
Mark R. Gibberd	
Alan D. Payne	
Fatima Naim	
Mark J. Hackett	

Contribution of Co-Authors:

Dr Mark Hackett, Dr Fatima Naim, Dr Alan. D. Payne: assisted with the editing of this thesis. Dr Mark Tobin, Dr Jitraporn Vongsvivut, Dr Annaleise Klein, and Dr Mark Hackett: assisted with training on the synchrotron beamlines that were used to collect data for this thesis. Dr Mark Hackett and Peter Chapman: assisted with training on benchtop IR instruments.

I, Karina Khambatta, contributed conceptualisation, investigation, methodology, and editing of:

Synchrotron X-ray fluorescence microscopy-enabled elemental mapping illuminated the 'battle for nutrients' between plant and pathogen

Journal of Experimental Botany: **https://doi.org/10.1093/jxb/erab005**

Fatima Naim, Karina Khambatta, Lilian M V P Sanglard, Georgina Sauzier, Juliane Reinhardt, David J Paterson, Ayalsew Zerihun, Mark J Hackett, Mark R Gibberd

This was an interdisciplinary paper, my specific contribution was design/data/collection/data analysis, interpretation, and scientific writing of the specific components of this paper that related to analysis of K^+ and Ca^{2+} levels in plants (not transition metals). Only the portions of this manuscript relating to K^+ and Ca^{2+} will appear in my thesis.

I as a Co-Author, endorse that this level of contribution by the candidate indicated above is appropriate.

Fatima Naim	Signatures redacted for public use
Lilian M V P Sanglard	
Georgina Sauzier	
Juliane Reinhardt	
David J Paterson	
Ayalsew Zerihun	
Mark J. Hackett	
Mark R Gibberd	

Contribution of Co-Authors:

Dr Fatima Naim: Primary author, developed samples, analysis of transition metals, Dr Lilian Sanglard: Responsible for generation of samples, Dr Georgina Sauzier: Assistance with literature review and project planning, Dr David Paterson: Training and assistance with XFM data collection and analysis, Dr Ayalsew Zerihum: Conceptual design, paper editing, Dr Mark Hackett: Supervision, advice on data analysis, editing, Professor Mark Gibberd: Conceptual design, expertise on wheat disease.

I, Karina Khambatta, contributed cover photo, conceptualisation, investigation, methodology, visualisation, and writing of "3.4 Surface chemistry of Eucalyptus leaf" for the following paper. The paper is multidisciplinary, including experiments on red-blood cells, brain cells, and also physical characterisation of spatial resolution, and I did not contribute to those components, and they will not appear in my thesis. The only data from this paper that will appear in my thesis, is the work focussed on plant sciences, for which I had the lead role, as described above.

Synchrotron macro ATR-FTIR microspectroscopy for high-resolution chemical mapping of single cells

Analyst: **https://doi.org/10.1039/C8AN01543K**

Jitraporn Vongsvivut, David Pérez-Guaita, Bayden R. Wood, Philip Heraud, Karina Khambatta, David Hartnell, Mark J. Hackett, and Mark J. Tobin

I as a Co-Author, endorse that this level of contribution by the candidate indicated above is appropriate.

Jitraporn Vongsvivut	Signatures redacted for public use
David Pérez-Guaita	
Bayden R. Wood	
Philip Heraud	
David Hartnell	
Mark J. Hackett	
Mark J. Tobin	

Contribution of Co-Authors:

Dr Mark Hackett: supervision and advice during data analysis (plant and brain cells). Dr Mark Tobin, Dr Jitraporn Vongsvivut: assisted with training on the synchrotron beamlines, physical characterisation of optics. David Hartnell: Undertook brain cell experiments. David Pérez-Guaita, Bayden R. Wood, Philip Heraud: Undertook red blood cell experiments (sample preparation, data collection, data analysis).

Conference Presentations

Selected aspects of the work contained within this thesis have been presented at the following conferences:

2018 Australian Society of Molecular Imaging - Presentation
- Student Presentation Award

2018 Organic18 RACI (Royal Australian Chemical Institute) Organic Division - Poster

2018 Australian Synchrotron User Meeting - Presentation

2019 RACI R&D Topics - Presentation

2019 Fresh Scientist Program - Presentation
- Finalist Award

2019 Twitter Conference - Poster

2020 Australian Synchrotron User Meeting – Presentation and Video poster
- Poster Presentation Award
- Snapshot Presentation Award

2021 Australian Society of Molecular Imaging – Video presentation and Poster

2021 Australian Plant Pathology Society - Poster

Table of Contents

CHAPTER 1 Introduction 1

1.1 General Introduction 2

1.2.1 The role of Epicuticular Waxes in Plant Biology 4

1.2.2 Effects of Environmental Stress on Epicuticular Wax Function 5

1.2.3 Stomata and Their Function in Plants 6

1.2.4 Disease Induced Change to Epicuticular Wax Layer 9

1.2.5 Mechanisms and Pathology of Pyrenophora tritici-repentis 9

1.3.1 Techniques to Study Epicuticular Waxes – Bulk Methods 11

1.3.2 Techniques to Study Epicuticular Waxes – Imaging Methods 11

1.3.3 Basic Theory of Infrared Spectroscopy Techniques 12

1.3.4 Attenuated Total Reflectance – Fourier Transformed Infrared Spectroscopy 15

1.3.5 Synchrotron ATR-FTIR Microscopy 16

1.3.6 Infrared Reflectance Spectroscopy and Microscopy 17

1.4.1 Plant Metallomics 19

1.4.2 The Role of Specific Metal Ions in Maintaining Plant Health 21

1.4.3 Effects of Infection on Plant Metallomics 22

1.5.1 Analytical Techniques to Study Metals in plants 23

1.5.2 Synchrotron Infrastructure 23

1.5.3 Synchrotron X-Ray Fluorescence Microscopy 25

1.5.3.1 Energy Dispersive X-ray Detector 27

1.5.3.2 X-ray Focussing Optics 28

1.5.3.3 Wavelength Selection Optics 28

1.5.3.4 Vortex - Silicon Drift Detector 28

1.5.3.5 Confocal X-ray Imaging Optics 30

1.5.3.6 Confocal Imaging Capabilities 31

1.6 Overview and Aims.....31

CHAPTER 2 Experimental.....34

2.1 Introduction.....35

2.2 Plant Models Used to Develop and Test Spectroscopic Protocols for the Analysis of Epicuticular Waxes.....36

2.3 Model System to Investigate Flora Ripening on Epicuticular Wax.....36

2.4 Plant Models of Epicuticular Wax Changes during Crop Disease.....38

2.5 Chemical Extraction and Analysis of Epicuticular Waxes.....39

2.6 Optimisation of Sample Preparation and Tissue Sectioning Parameters.....40

2.7 General Optical and Fluorescent Microscopy Parameters.....42

2.8 Benchtop Attenuated Total Reflectance – Fourier Transformed Infrared Spectroscopic Analysis of Eucalyptus Leaves.....43

2.9 Analysis of Leaf Surfaces with Benchtop Fourier Transformed Infrared Reflectance Microscopy.....44

2.10 Analysis of Leaf Sections with Focal Plane Array FTIR Spectroscopic Imaging 47

2.11 Synchrotron Attenuated Total Reflectance – Fourier Transformed Infrared Spectroscopic Analysis of Leaf Surfaces.....48

2.12 Elemental Mapping of Intact Leaves and Leaf Sections with 2D (MAIA) and 3D (Vortex) X-ray Fluorescence Microscopy.....50

2.13 Scanning Electron Microscopy.....52

CHAPTER 3 A Proof of Concept: Detecting Epicuticular Wax Distribution Using Attenuated Total Reflectance – Fourier Transformed Infrared Techniques.....54

3.1 Introduction.....56

3.2 Results and Discussion.....58

3.2.1 Investigating the Capability of ATR-FTIR Spectroscopy to Detect Differences in Epicuticular Wax Composition in Four Eucalyptus Species.....58

3.2.2 Investigation of Epicuticular Waxes in Different Leaf Regions: A Comparison of ATR-FTIR Spectra Collected from Abaxial and Adaxial Leaf Surfaces 61

3.2.3 Investigation of Spectroscopic Differences in ATR-FTIR Spectra Collected from the Surface of Tuart Leaves at Different Stages of Leaf Maturation (Immature vs Mature) 64

3.3 Application of ATR-FTIR coupled to a Synchrotron Lightsource, to Reveal Sub-cellular Epicuticular Wax Distribution on Leaf Surfaces 65

3.4 Using Ether Extractions to Reveal Individual Waxes Present on the Surface of Epicuticular Waxes in Eucalyptus Leaves 71

3.5 Conclusions 72

CHAPTER 4 Development and Application of Fourier Transformed Infrared Reflectance Microspectroscopy to Investigate Epicuticular Wax Distribution on Leaf Surfaces 73

4.1 Introduction 74

4.2 Results and Discussion 76

4.2.1 Demonstrating the Experimental Limitations Associated with Imaging Leaf Tissue Sections with Fourier Transform Infrared Transmission Spectroscopy and Raman Microscopy 76

4.2.2 Development of a Non-destructive Imaging Method to Study Leaf Surfaces, using Fourier Transform Infrared Reflectance Microscopy 77

4.2.3 Investigating Different Metal Substrates as Background References for the Analysis of Leaf Surfaces with Fourier Transform Infrared Reflectance Microscopy 81

4.2.4 Studying Seasonal Variations in Fourier Transform Infrared Reflectance Spectra of Leaf Surfaces 83

4.2.5 Observed Variation in ex vivo Fourier Transform Infrared Reflectance Spectra Collected from Leaf Surfaces During Leaf Growth and Maturation. 85

4.2.6 Observed Variation in Fourier Transform Infrared Reflectance Spectra Collected from Leaf Surfaces During Leaf Growth and Maturation in vivo .87

4.2.7 Fourier Transform Infrared Reflectance Spectra of Ethylene Gassed Geraldton Wax 89

4.2.8 Fourier Transform Infrared Reflectance Spectra of Diseased Wheat Leaves During Progression of Fungal Infection 94

4.2.9 Fourier Transform Infrared Reflectance Spectra of Yellow Spot Infected Susceptible and Resistant Wheat Cultivars.....99

4.2.10 Fourier Transform Infrared Reflectance Spectra of Diseased Wheat Leaves Reveals Differences in Calcium Oxalate Accumulation in Wheat Infected with Ptr.....103

4.3 Conclusions.....107

CHAPTER 5 Using Synchrotron X-Ray Fluoresence Microscopy to Characterise Changes in Calcium and Potassium Distribution in Infected Wheat Leaves.....109

5.1 Introduction.....110

5.2 Results and Discussion.....113

5.2.1 Utilising XFM to Associate Changes Seen in Calcium Distribution During Wheat Infection.....113

5.2.2 Developing Rb+ XFM Tracing Protocols to Assess Changes to the Distribution of K+, as a Marker for Plant Disease Pathology 120

5.3 Conclusions.....127

CHAPTER 6 Conclusions and Future Work.....129

6.1 Conclusions.....130

6.2 Future Work.....132

6.2.1 Future Work to Increase the Chemical Specificity of FTIR Reflectance Analysis of Epicuticular Waxes.....132

6.2.2 Studying Effects of Fruit Ripening on Epicuticular Wax Layers Using FTIR Reflectance Methods 132

6.2.3 Investigating the Effects of Ptr on Different Calcium Compounds Using XANES 133

6.2.4 Using 3D Confocal XFM to Investigate Effects on K+ Using Rb+ as a Biomarker 133

7.0 References 134

8.0 Appendix 151

List of Figures

Figure 1: *Epicuticular wax composition throughout Rosa canina leaves, adopted from (3)* 4

Figure 2: *Cross-section schematic of the epicuticular wax layer of the outer most layer of plant cuticle, adopted from (5)*.....5

Figure 3: *Seasonal variation in epicuticular wax thickness on the adaxial and abaxial surfaces of Douglas-fir needles. (8)*.....6

Figure 4: *Schematic of Stomata and different cellular/sub-cellular compartments ...*7

Figure 5: *SEM images of different stomata shapes and sizes depending on plant species (left to right): Eucalyptus (tuart), wheat (cv Scout), wheat (cv Magenta). Scale bars - 10 and 20µm.* 7

Figure 6: *SEM images of Eucalyptus tuart, showing stomata cells being surrounded by wax, opening, and closing of guard cells due to electron beam exposure 10 µm, 50 µm and 200 µm scale.* 8

Figure 7: *SEM images of Pyrenophora tritici-repentis infected wheat (cv Scout) leaf section, 50 µm scale (left) and 100 µm scale (right)* 10

Figure 8: *Schematic representation of infrared wavelength regions ranging from far-infrared to near-infrared*.....12

Figure 9: *Different stretching and bending molecular vibrations. + indicates movement out of the plane while – indicates movement in. (35, 37)* 13

Figure 10: *Schematic representation of how FTIR spectrometer works*.....14

Figure 11: *Schematic representation of how Synchrotron ATR-FTIR works when sample is in contact*.....16

Figure 12: *Schematic depicting infrared transmission (red trace) and infrared reflectance (blue trace) when sample is in contact with source (specular reflection)* 17

Figure 13: *Important components and configuration of a modern synchrotron source. Schematic adapted from Wilmott et al. (114)*.....24

Figure 14: *Prototype magnets found at the Australian synchrotron storage ring, green and red magnets (red not imaged) help focus and steer the electrons while the large yellow one (located behind green magnet) are used for insertion devices which direct the electron flow via wigglers and undulators, maintaining the high intensity flux of light. (114, 117)*.....25

Figure 15: *Principles of X-Ray Fluorescence*.....26

Figure 16: *Visualisation of 2D MAIA Synchrotron XFM setup with whole wheat leaf samples red arrow indicating direction of x-ray beam*.....27

Figure 17: *Visualisation of Synchrotron XFM (vortex detector and 3D setup) with sectioned wheat leaf sample white arrow - indicating cryostat, green – vortex detector, red – mounted sample.* 30

Figure 18: *Schematic representation of 3D Vortex detector Synchrotron XFM setup* 31

Figure 19: *Molecular structure of common ethylene promoter; Ethephon* 38

Figure 20: *25 L containers being filled with Geraldton wax and ethylene solution/procedural blank solution (left) Geraldton wax places in flask with ethylene/procedural blank solution placed next to it (right).*.....38

Figure 21: *Image of wheat leaves fixed on to a flat platform with 10 uL inoculation of Ptr placed on the leaf surface (left) glasshouse with misting system in action (right)* 39

Figure 22: *Wheat embedded vertically on cryo-microtome sectioning mount (left), wheat embedded onto cryo-microtome mount with OCT embedding surrounding the tissue structure (right)*.....42

Figure 23: *tissue sections of wheat on silicon nitride chip (left) and microscope slide (right)* 43

Figure 24: *Spatula implemented between pressure arm and sample utilised for eucalyptus ATR analysis.* 45

Figure 25: *live in vivo imaging of eucalyptus plant (top, bottom left) example of sample mounting for ex vivo wheat and eucalyptus leaves aluminium foil directly under sample (right)*.....47

Figure 26: *Image of FTIR general set up with Focal Plane Array detector*.....48

Figure 27: *General ATR set up microscope and detector (left), Synchrotron ATR-FTIR beam mirrors/optics focus (right)* 49

Figure 28: *Sample mounting and placement 2D Maia XFM imaging, samples located directly in front of incident beam and detector located behind.* 51

Figure 29: *Sample mounting and placement, for 3D XFM confocal imaging, Vortex detector seen at a right angle relative to incident beam, and sample mounted at a 45 º angle with cryo-stream found directly above.*.....52

Figure 30: *Mounted images of wheat sections prepared for SEM imaging control (left) infected (right)*.....53

Figure 31: *ATR-FTIR overview spectra of four* ***mature*** *eucalyptus species (adaxial left, abaxial right) (Karri: blue, Marri: green, Tuart: yellow, Wandoo: red) and zoomed in ν(C-H) (2800-3000 cm^{-1}) region, demonstrating disparity in wax (lipid) content between species* ***A-D****. 2D score plots from PCA showing the distribution of*

*four eucalyptus species Karri (blue) Marri (green) Tuart (yellow) Wandoo (red) comparing species grouping for different anatomical regions (adaxial left, abaxial right) in mature leaves **E,F**. Factor loading distributions (adaxial left, abaxial right) showing where principal component PC-1 (blue), PC-2 (right, green), and PC-3 (left, green) separation has been attributed to for different eucalyptus species **G,H**.* 60

Figure 32: *ATR-FTIR individual spectra of **mature** eucalyptus tuart (5 adaxial (green), 5 abaxial (blue)) in overall (400-4000 cm^{-1}) and lipid C-H (2800-3000 cm^{-1}) stretching regions, demonstrating disparity in wax (lipid) content between adaxial and abaxial surfaces **A, B**. SEM images of eucalyptus tuart mature leaves adaxial (**C**) displaying "column like" structures throughout the plant tissue, and abaxial (**D**) displaying distribution of epicuticular wax crystallinity scale = 10 µm.* 62

Figure 33: *ATR-FTIR individual spectra of **immature** eucalyptus Tuart (5 adaxial (green), 5 abaxial (blue)) in overall (400-4000 cm^{-1}) and lipid v(C-H) (2800-3000 cm^{-1}) stretching regions, demonstrating disparity in wax (lipid) content between adaxial and abaxial surfaces **A, B**. SEM images of eucalyptus Tuart immature leaves adaxial (**C**) and abaxial (**D**) displaying distribution of epicuticular wax crystallinity scale = 10 µm.*.....63

Figure 34: *ATR-FTIR individual spectra of immature (green) and mature adaxial (blue) eucalyptus tuart leaves in overall (400 – 4000 cm^{-1}) and lipid v(C-H) (2800 – 3000 cm^{-1}) stretching regions, demonstrating disparity in wax (lipid) content between species **A, B**. SEM images of eucalyptus tuart adaxial leaves immature (**C**) and mature (**D**) showing distribution differences of epicuticular wax layers (webbed vs flaky structure) and crystallinity. Scale = 20 µm.* 65

Figure 35: *Synchrotron macro ATR-FTIR showing sub-micron mapping of epicuticular wax distribution of an unknown cell in eucalyptus leaf section brightfield overview, Asterix of CH_2 and CH_3 regions taken for representative spectra (A, C). Representative synchrotron macro ATR-FTIR spectra showing differences seen throughout protein, [(amide I 1600 – 1700 cm^{-1}) and ($\nu_s(CH_3)$ 2865 – 2885 cm^{-1})], lipid, ($\nu_s(CH_2)$ 2845 – 2865 cm^{-1}), alcohol, (v(OH) 3000 – 3500 cm^{-1}) and ν_s(C=O) 1670 – 1820 cm^{-1}), groups, (green spectra $\nu_s(CH_3)$ imaging region, blue spectra*

$\nu_s(CH_2)$ imaging region indicated in C.) (B). false-colour images of representative functional groups (D-H)......68

Figure 36: *Synchrotron macro ATR-FTIR showing sub-micron mapping of epicuticular wax distribution of an Stomata cell eucalyptus leaves brightfield overview (A, C). Representative synchrotron macro ATR-FTIR spectra showing differences seen throughout protein, [(amide I 1600 – 1700 cm^{-1}) and ($\nu_s(CH_3)$ 2865 – 2885 cm^{-1})], lipid, ($\nu_s(CH_2)$ 2845 – 2865 cm^{-1}), alcohol, (ν(OH) 3000 – 3500 cm^{-1}) and carbonyl, (ν(C=O) 1670 – 1820 cm^{-1}), groups, (green spectra $\nu_s(CH_3)$ imaging region, blue spectra $\nu_s(CH_2)$ imaging region indicated in C.) (B). false-colour images of representative functional groups (D-H).*.....70

Figure 37: *The epicuticular wax layer is not consistently preserved in leaf sections, as observed through FTIR spectroscopic imaging (A-E), and Raman microscopy analysis (F-J). Bright field images reveal sample morphology (A, C). FTIR spectroscopic imaging revealed that the wax layer was absent in some sections (B), but present in other sections (D). False-colour functional group images in (B) and (D) were generated from integrated area under the curve for the $\nu_s(CH_2)$ absorbance band (2840 – 2865 cm^{-1}). Representative FTIR spectra from image positions 1 (good wax preservation) and 2 (poor wax preservation) are shown in (E). Raman microscopy analysis of leaf sections (F-I) yielded similar conclusions. The bright field image (F), and the autofluorescence Raman image reveals leaf structure (G), and the false-colour functional group images generated from integrated area under the curve for the $\nu_s(CH_2)$ absorbance band 2840 – 2865 cm^{-1} reveals location of epicuticular waxes (H). Overlay of the autofluorescence and epicuticular wax image reveals inconsistent preservation of epiculatular wax on the leaf surface (I). Representative Raman spectra from image positions 1 (good wax preservation) and 2 (poor wax preservation) are shown in J. Scale bar F-I = 5 µm.* 76

Figure 38: *Epicuticular waxes on the leaf surface can be measured in situ by SR-ATR-FTIR spectroscopy (direct contact, destructive method) or by FTIR reflectance spectroscopy (non-contact, non-destructive). A) Bright field image of stomata on the surface of a Eucalyptus leaf, which was then analyzed by SR-ATR-FTIR spectroscopy. B) False-color functional group images generated from integrated area under the*

curve for the $\nu_s(CH_2)$ absorbance band (2840–2865 cm^{-1}) in SR-ATR-FTIR spectra showing location of wax rich regions. Scale bar = 5 μm. C) Representative SR-ATR FTIR spectra of epicuticular wax. D) Representative FTIR reflectance spectra from the surface of the Eucalyptus leaf, and E) comparison of FTIR reflectance spectra with SR-ATR FTIR spectra. F) Representative FTIR reflectance second derivative spectra. G) Different anatomical locations on the leaf surface produce different FTIR reflectance spectral signatures, which can be observed in the second-derivative spectra. Spectra in (F) and (G) were not vector normalized prior to calculation of second-derivatives. H) Representative SEM image captured from the surface of the leaf, showing thin wax structures that contribute to the infrared reflectance properties of the leaf surface. Scale bar = 10 μm. I,J) Bright field optical microscope (white light illumination) image of plant leaf surface, showing the sample region that was then imaged with FTIR reflectance (10× magnification). These bright field images of the leaf imaged with FTIR reflectance were collected on a dedicated optical microscope (I) and the optical microscope coupled to the FTIR spectrometer (J). K) False-color FTIR reflectance functional group images of wax layer generated from second-derivative intensity of the $\nu_s(CH_2)$ absorbance band at 2848 cm^{-1}. Scale bar = 500 μm...... 79

Figure 39: *FTIR reflectance signal of the epicuticular wax layer on plant leaf surface is observed independent of background substrate used (Au vs Al) (A). Incubation of leaves in ether ("Ether Wash") extracts waxes from the leaf surface and drastically reduces the FTIR reflectance signal (B).* 82

Figure 40: *FTIR reflectance spectroscopic imaging reveals consistent spectroscopic differences associated with seasonal variation, comparing leaves analyzed in autumn against leaves analyzed in winter. A,B) False-color functional group images of wax layer, generated from second-derivative intensity of the $\nu_s(CH_2)$ absorbance band at 2848 cm^{-1}, showing location of wax rich regions in leaves in autumn (A) and leaves in winter (B). Representative second-derivative spectra (C) and non-derivatized spectra (D) reveal the decreased reflectivity in spectra from leaves in autumn compared to winter, and show the shift of $\nu_s(CH_2)$ to lower wavenumbers in autumn compared to winter. E,F) Statistical analysis of replicates reveals that the observed*

*differences in intensity (E) and peak positions (F) are significant. Data in (E) and (F) are presented as a box and whisker plots showing the mean, upper, and lower quartiles. Error bars show the standard deviation. All statistical testing was undertaken using a two-way ANOVA, followed by post-hoc testing, as described in the Experimental Section. Each experimental group consists of five replicates (n = 5). Post-hoc testing was performed with t-tests, corrected for four multiple comparisons using the Bonferroni method and an alpha of 0.05 (two-tail testing). *p < 0.05, **p < 0.01, ***p < 0.001, ****p < 0.0001. Scale bar = 500 μm.* 84

Figure 41: *FTIR reflectance spectroscopic imaging reveals consistent spectroscopic differences between young (immature) and old (mature) plant leaves. A,B) False-color functional group images of the wax layer, generated from second-derivative intensity of the $\nu_s(CH_2)$ absorbance band at 2848 cm−1, showing location of wax rich regions in young (immature) leaves (A) and old (mature) leaves (B). Scale bar (A,B) = 500 μm. C) Representative second derivative and D) non-derivatized spectra reveal the decreased reflectivity in spectra from older (mature) leaves, and show the shift of $\nu_s(CH_2)$ to lower wavenumbers in older (mature) leaves, relative to younger (immature) leaves. E,F) Statistical analysis of five replicates from different morphological regions show that differences in peak intensity (E) and peak position (F) are significant for stem, the cuticle adjacent to the stem (CATS), veins, and cuticle, when comparing spectra from young (immature) and old (mature) leaves. Data in (E) and (F) are presented as a box and whisker plots showing the mean, upper, and lower quartiles. Error bars show the standard deviation. All statistical testing was undertaken using a two-way ANOVA, followed by post-hoc testing, as described in the Experimental Section. Each experimental group consists of five replicates (n = 5). Post-hoc testing was performed with t-tests, corrected for four multiple comparisons using the Bonferroni method and an alpha of 0.05 (two-tail testing). *p < 0.05, **p < 0.01, ***p < 0.001. G) Representative SEM images of surface or immature and mature leaves, showing that the immature leaf surface contains thin, fibril-like wax structures, while large wax aggregates appear on the surface of mature leaves. Scale bar = 10 μm (i), 20 μm (ii), and 50 μm (iii).* 86

Figure 42: *FTIR reflectance spectroscopy enables longitudinal monitoring of epicuticular waxes. A–C) Representative optical images of the leaf of Eucalyptus sapling imaged at different time points depicting young (B) and 7 weeks older (C). D,E) False-color functional group images of wax layer, generated from second-derivative intensity of the $\nu_s(CH_2)$ absorbance band at 2848 cm^{-1}, showing increased intensity at 2848 cm^{-1} in the young leaf (D) compared to the same leaf 7 weeks later (E). F) Representative second-derivative FTIR reflectance spectra showing the shift of the $\nu_s(CH_2)$ band to lower wavenumbers, associated with leaf maturation. G,H) Statistical analysis of five replicates reveals differences in intensity (G) and peak positions (H) are significant for vein and cuticle and not for stem and cuticle adjacent to the stem (CATS). Data in (G) and (H) are presented as a box and whisker plots showing the mean, upper, and lower quartiles. Error bars show the standard deviation. All statistical testing was undertaken using a two-way ANOVA, followed by post-hoc testing, as described in the Experimental Section. Each experimental group consists of five replicates (n = 5). Post-hoc testing was performed with t-tests, corrected for four multiple comparisons using the Bonferroni method and an alpha of 0.05 (two-tail testing). *p < 0.05, **p < 0.01. Scale bar (B,C) = 1 cm; (D,E) = 500 μm.* 88

Figure 43: *FTIR reflectance spectroscopic imaging reveals spectroscopic differences associated with Geraldton wax (A,B), comparing different ages, mature (red), immature (blue), and sprouting needles (green). Spectral variance can be seen in $\nu_s(CH_2)$ peak intensity as well as slight $\nu_s(CH_2)$ shift in spectra (A), while changes in peak shift and intensity in $\nu_s(CO)$ region (B) can also be seen across different maturation stages. Representative Geraldton wax (C), where D displays needle-like leaf structures used for FTIR reflectance analysis.* 90

Figure 44: *Visual images of different time points taken during ethylene gassing time-course experiments including initial, 24 hour, 48 hour and 1 week studies. Ethylene gassed plants (Left) displaying significant flower loss over time in comparison to Geraldton wax controls (right).* 91

Figure 45: *FTIR reflectance spectroscopic imaging reveals consistent spectroscopic differences associated with leaf senescence as a result of ethylene gassing, comparing*

*mature needles in a controlled environment after 24 hours against needles analysed 24 hours after ethylene gassing. A,B) False-color functional group images of wax layer, generated from second-derivative intensity of the ν_s(CH2) absorbance band at 2848 cm^{-1}, showing location of wax rich regions in mature 24 hour post gassing ethylene needles (C) and controlled needles (D). Representative mature 24 hour second-derivative spectra (E) reveal the decreased reflectivity in spectra from ethylene gassed needles in comparison to control and show a shift of ν_s(CH2) to lower wavenumbers in ethylene gassed compared to control. Statistical analysis of replicates reveals that the observed differences in peak position (E) and intensity (F) are significant. Data in (E) and (F) are presented as a box and whisker plots showing the mean, upper, and lower quartiles. Error bars show the standard deviation. All statistical testing was undertaken using a two-way ANOVA, followed by post-hoc testing, as described in the Experimental Section. Each experimental group consists of duplicates (n = 2). Post-hoc testing was performed with t-tests, corrected for three multiple comparisons using the Bonferroni method and an alpha of 0.05 (two-tail testing). *p < 0.05, **p < 0.01, ***p < 0.001 Scale bar = 100 µm.*.....93

Figure 46: *FTIR reflectance spectroscopy enables monitoring of changes in epicuticular wax induced during plant–pathogen interactions in wheat (cv Scout). Bright field optical microscopy images (10× magnification) of control (A) and yellow spot infected (C) wheat leaf samples. FTIR reflectance false-color functional group images of wax layer generated from second-derivative intensity of the ν_s(CH2) absorbance band at 2848 cm^{-1} indicating differences between control (B) and infected (D) wheat leaf sections. Scale bar = 500 µm. Representative second-derivative FTIR reflectance spectra show the shift of the ν_s(CH2) band to higher wavenumbers closer to infected site (E). Statistical analysis of replicates reveals differences in intensity (F) but not in peak positions (G), between control and infected leaves. Data in (F) and (G) are presented as a box and whisker plots showing the mean, upper, and lower quartiles. Error bars show the standard deviation. All statistical testing was undertaken using a two-way ANOVA, followed by post-hoc testing, as described in the Chapter 2.9. Each experimental group consists of five replicates (n = 5). Post-hoc testing was performed with t-tests, corrected for four multiple comparisons using the Bonferroni method and an alpha of 0.05 (two-tail testing). *p < 0.05.*.....95

Figure 47: *FTIR reflectance spectroscopy enables monitoring of changes in epicuticular wax induced during plant–pathogen interactions wheat (cv Magenta). Optical bright-field images of infected (A) and control (C) wheat leaf sections. FTIR reflectance false-color functional group images of wax layer generated from second-derivative intensity of the ν_s(CH2) absorbance band at 2848 cm^{-1} indicating differences between infected (B) and control (D) wheat leaf sections. Representative second-derivative FTIR reflectance spectra show the shift of the $\nu_s(CH_2)$ band to higher wavenumbers closer to infected site (E). Representative SEM image captured from the surface of the leaf, showing fungal hyphae on the surface of leaf section contributing to the infrared reflectance properties of the infected leaf surface (F). Statistical analysis of replicates reveals differences in intensity (G) and peak positions (H), between control and infected leaves. Data in (G) and (H) are presented as a box and whisker plots showing the mean, upper, and lower quartiles. Error bars show the standard deviation. All statistical testing was undertaken using an ordinary one-way ANOVA, followed by post-hoc testing, as described in the Chapter 2.9. Each experimental group consists of five replicates (n = 5). Post-hoc testing was performed with t-tests, corrected for four multiple comparisons using the Bonferroni method and an alpha of 0.05 (two-tail testing). ****p < 0.0001. Scale bar = 500 µm*.....97

Figure 48: *FTIR reflectance spectroscopic imaging reveals spectroscopic differences associated with infection in two wheat cultivars (Magenta and Scout). Optical bright-field images of infected Magenta (A) and infected Scout (C) wheat leaf sections. False-colour functional group images of wax layer, generated from second-derivative intensity of the (CH) absorbance band at 2915 cm^{-1}, showing location of wax rich regions in Magenta (B) and Scout (D) cultivars. Representative second-derivative spectra (E) reveal a slight $\nu_s(CH_2)$ (blue arrow) and a large ν(CH) (red arrow) shift in spectra when comparing cultivars. Statistical analysis of replicate $\nu_s(CH_2)$ peaks observed no significant differences in intensity (F) and peak position (G), while differences observed in intensity (H) and peak position (I) for ν(CH) were seen to be statistically significant. Data in (F-I) are presented as a box and whisker plots showing the mean, upper, and lower quartiles. Error bars show the standard deviation. All statistical testing was undertaken using paired t-tests method and an*

alpha of 0.05 (two-tail testing). Each experimental group consists of five replicates (n = 5) Scale bar = 500 µm.....100

Figure 49: *FTIR reflectance spectroscopic imaging reveals spectroscopic similarities associated with the asymptomatic region of infected leaf, in Scout and Magenta. Optical bright-field images of infected Magenta (A) and infected Scout (C) wheat leaf sections. False-colour functional group images of wax layer, generated from second-derivative intensity of the ν_s(CH2) absorbance band at 2850 cm^{-1}, showing location of wax rich regions in Magenta (B) and Scout cultivars (D). Representative second-derivative spectra (E) reveal a slight $\nu_s(CH_2)$ shift in spectra when comparing cultivars. Statistical analysis of replicates reveals intensity (F) and peak position (G) are not significantly different. Data in (F) and (G) are presented as a box and whisker plots showing the mean, upper, and lower quartiles. Error bars show the standard deviation. All statistical testing was undertaken using paired t-tests method and an alpha of 0.05 (two-tail testing). Each experimental group consists of five replicates (n = 5) Scale bar = 500 µm*.....102

Figure 50: *FTIR reflectance spectroscopic imaging reveals spectroscopic differences associated between cultivars of Magenta and Scout when looking at calcium oxalate. Optical bright-field images of infected Magenta (A) and infected Scout (C) wheat leaf sections. False colour images of calcium oxalate, generated from second derivative intensity of ν_s(CO) absorbance band at 1795 cm^{-1}, showing locations of calcium oxalate in Magenta (B) and Scout (D) cultivars, in symptomatic regions. Representative raw and second-derivative spectra (E and F respectively) reveal changes in ν_s(CO) intensity and slight wavenumber shifts. SEM images display potential presence of calcium oxalate crystals present in both symptomatic (G) and asymptomatic regions (H). Statistical analysis of Scout and Magenta replicates reveals the observed differences in intensity (I) and peak position (J) are not different enough to be statistically significant. Data in (I) and (J) are presented as a box and whisker plots showing the mean, upper, and lower quartiles. Error bars show the standard deviation. All statistical testing was undertaken using paired t-tests method and an alpha of 0.05 (two-tail testing). Each experimental group consists of five replicates (n = 5). Scale bar = 500 µm (A-D) 50 µm (G) and 200 µm (H)*.....105

Figure 51: *Bright-field optical images (BF), Distribution of calcium oxalate ν_s(CO) absorbance band at 1795 cm^{-1} seen in red (IR), in 3 replicates (n=3) of wheat leaves infected with Ptr and harvested 6 days post inoculation for Magenta (Top) and Scout (Bottom) cultivars (R1-R3). Displaying an overall larger area of leaf surface containing calcium in infected Magenta leaf sections. Scale bar = 1 mm* 106

Figure 52: *Statistical analysis of average area of calcium oxalate (ν_s(CO) absorbance band at 1795 cm^{-1}) in pixels (of n = 5 for each species) reveals a significantly larger area in Magenta compared to Scout (p = 0.0028). Error bars show the standard deviation. All statistical testing was undertaken using student's t-tests method and an alpha of 0.05 (two-tail testing).*.....107

Figure 53: *2D Maia XFM false colour images of 2, 4 and 8 dpi, reveal the accumulation of Ca^{2+} 2-4 dpi and depletion of calcium during 4-8 dpi over time when comparing days post infection for wheat (cv Magenta). Scale bar = 1mm* 114

Figure 54: *2D Maia XFM false colour images reveal the presence of concentrated calcium hot spots around and within the necrotic lesion in Triticum aestivum cv Magenta and Scout cultivars after 4-days post infection. Scale bar = 1mm* 116

Figure 55: *Statistical analysis of Magenta and Scout replicates reveals the observed average area of calcium hot spots (Kα1 3691 eV) in μm^2 (of n = 3 for each species) having a much greater average area in Magenta when comparing to Scout (p = 0.0050). Error bars show the standard deviation. All statistical testing was undertaken using student's t-tests method and an alpha of 0.05 (two-tail testing)* 117

Figure 56: *Confocal 3D XFM false colour images showing calcium distribution at different depths of plant tissue. Quantitative scale (set A) and individual Min-Max scale (set B) Scale bar = 1mm* 119

Figure 57: *Schematic reference of theorised Ca^{2+} transmission at different tissue thickness' using cellulose $[C_6H_{10}O_5]_n$ to approximate wheat tissue chemical composition and density*.....120

Figure 58: *Schematic reference of calculated X-ray attenuation in a 250 µm thick $C_6H_{10}O_5$ sample displaying transmission signal relative to the photon energy being distributed throughout the sample. Different line transmissions of varying metals, with key metals K^+ (green) line transmission ~ 0% of signal, Ca^{2+} (blue) line ~ 15% transmission, while Rb^+ (purple) line displays ~ 98% of rubidium would be detected within a 250 µm sample.* 121

Figure 59: *15 µm thick sectioned Triticum aestivum cv Scout wheat samples analysed via 2D Maia XFM. False colour images showing distribution of Rb^+ (blue) (A) K^+ (red) (B) and an overlay image of both Rb^+ and K^+ (blue and red) (C) highlighting the overlap of Rb^+ and K^+ localisation. Areal density distribution of Rb^+ and K^+ in sectioned wheat display a linear correlation (D). Scale bar = 1mm*.....123

Figure 60: *Triticum aestivum cv Scout wheat samples analysed via 2D Maia XFM. False colour images showing distribution of Rb^+ (blue) (A) K^+ (red) (B) and an overlay image of both Rb^+ and K^+ (blue and red) (C) highlighting the overlap of Rb^+ and K^+ localisation. Areal density distribution of Rb^+ and K^+ in wheat display a heavier density of Rb^+ than K^+. Scale bar = 1mm*.....124

Figure 61: *Wheat (cv Scout) samples analysed using 2D Maia XFM. False colour images of paired control tissue displaying K^+ (A) and Rb^+ (E) intensity differences in whole wheat tissue. Triplicate false colour images displaying signal intensity of K^+ (B-D) and Rb^+ (F-H) in infected wheat. Scale bar = 1mm*.....126

List of Tables

Table 1: *Metals found in plants and their common functions (56-61)*.....19

List of Abbreviations

ATR	Attenuated total reflectance
Ca^{2+}	Calcium
CATS	Cuticle adjacent to stem
EM	Electron microscopy
FTIR	Fourier transformed infrared
GC	Gas chromatography
HPLC	High performance liquid chromatography
IRM	Infrared Microscopy
IRRAS	Infrared reflectance absorption spectrometry
K^{+}	Potassium
KB	Kirkpatrick-Baez
MALDI-TOF	Matrix assisted laser desorption ionisation time-of-flight
MS	Mass spectroscopy
PCA	Principal component analysis
Ptr	*Pyrenophora tritici-repentis*
Rb^{+}	Rubidium

ROS	Reactive oxygen species
S/N	Signal to noise
XFM	X-ray fluorescence microscopy
XOS	Polycapillary optics

CHAPTER 1

Introduction

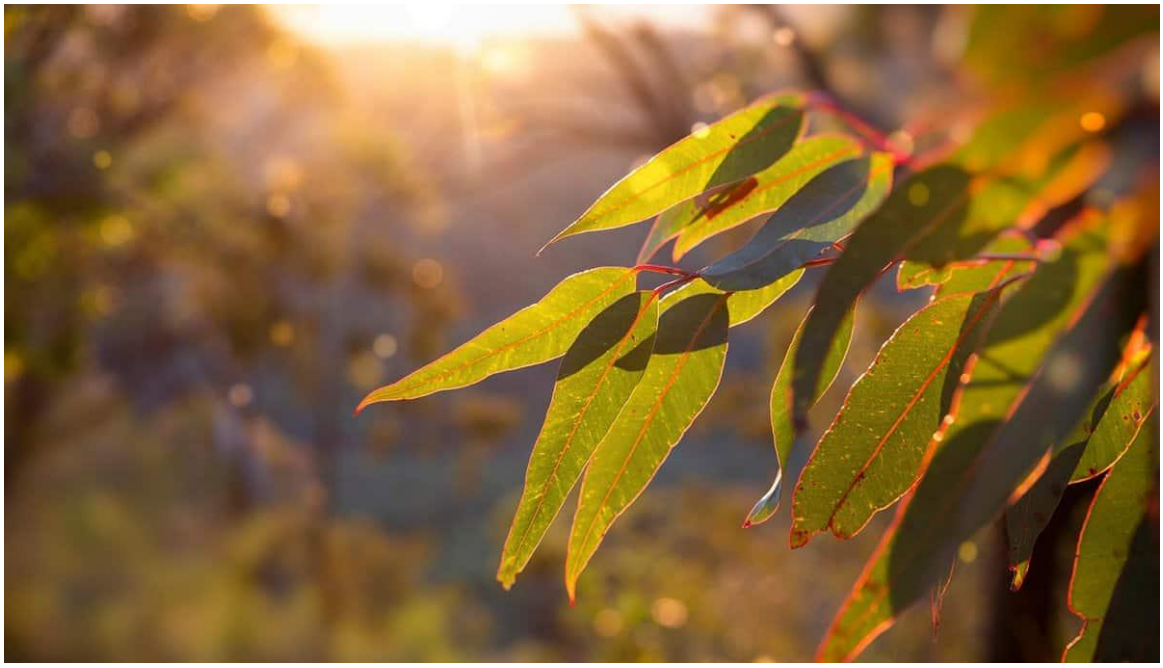

1.1 General Introduction

With an increasing global population, it is important to ensure crop health to provide global food security. Threats to crop health include crop diseases and environmental stressors such as soil degradation and rising temperatures associated with climate change. A key step in mitigating the effects of disease and environmental stressors on crop health, is the ability to monitor/diagnose their effects on crop health.

Traditionally, knowledge on chemical mechanisms to study impact of environmental stress on plants has been generated from *ex vivo*, destructive, bulk chemical analyses. (1, 2) Bulk chemical analyses, which typically have excellent chemical specificity and detection sensitivity, are incredibly important, and have yielded many important findings. However, a greater overall biochemical picture can be obtained if bulk analyses are complemented with direct *in situ* biochemical imaging, enabling association of the distribution of biochemical markers with plant anatomical structures. Further, capability of *in vivo* chemical imaging would offer potential for time-course chemical analysis of living systems. Improved ability to study chemical mechanisms of plant stress and disease is important to help the development of mitigation strategies which can lead to future improvements in overall crop yields and plant health.

In the last two decades spectroscopic mapping / imaging techniques such as Fourier transform infrared spectroscopy (FTIR), Raman spectroscopy and X-ray fluorescence microscopy (XFM) have emerged as methods capable of direct, chemical analyses in biological samples. As such, these techniques have begun to fill a previously unmet research challenge in the plant sciences – direct *in situ* or *in vivo* chemical imaging. Such imaging capability has long been sought to study the chemical mechanisms and impact of plant stress and diseases.

The research carried out in this thesis focuses on the application of imaging methodologies incorporating both FTIR microscopy and XFM, to shed new light on plant disease. However, while the primary focus of this research was in the context of crop health, the application can also be plausible for the preservation of native flora. The following sub-sections will discuss the relevant background on epicuticular waxes and how they are influenced by different physical, environmental and disease traits

(1.2), techniques used to study epicuticular waxes – with a focus on infrared spectroscopy and its background theory (1.3), relevant background on plant metallomics and how it is involved in plant health and disease (1.4), techniques used to study plant metallomics – with a focus on synchrotron XFM (1.5), and lastly the specific aims of this thesis (1.6).

1.2.1 The role of Epicuticular Waxes in Plant Biology

Epicuticular waxes are located on the surface of plant leaves and provide a range of vital protective functions to sustain plant health. Specifically, the wax coating serves to minimise water loss, protect against UV damage, provide a mechanical barrier to disease, and act as an anti-feedant, amongst others. (3) Lipid synthesis and production of the epicuticular wax coating is therefore, vital to plant health. Epicuticular waxes are chemically diverse, and numerous chemical compounds have been identified. In general, epicuticular waxes are long chain hydrocarbons of esters, alcohols and ketones. (4) Synthesis of epicuticular waxes are intrinsically linked to lipid metabolism within the plant and unique differences in lipid metabolism between plant species typically manifests in plant-specific epicuticular wax composition on the leaf surface. The average chemical composition of epicuticular waxes, in addition to intra-cuticular waxes, showing the relative abundance of different molecular classes is shown in Figure 1. A schematic of the anatomy of the plant leaf surface and epicuticular wax layer is shown in Figure 2.

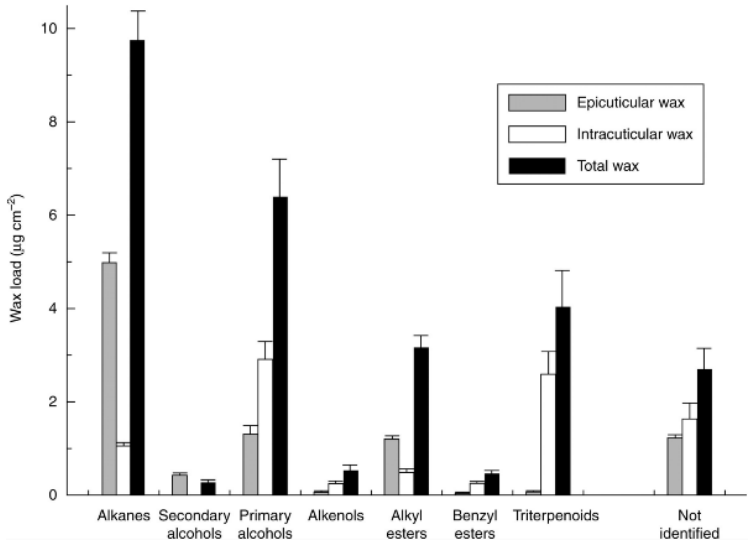

Figure 1: *Epicuticular wax composition throughout Rosa canina leaves, adopted from (3)*

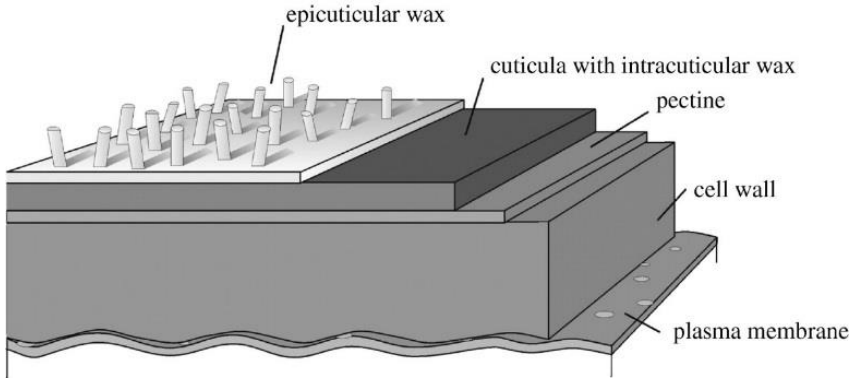

Figure 2: *Cross-section schematic of the epicuticular wax layer of the outer most layer of plant cuticle, adopted from (5)*

1.2.2 Effects of Environmental Stress on Epicuticular Wax Function

The epicuticular wax layer on the surface of plant leaves is an evolutionary adaptation to enhance plant survival during times of environmental stress or disease (Figure 2). Studies of plants focussed on seasonal variation in the southern hemisphere, indicate adaptation of the wax layer. The results indicated lower amounts of epicuticular wax in winter as less risk associated to dehydration was present in comparison to greater wax coverage in summer where plants were at higher risk of dehydration. (6, 7) An opposite trend for seasonal variation in wax thickness is observed in the northern hemisphere, specifically increased thickness during winter months, which acts as an insulator to protect internal plant structures (Figure 3). (8) In addition to seasonal variation, the distribution and composition of the epicuticular wax layer has been established to vary with: leaf age; health or fitness; and in response to environmental stressors such as drought, hyper salinity, increasing soil acidity or soil contamination (i.e., metal toxicity). (9-12) For example increased thickness of the epicuticular wax layer reduces leaf transpiration and maintains stomatal conductance, which increases wheat yield in drought stricken areas. (12) Study of variation in flora species across different global locations showed that some flora were able to adapt well to heat exposure through variation of their epicuticular wax layer. Specifically, the wax layer was able to reflect the excess UV radiation while maintaining stomatal conductance, while those which lacked sufficient epicuticular wax suffered from a decline in

stomatal conductance and therefore limited transpiration. (13) Although epicuticular waxes have been established to vary in response to environmental stressors, the specific mechanisms that control secretion of specific wax components into the epicuticular layer, remain largely unknown. (11) Nonetheless, the fact that epicuticular waxes show such variation in response to plant stress makes them a valuable marker for both plant health/fitness, and state of the surrounding environment. (11)

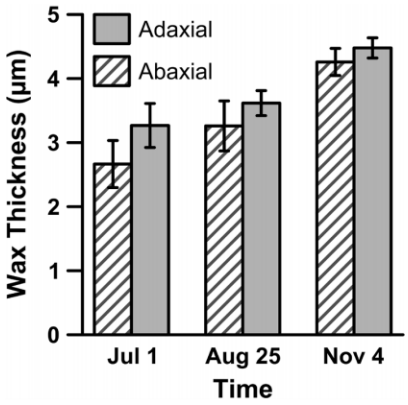

Figure 3: *Seasonal variation in epicuticular wax thickness on the adaxial and abaxial surfaces of Douglas-fir needles. (8)*

1.2.3 Stomata and Their Function in Plants

Stomata are cellular structures that are embedded on the surface of the plants epidermis (excluding stems in most cases), they are comprised of an outer subsidiary cell, guard cells which contain chloroplasts and a nucleus which help in the functioning to open and close the central stomatal pores. (14)

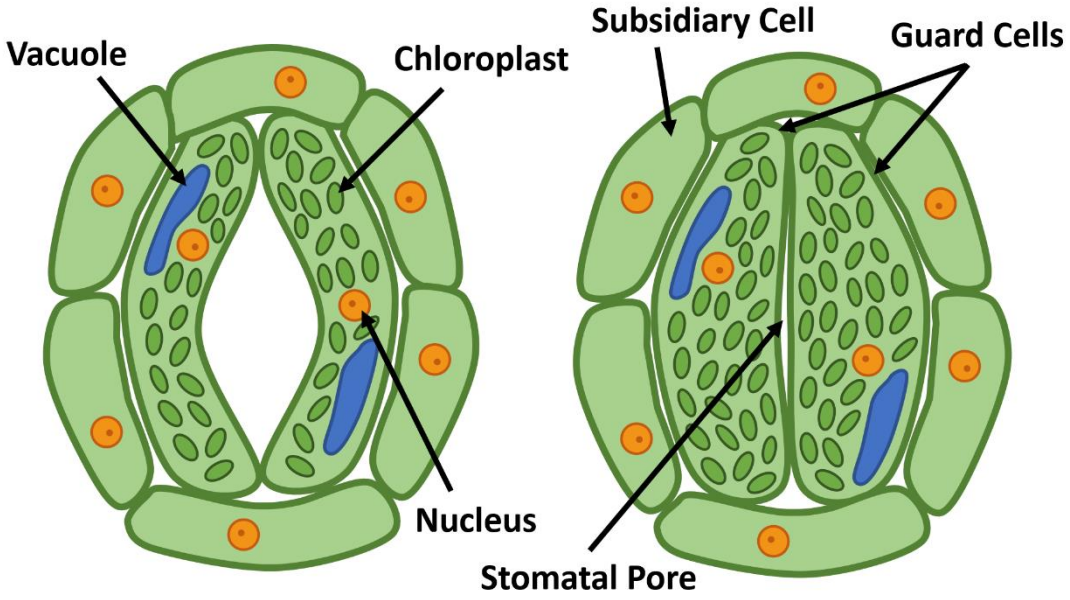

Figure 4: *Schematic of Stomata and different cellular/sub-cellular compartments*

The opening of the stomata allows for the gas exchange of carbon dioxide, oxygen, and water vapor (in the form of transpiration) which takes place in order for photosynthesis to occur, while also helping to reduce water loss by closing in sub optimal conditions such as when hot or dry weather is present. Depending on the plant there can be varying amounts of stomata as well as varying shapes/sizes, majority of stomata are located on the abaxial side of the leaf with the exception of wheat (*Triticum* sp.) in which the adaxial side density is larger. (15)

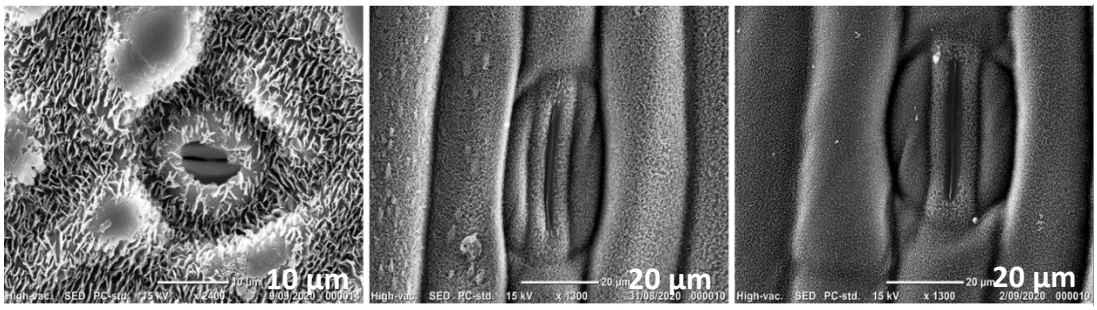

Figure 5: *SEM images of different stomata shapes and sizes depending on plant species (left to right): Eucalyptus (tuart), wheat (cv Scout), wheat (cv Magenta). Scale bars - 10 and 20µm.*

The subsidiary cells, support the guard cells and surrounding cells, acting as a buffer between the guard cells and exterior epidermal cells. This protects the exterior epidermal cells against guard cell expansion and contraction. The opening and closing of guard cells are regulated by several factors including, light, CO_2 levels, and changes in environmental conditions. (14, 15) The guard cells of the stomata use a potassium pump (K^+) diffusion process in which the cells regulate potassium concentrations between the surrounding epidermal cells and guard cells in order for the guard cells to swell or shrink and allow for gas exchange to occur depending on the needs of the plant. (14, 15) When the stomata need to open allowing for gas exchange, potassium ions are pumped into the guard cells from surrounding epidermal cells, causing the guard cells to swell and curve. This allows the stomatal pore to open in order for the exchange of CO_2, O_2 and water vapor to occur.

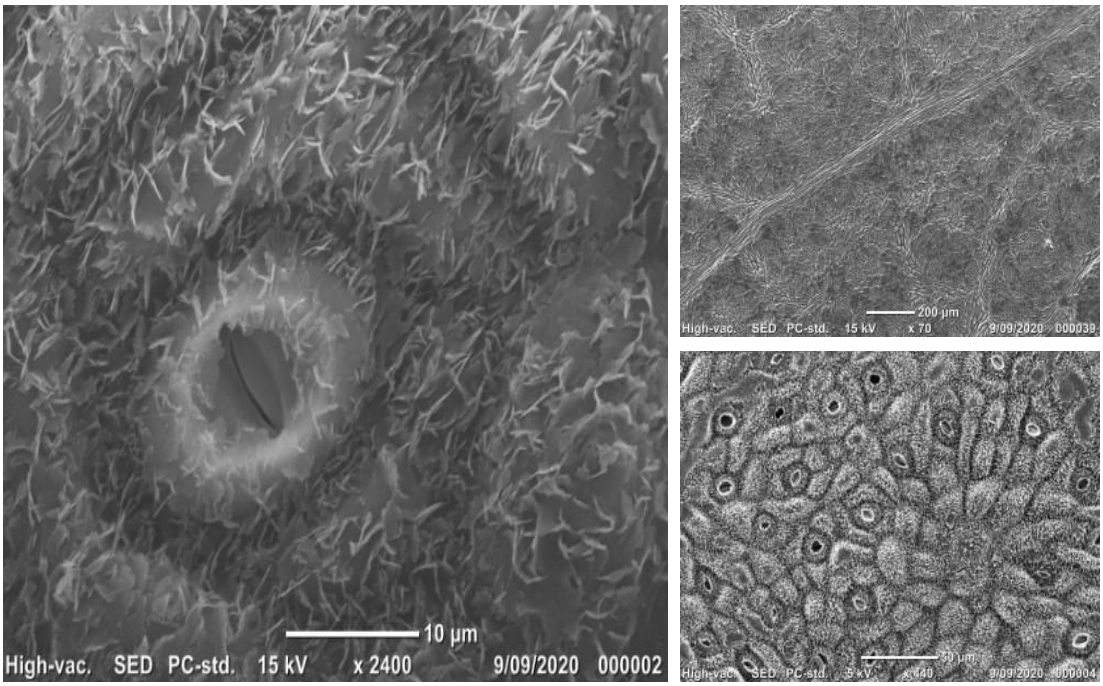

Figure 6: *SEM images of Eucalyptus tuart, showing stomata cells being surrounded by wax, opening, and closing of guard cells due to electron beam exposure 10 µm, 50 µm and 200 µm scale.*

1.2.4 Disease Induced Change to Epicuticular Wax Layer

While epicuticular wax acts as a protective barrier preventing water loss, facilitates transport of solutes and gases, and helps regulate transpiration, it also acts as a line of defence against pathogens and herbivorous insects. (16, 17) Plant cuticles have the

ability to expand and change their composition during varying developmental stages. (18) During pathogen interactions with the host, the plant cuticle and cell wall compositions are affected by the invading pathogens, the pathogens sense the surface of the plants components and change their pathogenesis accordingly to suite the host to have the best chance at invading. For example, during the early stages of infection, phytopathogenic fungi directly target the cuticle by synthesising hydrophilic enzymes, including esterases, cutinases and lipases which play a key role in the pathogenic infection, by degrading the cuticle. (19-21) By being able to monitor chemical changes in the above plant structures located on the plant leaf surface (epicuticular waxes, stomata, cuticles) during pathogenic infection would create the potential to obtain greater insight of plant disease.

1.2.5 Mechanisms and Pathology of *Pyrenophora tritici-repentis*

Yellow spot disease is caused by the necrotrophic fungus *Pyrenophora tritici-repentis* (Ptr). As the name states, yellow spot is a yellow/tan coloured necrotic lesion caused by the fungal infection and resulting in chlorosis of the surrounding tissue in wheat plants. (22) Due to the size of the necrotic and chlorotic tissue and subsequent reduction in photosynthetic active area, yield losses up to 50% are reported. (23) Ptr works by secreting an array of toxins which interact with the hosts genes causing inhibition of photosynthesis, accumulation of reactive oxygen species (ROS), and cell death. (24, 25) While yellow spot is a wide spread disease found in major wheat growing regions, previous studies have mainly focused on effector mediated host pathogen interactions. (25-27) The invading plant pathogens cause alterations through specific effector proteins which target the host plants systems. (28, 29) Given the large change in plant physiology and biochemistry that occurs during yellow spot disease, it is likely that epicuticular waxes on the leaf surface also change. If so, these may serve as a unique marker of crop health and disease status. This serves as the driving motivation behind method developments in Chapter 3 and Chapter 4 of this thesis.

Another facet of plant health that may be affected during disease, is plant metallomics (described in Section 1.41). Increased understanding of how plant metallomics changes during disease may shed light on disease pathways, and possibly reveal new

treatment strategies. Understanding the effect of yellow spot disease on wheat metallomics forms the driving motivation of chapter 5 of this thesis.

Yellow spot will be used as a fungal infection case study, utilising both infrared microscopy and X-ray fluorescence microscopy techniques to see how epicuticular waxes and metal concentration and distributions are affected during plant disease.

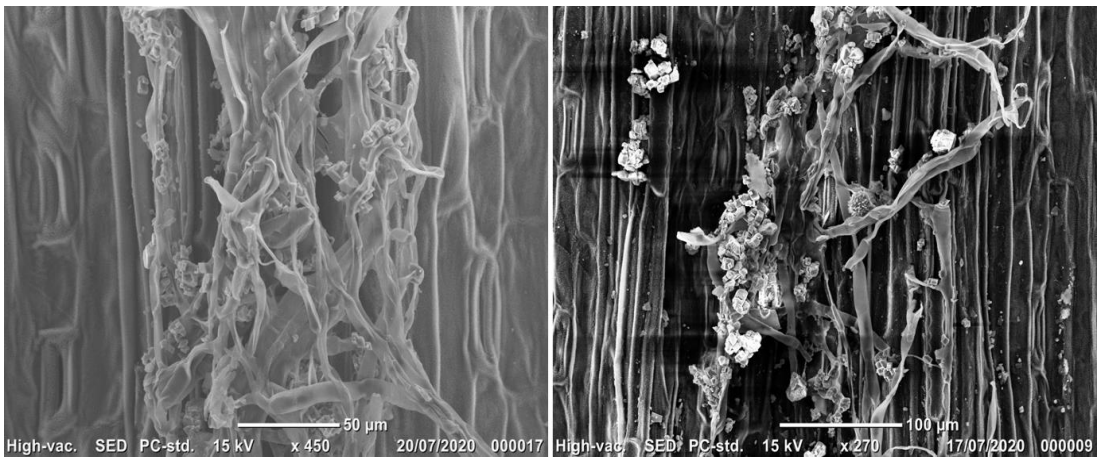

Figure 7: *SEM images of Pyrenophora tritici-repentis infected wheat (cv Scout) leaf section, 50 µm scale (left) and 100 µm scale (right)*

1.3.1 Techniques to Study Epicuticular Waxes – Bulk Methods

Currently within the field of plant physiology, an array of research has been conducted using traditional analytical techniques such as high-performance liquid chromatography (HPLC) and mass spectrometry (MS) to study the relationship between epicuticular wax compositions and internal plant physiology. (30, 31) HPLC and GC-MS are powerful analytical tools that can quantify numerous chemical species at excellent detection limits (i.e. high chemical specificity and sensitivity). Unfortunately, one limitation of these traditional methods is that they require solvent extraction, which prevents studies of spatial location of waxes on the leaf surface. Thus, there has been an un-filled niche in this research field for methods capable of non-destructive, direct, *in situ* and spatially resolved detection (or imaging) of epicuticular waxes on the surface of plant leaves. Therefore, the distribution of waxes across the leaf surface in relation to plant physiology and anatomical features such as stomata are still largely unexplored.

1.3.2 Techniques to Study Epicuticular Waxes – Imaging Methods

There are two analytical methods that have found regular use for spatially resolved studies of epicuticular wax distribution on the surface of plant leaves, electron microscopy (EM) and matrix assisted laser desorption ionisation time-of-flight (MALDI-TOF) mass spectrometry. (1, 32) EM has previously been utilised to investigate the micro- and nano-structures of epicuticular waxes on the leaf surface, however due to the limited field of view, it is not well suited to provide essential information of how wax distribution changes in relation to plant anatomy across a macro scale. Further, while EM can reveal incredible detail, at nm spatial resolution, it provides little information about the chemical composition of the wax. In contrast, MALDI-TOF-MS-imaging offers excellent chemical specificity, being able to detect specific molecular compounds. Unfortunately, MALDI-TOF-MS-imaging does not offer the same spatial resolution EM, and typically individual molecular species can only be imaged at 30-100 μm. (33)

1.3.3 Basic Theory of Infrared Spectroscopy Techniques

Infrared spectroscopy is a method in which light (electromagnetic radiation) interacts with the oscillating electric field produced by an oscillating bond dipole during molecular vibration. The interaction can be analysed via reflection, absorption or emission. (34) The position at which infrared absorbance band occur is characteristic of the functional groups present within a sample, which is the result of the differing bond lengths, bond strength, and bond dipole between functional groups. The intensity of an absorbance band is proportional to the bond dipole, with stronger bond dipoles producing more intense absorbance. Due to its wide array of wavelengths infrared is often split into three different subdivisions, this includes most commonly used mid-IR region ranging from 400 cm^{-1} to 4000 cm^{-1}, far-IR 10 cm^{-1} to 400 cm^{-1} and near-IR 4000 cm^{-1} to 12800 cm^{-1}. (35, 36) Many studies in the biological sciences have predominantly focused on mid-infrared regions as this is the location at which fundamental modes of most organic molecules absorb, and a wide variety of instrumentation to study these molecular vibrations have been made available. (35, 36)

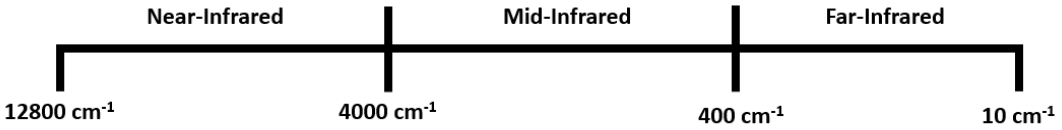

Figure 8: *Schematic representation of infrared wavelength regions ranging from far-infrared to near-infrared*

When molecules that contain bonds with a net dipole change during molecular vibration are exposed to infrared radiation, an absorption process can occur. Specifically infrared light is absorbed at wavelengths with a corresponding frequency that matches the frequency of the oscillating bond. In doing so, the molecular vibration absorbance energy and is excited to a higher vibrational state. (37) Commonly observed molecular vibrations include stretching vibrations (which can be symmetric or asymmetric) and bending vibrations which involves scissoring (in-plane), rocking (in-plane), wagging (out of plane) and twisting (out of plane) (Figure 9).

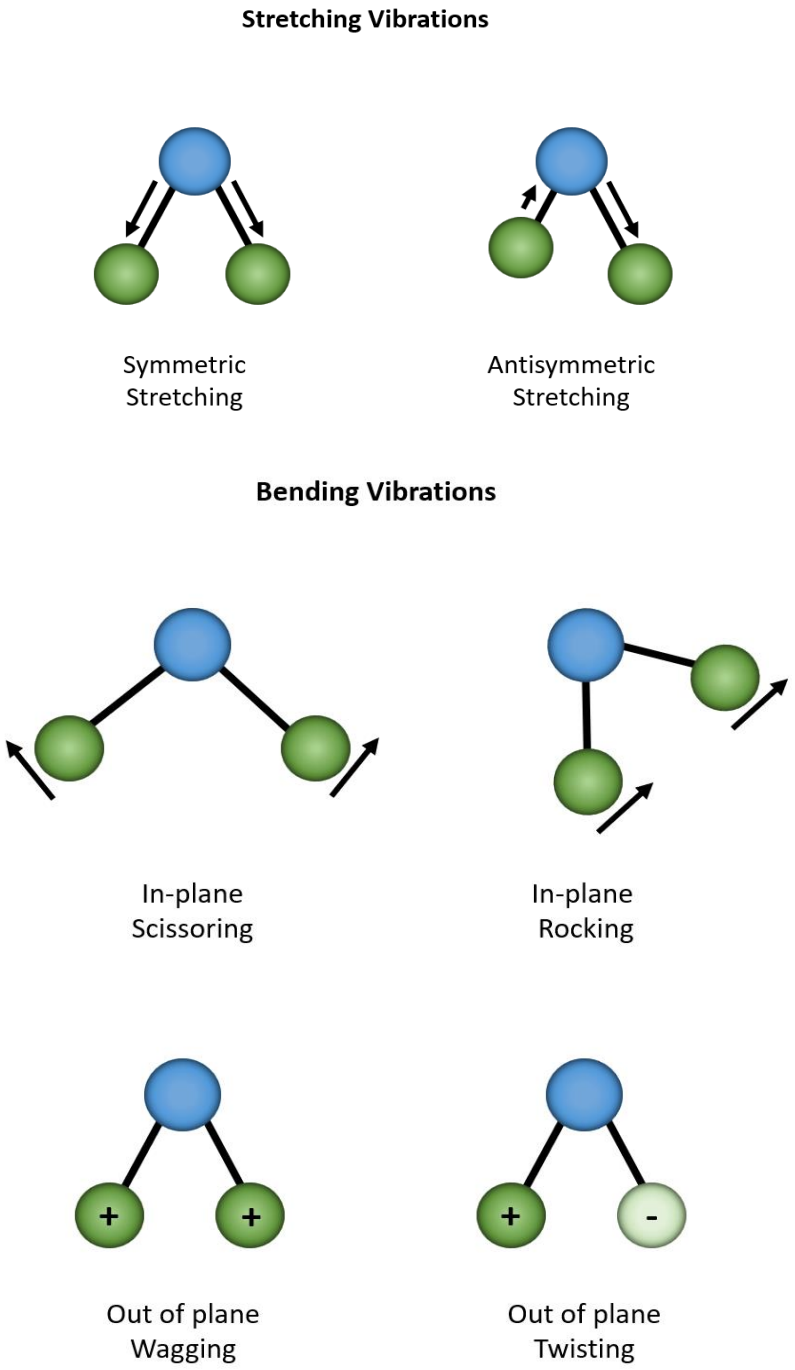

Figure 9: *Different stretching and bending molecular vibrations. + indicates movement out of the plane while – indicates movement in. (35, 37)*

Infrared active molecules are most commonly analysed through the use of Fourier transformed infrared spectroscopy (FTIR). A key component of the FTIR spectrometer is the interferometer, a beamsplitter splits the infrared beam into two, a reflecting and transmitted light source splitting at right angles where it is guided towards a fixed and a moving mirror. The split beams are each reflected back to the interferometer and recombined to give constructive and destructive interference (Fig 10). This process (interferometry) provides benefits for infrared spectroscopy, owing to the ability that all spectral bands are simultaneously measured leading to greater sensitivity (Fellgetts advantage), as well, the interferometer not requiring a slit for measurement, leading to substantially more light within the system (Jacquinot advantage). (38, 39) The benefits of which Fellgett and Jacquinot advantages result in greater signal/noise ratios, improving the overall measured signal.

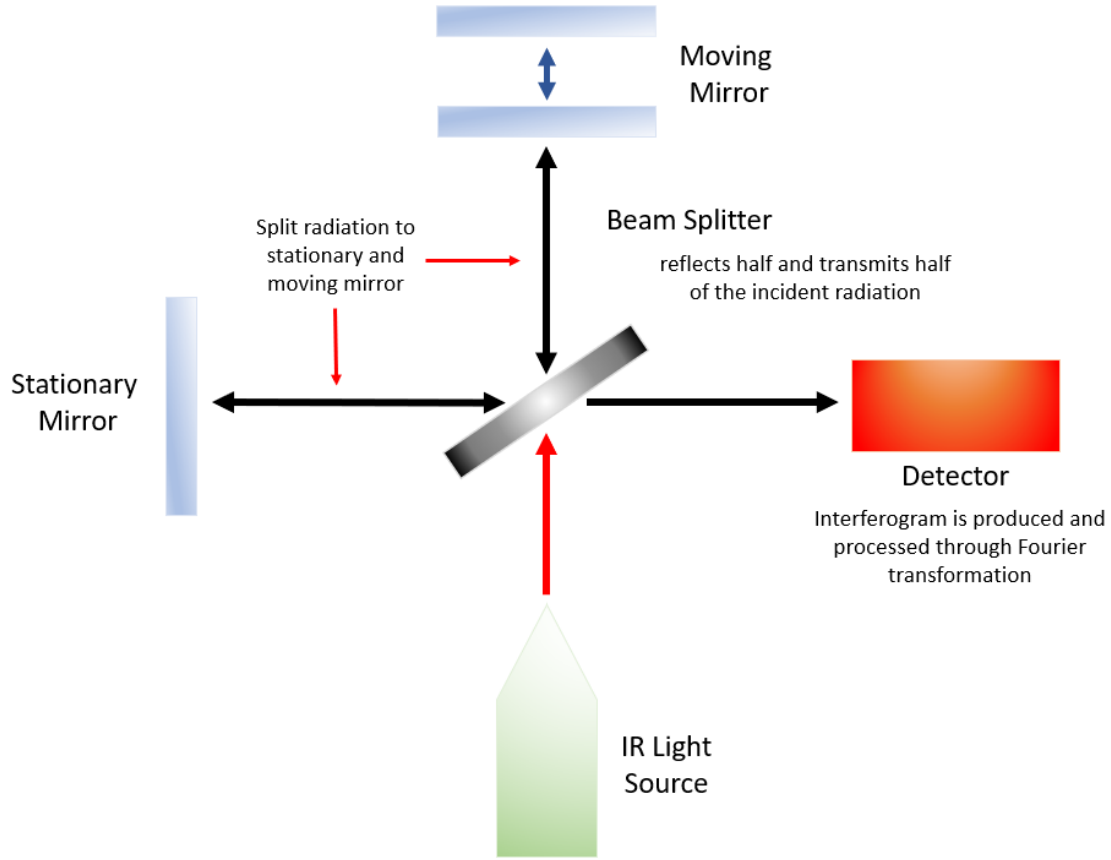

Figure 10: *Schematic representation of how FTIR spectrometer works*

1.3.4 Attenuated Total Reflectance – Fourier Transformed Infrared Spectroscopy

Attenuated total reflectance FTIR (ATR-FTIR) is a surface sensitive technique (detects ~1 μm of the sample surface), and therefore, well suited to study the epicuticular wax layer on plant leaves. ATR-FTIR uses the property of total internal reflection producing an evanescent wave on the crystal surface, the oscillating electric field of the evanescent wave can interact with the oscillating dipole of the molecules within the sample. giving a signal measurement in which a spectrum is produced. (40) ATR-FTIR spectra reflect the array of organic constituents on the leaf surface, and these spectra are easily obtainable using laboratory or portable field instrumentation. In addition, due to the use of high refractive index crystals, ATR-FTIR spectra are capable of improved spatial resolution ($r = \frac{0.61 \times \lambda}{n \times \sin\alpha}$) (where $n \times \sin\alpha = NA$, λ = wavelength and r = resolution), in which the diffraction limit is lower (better) that the diffraction limit of measurements made in a traditional transmission optical geometry.

To date, ATR-FTIR spectroscopy has exclusively been applied to characterise epicuticular waxes at the macroscopic level, which has still yielded valuable insights. This provides a foundation that benefits both ecological and botanical applications. (41) Previous studies from bulk ATR measurements have shown spectral variation on the leaves surface characteristic to lipid distribution which could be due to the differing environmental factors. (41) For example, a study looking at the adaxial surface of mature leaves was conducted and found that variations between species are present within the lipid wax region indicating a change in functional groups present. (4) Similarly, studies looking at plant health has provided a foundation in which the investigation into varying environmental growth conditions can be applied utilising ATR measurements. (42) Additionally, the ability of a synchrotron lightsource when coupled with FTIR provides improved spatial resolution, and increased ability to study spatially resolved cellular components on the surface of plants. This enables a deeper understanding of information in regard to biochemical markers involved in plant development and stress and will be discussed in more detail in Chapter 1.3.5.

1.3.5 Synchrotron ATR-FTIR Microscopy

While the same principles for benchtop ATR-FTIR also apply for synchrotron ATR-FTIR, there are a few subtle differences that prove beneficial for the analysis of epicuticular waxes. Conventional benchtop instruments do not have a light source bright enough to provide sufficient signal to noise for diffraction limited spatial resolution. Benchtop ATR-FTIR is often not suitable for imaging at the diffraction limit, due to lower photon flux of benchtop infrared sources. A brighter infrared light source is needed when investigating small sample regions that require diffraction limited spatial resolution. (43-46)

Synchrotron ATR-FTIR applies the principal of a confined/focused bright light source along with an ATR crystal with a high refractive index, (Figure 11) facilitating diffraction limited spatial resolution with an acceptable signal/noise ratio. The capability of diffraction resolution imaging enables cellular/sub-cellular studies. (43, 46) The use of high refractive index crystals such as diamond (n= 2.42), silicon (n= 3.42) and germanium (n= 4.00) also help to facilitate an increase in numerical aperture, when conducting ATR-IR microscopy experiments at the synchrotron. (47, 48)

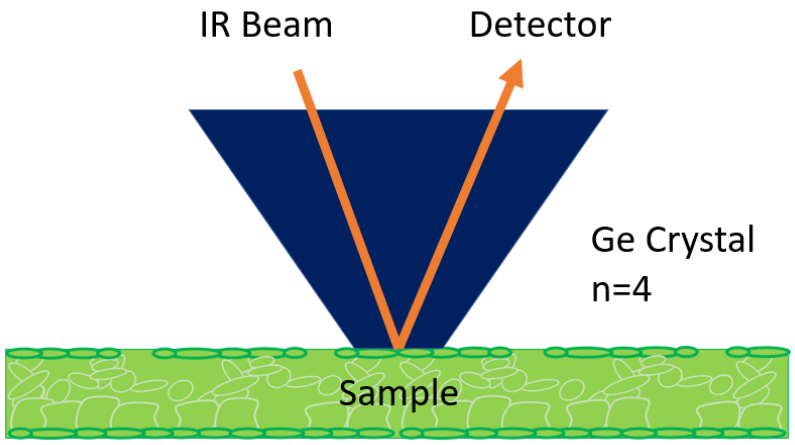

Figure 11: *Schematic representation of how Synchrotron ATR-FTIR works when sample is in contact*

Recent advances into the use of ATR-FTIR Microscopy coupled with a synchrotron light source have shown promising results for future research capabilities. Being able to capture and analyse high spatial and spectral resolution samples requiring micrometre (µm) resolution, with the potential of sub-micron resolution (previously reported by Vongsvivut et al.) prove relevant to the fields of environmental, biology and surface materials amongst others. (44, 47, 49)

1.3.6 Infrared Reflectance Spectroscopy and Microscopy

While ATR-FTIR is well suited for spectroscopic investigation of the epicuticular wax layer, the sample is damaged/destroyed during contact with the crystal, preventing the possibility for repeated studies. FTIR reflectance spectroscopy offers a non-contact (and therefore non-destructive) alternative, which when combined with microscopy could make possible spatially resolved studies on epicuticular wax surfaces of plant leaves. FTIR reflection primarily takes advantage of specular reflection (Figure 12) that occurs from the sample surface, and the signal is often enhanced if the surface contains thin films of ordered molecules. If molecules are ordered, light is reflected at the same (or very similar) angle from multiple molecules, thus higher photon intensity reaching the detector (conceptually a similar process to diffraction/crystallography).

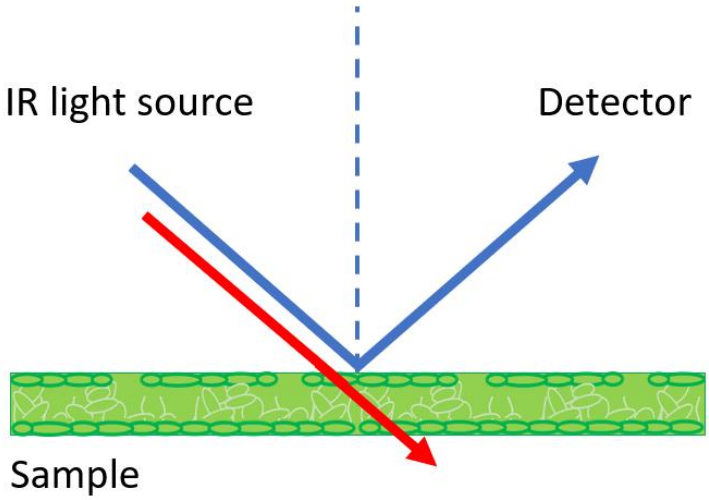

Figure 12: *Schematic depicting infrared transmission (red trace) and infrared reflectance (blue trace) when sample is in contact with light (specular reflection)*

Previously established literature defined the increased reflectance signal that occurs from orientated molecules in thin films as infrared absorption spectroscopy (IRRAS). IRRAS is most pronounced when the film thickness of the sample is less than the wavelength of the light. (50-53) The percentage of reflected infrared light in IRRAS is quite low around ~6% which results in a weak signal and low signal to noise (S/N) spectra, however, although weak, the signal is sufficient for meaningful spectroscopic interpretations. (52-54) IRRAS spectra are presented as the -log R/R0, where R is the reflectivity of the sample surface, and R0 is the reflectivity of the substrate. (50, 53-55) The magnitude of reflectance signal that is observed is influenced by several factors, including the angle of incidence of the light source, polarisation of the light, and the molecular orientation at the surface of the sample. (53, 55)

A range of different reflective surfaces have been used for background reflectivity measurements, this ranges from different metal surfaces (Aluminium, Gold) to H_2O or D_2O. (53-55) IRRAS has been well studied and characterised previously to study the orientation of bio-molecular thin films such as lipids, and peptides at air-water interfaces. (53, 54) The technique has not been demonstrated for *in situ* analysis of ordered molecules within biological tissues. However, the question arises, is the thin film of the epicuticular wax layer oriented and sufficiently thin to produce a detectable IRRAS signal? This thesis seeks to investigate this research question, and ideally to use the IRRAS effect to develop non-destructive *in situ* and *in vivo* imaging of plant leaf surfaces.

1.4.1 Plant Metallomics

Plants require balanced metal-homeostasis to support growth. (56) The main source of metal ions for plants is from soil, and includes potassium (K), calcium (Ca), magnesium (Mg), manganese (Mn), zinc (Zn), copper (Cu), and iron (Fe). A summary table can be found below of typical metals found in plants, and their benefits and contributions as a nutrient source.

Table 1: *Metals found in plants and their common functions (56-61)*

Metal	Function
K	An essential macro nutrient, increases vigour and disease resistance in plants, helps in transport and production of starches, sugars, and oils, activator of multiple enzymatic processes including protein synthesis, sugar transport, carbon and nitrogen metabolism, regulates cell osmotic pressure and cation/anion balance in the cytoplasm, regulates stomatal opening and closing, alongside cell elongation.
Ca	Essential for root health and development of leaves, improves absorption and translocation of nutrients, activates several enzymatic processes relating to growth regulation, strengthens cell walls, and plays a part in cell division, helps in protein formation, and is a first line of defence responder when infection and/or disease occurs within plants.
Mg	Key component of chlorophyll, vital for photosynthesis, plays a role in osmotic regulation of cation/anion balance, as well as regulating cell turgor alongside K, plays a role in photosynthesis, and acts as a cofactor in many enzymatic processes.

Mn	Aids in photosynthesis making the necessary electrons available, helps activate essential enzymes for nitrogen metabolism, essential for the biosynthesis of aromatic amino acids, aids in cell wall stabilisation and pathogen resistance via manganese peroxidases.
Zn	Helps in plant hormone production via a number of enzymatic processes, responsible for leaf growth/expansion and stem elongation, is a constituent of proteins associated with DNA and RNA transcription.
Cu	Essential in many enzymes, protein interactions help stabilise structural integrity and help drive biochemical reactions, is an active transporter both intracellular and tissue specific, also plays a critical role in photosynthesis, respiration, and protects against oxidative stress.
Fe	A key cofactor of many molecular complexes that regulate and promote growth in plants, required for chlorophyll synthesis, and maintenance of chloroplast structure and functions, a part of CO_2 fixation ensuring electron flow.

While metals are essential for plant growth and development, it is still very common for potential toxicity to occur if the translocation of metals to its desired destination does not occur correctly. Mechanisms by which plants translocate metals from roots to different functioning sites is not well understood. However, recent advances in the X-ray spectroscopy field have unveiled, the localisation of metal speciation relative to the plant's anatomy. (62) Micro and macronutrients, are absorbed via diffusion of an aqueous water solution from micro hairs located on the roots of plants, in which they cross multiple cell membranes before being transferred to the xylem in their chelated or hydrated forms. (63, 64) From there, the uptake of different metals and their translocation are dependent on the processes' they take part in. For metals to freely move between plasma membranes, binding to localised transporters occurs, this allows translocation to the desired plant tissue. (62-66) Once the metals have translocated to

the leaves of a plant a number of catalytic transporter processes occur, so that the metals can be differentiated to their various desired locations. (63, 64) Finally, intracellular distribution of metals occur via endomembrane and metallochaperones in which the metals various functions in plant growth and development can take place. (63)

Factors that disturb metal homeostasis include changes in nutritional content of soil, changes in climate, and fungal, viral, or bacterial infection, The ability to assess the content and distribution of metal ions in plant leaves is critical in further understanding the chemical pathways through which metal ions regulate plant health during stress and disease.

1.4.2 The Role of Specific Metal Ions in Maintaining Plant Health

Potassium ions (K^+) and calcium ions (Ca^{2+}) were the primary focus' when investigating metals and their relations to plant health in this thesis, and the literature on the role of these two ions in plant and disease is described in further detail below. K^+ is the most abundant ion in plants and plays a critical role as a macronutrient, with deprivation of K^+ leading to major growth and development defects. (67, 68) K^+ acts as an activator in numerous enzymes within plants, including processes involving protein synthesis, photosynthesis, sugar transportation, C and N metabolism, which play a part in overall yield and quality of plants. (69, 70) K^+ is also integral for cell growth, a process which aids the function and development of plants. (71) In this case, K^+ acts as a stimulant in controlling ATPase in the plasma membrane and subsequently leads to acid stimulation which controls the loosening of cell walls and hydrolase activation in which nutrients is broken down into smaller digestive constituents. (69) The mass abundance of K^+ allows for easier mobility in plants, which helps in regulating cell osmotic pressure as well as balancing other ions within the cytoplasm. (72) Most importantly K^+ is involved in stomatal opening and closing which is a critical site for photosynthesis to occur.

While K^+ is the most abundant metal in plants and plays a critical role in many processes relating to plant growth and development, Ca^{2+} also plays a critical role in

plant health and fitness. Ca^{2+} is another macronutrient and helps maintain structural integrity of cell walls and membranes reducing the likelihood of cell membrane damage and preserving normal structure and function of the cell. (73) It also acts as a ubiquitous second messenger helping in the regulation of plant growth and development, as well as being a first responder to various plant stresses such as pathogenic infections. (74, 75) Ca^{2+} also has synergistic effects with other elements affecting the affinity to absorb other elements. (76) Much like K^+, Ca^{2+} plays a crucial role in photosynthesis, regulating stomatal opening and closure. (74) While both K^+ and Ca^{2+} play crucial roles in regulating and maintaining plant health and development the effects of pathogenic attack has not been studied widely *in vivo*, highlighting the importance to monitor changes that occur during pathogenic attack, revealing qualitative information as to how much of the plant tissue is affected and where the metals are being drawn from.

1.4.3 Effects of Infection on Plant Metallomics

As metal ions are critical to plant health, it is important to understand how plant infection alters metal-homeostasis. Metal homeostasis is challenged when a pathogen infects a plant, as nutrient availability becomes split between the plant and pathogen. Reduced access to metal ions within the plant is often hinders growth and development. (25, 77) An example of this is seen in necrotrophic fungi, which release toxins that initiate plant cell apoptosis, allowing the fungi to then extract nutrients from the dead tissue, enabling the fungi to grow and colonise other parts of healthy plant tissue. (78-80) Plants have however, also developed a range of responses to combat infections. Specifically, plants may use ionophores as a means of sequestering metal ions to limit their availability to the pathogen, in an attempted to "starve out" the infection. (81, 82) In contrast, plants may accumulate and then release high concentrations of metal ions, particularly redox active metal ions (e.g., iron, manganese, and copper) as a way of creating highly localised oxidative stress to chemically damage the pathogen. (77, 81-92) It has also been reported that those necrotrophic fungi (*Rhizoctonia solani AG2-1*, *Phanerochaeta chrysosporium*, *Dichomitus squalens*, and *Trametes versicolor*) secrete oxalate to sequester calcium through the formation of calcium oxalate from the host plant. (93, 94) However, care must be taken when analysing Ca^{2+} distribution as one of the first lines of defence

involves the signalling of cytosolic Ca^{2+} mediated plant responses, accumulating at the site of infection. (79, 95) Depending on the species of pathogenic fungi, and host plant, differing responses in defence of fungal invasion are inevitable, and therefore monitoring and analysing such changes can be rather complex. (90, 96)

1.5.1 Analytical Techniques to Study Metals in plants

Current techniques that exist for the analysis of metal concentration and distribution within plant tissue include synchrotron radiation X-ray fluorescence microscopy (XFM), laser ablation inductively coupled plasma spectrometry (LA-ICP-MS), scanning electron microscopy coupled with X-ray spectroscopy (SEM) and confocal microscopy. All these techniques have various advantages and disadvantages when trying to analyse metals within a plant specimen, this can include: sample preparation time, detection limits, resolution, spatial resolution, and range of detectable elements. (97) Synchrotron XFM is seen favourably when comparing to other analytical techniques due to its relatively straightforward sample preparation, excellent detection limits/spatial resolution, accompanied by direct, multi element mapping at reasonable data collection times. (98-100) Previous studies using synchrotron XFM has looked at the compartmentalisation of different metals alongside their accumulation across a wide variety of plants and anatomical regions of the plant, to study stress responses, natural accumulation, and biofortification of nutrients in relation to genetically modified crops. (98, 99, 101-105)

1.5.2 Synchrotron Infrastructure

A synchrotron is a large cyclic particle accelerator, which generates extremely intense, bright, broadband light via accelerating electrons at speeds close to the speed of light. The broadband light given off from the synchrotron spans the microwave to gamma - ray range, enabling a range of spectroscopy measurements to be undertaken at the one facility (terahertz and infrared spectroscopy, through to high energy X-ray spectroscopies). (49, 106-113)

Synchrotron light is produced from high-energy electrons accelerated to nearly the speed of light (i.e., they become relativistic particles). (114) Changes in the

acceleration of electrons is then induced by magnetic fields, resulting in release of the intense broadband synchrotron radiation. The resulting magnetic field (induced by the strong bending magnets) set the electrons into a circular trajectory, multiple beamlines are generally added to the surrounding ring, in order for different instruments and experiments to be ran simultaneously (a schematic is shown in Figure 13).

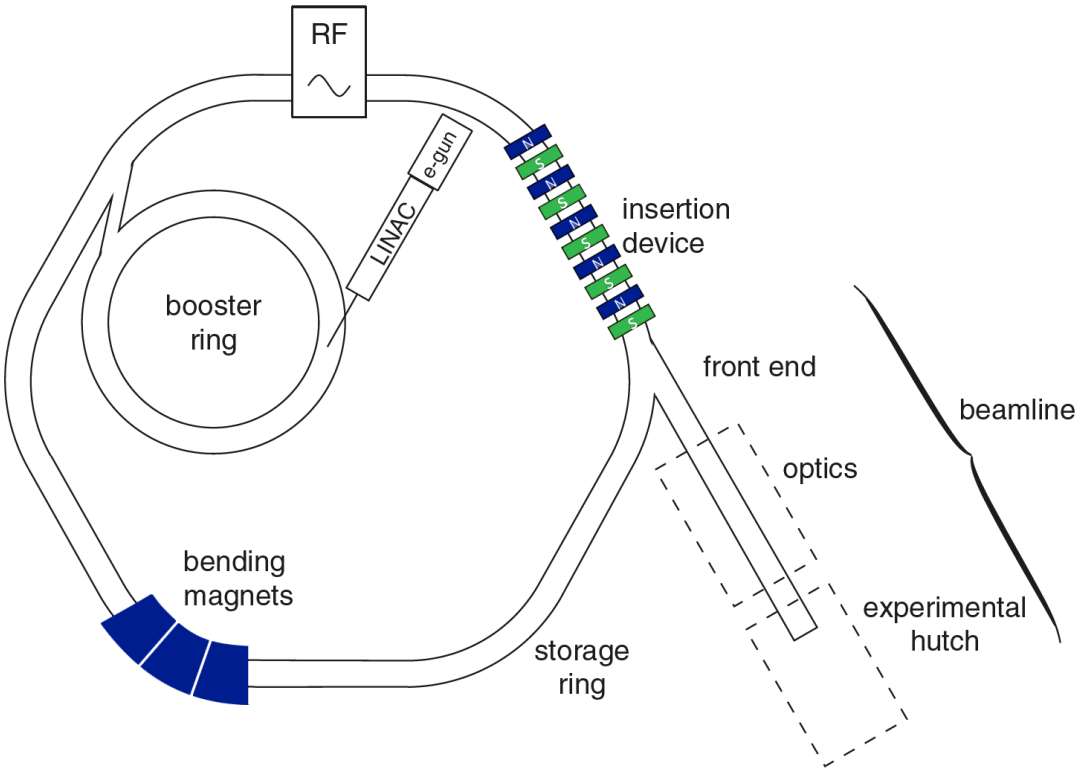

Figure 13: *Important components and configuration of a modern synchrotron source. Schematic adapted from Wilmott et al. (114)*

The first component of the synchrotron is the electron gun which injects electrons into the linear accelerator, accelerating electrons close to the speed of light (99.9997%), through a series of oscillating electric potentials. (114-116) Once the electrons are cycling at sufficient speeds they transfer to the booster ring where the beam energy is raised (3 GeV at the Australian Synchrotron), via a sequence of magnetic fields and radio frequency fissures. (117) The electrons then transferred to the storage ring, where magnetic fields (produced by bending magnets and insertion devices) are used to modulate acceleration of the electrons, producing synchrotron light, as shown in

Figure 14. (118) Synchrotron light is directed towards the experimental end station using a series of optical configurations, often unique for each spectroscopic technique (described in more detail below, for XFM). (114)

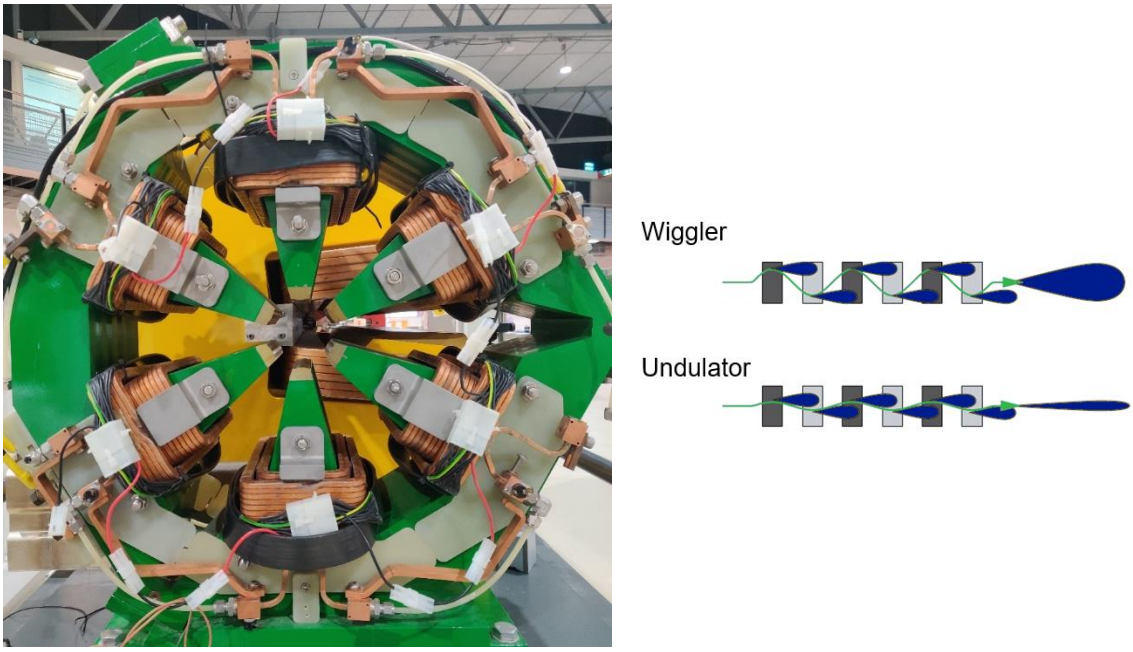

Figure 14: *Prototype magnets found at the Australian synchrotron storage ring, green and red magnets (red not imaged) help focus and steer the electrons while the large yellow one (located behind green magnet) are used for insertion devices which direct the electron flow via wigglers and undulators, maintaining the high intensity flux of light. (114, 117)*

The brightness (high photon density) of synchrotron light provides many benefits over standard benchtop instruments, with spectroscopic analysis often made possible at much finer spatial resolution, lower detection limits and faster data collection times. (119). In the case of XFM, a synchrotron light sources makes possible measurements which would generally take days, otherwise take hours, making large scale map analysis at the single cell level more feasible. (98, 109, 119)

1.5.3 Synchrotron X-Ray Fluorescence Microscopy

X-ray fluorescence microscopy (XFM) uses X-rays to study the elemental distributions and concentrations of biological samples. (120) While benchtop and hand-held XFMs exist, the benefits of a synchrotron light source, enables samples to be measured in a timely manner with exceptional S/N detection limits allowing for detection of even the smallest (microns) amount of trace elements. (98, 99, 121-126)

High energy X-rays bombard the sample, causing electrons within corresponding metal(s) of interest, to be excited and leads to fluorescence occurring (Figure 15). (127) When the incident X-ray energy is high enough to overcome the binding energy of an electron in the inner most orbital, the electron is subsequently ejected from the atom, or if the incident X-ray energy matches that of an electron transition the electron may be excited into an unoccupied molecular orbital, typically the lowest unoccupied molecular orbital (LUMO). (128) When the electron is ejected or moved to the LUMO, an electron vacancy is created (core hole) and the resulting atom is in an excited yet, unstable electronic state. To return to a stable state, an electron from a higher energy orbital (usually the orbital closest to the inner most orbital) fills the vacancy of the inner most orbital, as a result the electron transferring from a higher energy orbital to the lower has an intrinsic energy difference resulting in the residual energy being emitted as fluorescence which has a specific wavelength characteristic of the atom. (129, 130)

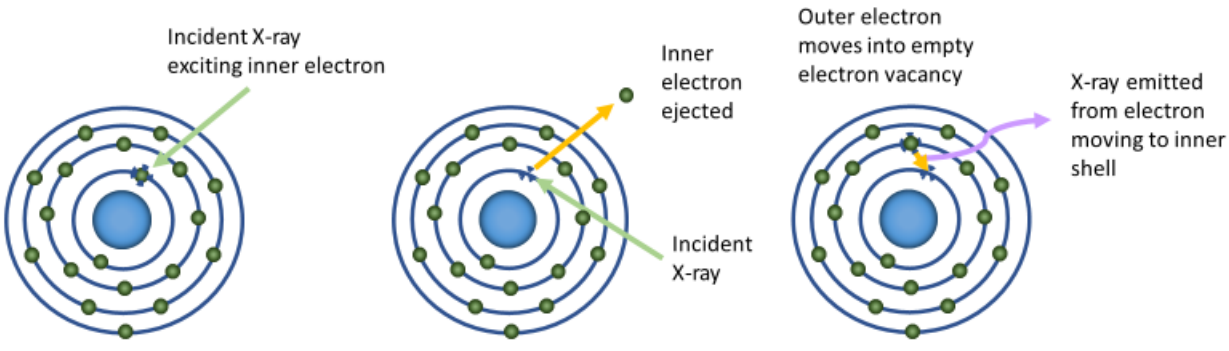

Figure 15: *Principles of X-Ray Fluorescence*

XFM provides the capability to analyse samples both *in vivo* and *ex vivo*. A major advantage of XFM analyses is that unlike other elemental analysis instruments (LA-ICP-MS, XPS, SEM), analysis does not require vaccum conditions and can be undertaken at ambient pressure. (122, 126) The ability to analyse samples at ambient pressure enables more different types of biological tissues to be analysed in hydrated state, without the loss of morphology or possible redistribution of analytes that can occur during dehydration.

There are several key components of an XRF spectrometer: wavelength selection optics, focussing optics, sample stage, energy dispersive X-ray detector, and these are described in further detail below.

1.5.3.1 Energy Dispersive X-ray Detector

An energy dispersive X-ray detector is used to measure X-rays from the sample, which is a mixture of X-ray emission (X-ray fluorescence) and also elastic and inelastic X-ray scatter. (129) There are two main X-ray detectors used at the Australian synchrotron, the Maia 384-element detector and a Vortex silicon drift detector. (109) The Maia detector (Figure 16) used at the Australian synchrotron consists of a 0.5mm diameter aperture in the centre, which enables the X-ray beam to pass through the detector and penetrate the sample using a backscatter array configuration, facilitating freedom for both sample size and increased scanning range. (109) a monolithic silicon planar array, consisting of 384 detector elements connects to independent analogue channels. (109)

Figure 16: *Visualisation of 2D MAIA Synchrotron XFM setup with whole wheat leaf samples, red arrow indicating direction of x-ray beam*

1.5.3.2 X-ray Focussing Optics

Optics are used to focus the X-ray beam to a desired "spot-size", enabling collection of elemental data from a localised region of the sample. The sample can then be raster-scanned "mapped" through the focussed X-ray beam, allowing generation of spatially resolved elemental maps. A common focussing optic used for 2D elemental mapping is, the Kirkpatrick-Baez (KB) mirror pair, which typically provides a focussed X-ray "spot-size" of 1-2 µm. In the KB mirror pair, the mirror shape can be adjusted through two adjustable moments via trapezoidal-shaped mirror, in which radius of curvature and ellipticity can change independent of one another to focus the beam. (109)

1.5.3.3 Wavelength Selection Optics

Synchrotron radiation is inherently broadband, while the majority of XFM experiments utilise monochromatic or narrow-band excitation source. At the XFM beamline at the Australian Synchrotron a narrow band X-ray source is extracted from broad band synchrotron radiation through the use of silicon mirrors containing several

platinum and rhodium strips in order to access different energy ranges: Si (4-10 keV), Rh (4-22.7 keV) and Pt (>22.7 keV). (109)

1.5.3.4 Vortex - Silicon Drift Detector

The Vortex detector is significantly smaller when comparing to the Maia 384-element detector, with the primary detection surface being 80 mm^2 for the central on-axis active area, and two off-axis elements with 50 mm^2 of active area. (109) The vortex detector is positioned 90 º to the incident beam and 45º to the sample in order to minimise scattering signal (Figure 17). (109, 131) 3D confocal imaging was performed using the 4 element Vortex detector, coupled with the use of a cryostream (operating at -40 ºC) to keep *in vivo* biological samples, as pristine/accurate representations of their original form, without having to face tissue damage (Figure 17).

Figure 17: *Visualisation of Synchrotron XFM (vortex detector and 3D setup) with sectioned wheat leaf sample white arrow - indicating cryostat, green – vortex detector, red – mounted sample.*

A key feature of the vortex detector is the ability to collect confocal 3D XFM data. This is made possible due to polycapillary optics (XOS) that can be mounted in conjunction with the single element vortex detector for analysis. (109) Since the sample area possible for analysis is relatively small a carbon fibre rod (with a hollow diameter, see Figure 18) is used in order to mount the sample, avoiding any background elemental pick up that would otherwise be seen as interference.

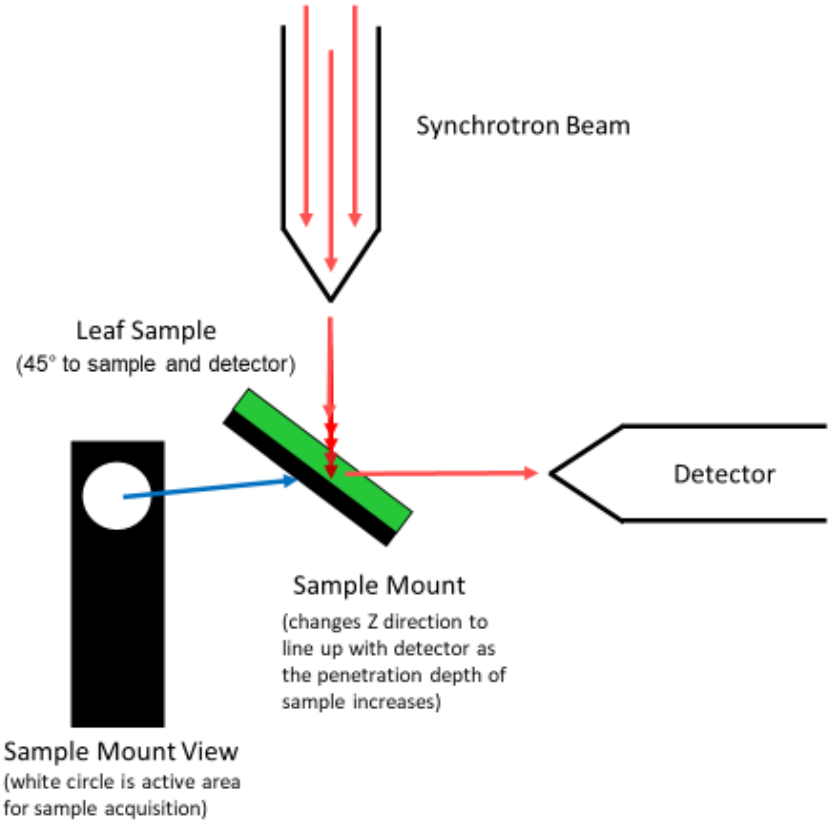

Figure 18: *Schematic representation of 3D Vortex detector Synchrotron XFM setup*

1.5.3.5 Confocal X-ray Imaging Optics

Confocal optics work by restricting the volumetric field of view of the detector, which enables the potential for depth-specific analysis, unlike the Maia detector which encompasses the entirety of the sample due to a backscatter setup. (109, 132) A much larger dwell time is needed depending on the scan range and sample concentration, this is in part largely due to the fact that the peak count rate is quite low 500 kHz when comparing to the Maia detectors 1.4 MHz. When conducting confocal XFM experiments it is imperative that the sample is as flat as possible to ensure the most

accurate depth analysis is conducted for anatomical accuracy. To help with the increase in dwell time a technique similar to the Maia's raster-scan acquisition is used for the vortex detector called 'list-mode'.

1.5.3.6 Confocal Imaging Capabilities

The unique capabilities of the vortex detector during XFM analysis allows the potential for confocal XFM imaging, which could provide better understanding into the elemental concentration and distribution changes that occur as a result of wheat fungal infections. Being able to understand how deep the infection effects the host source as well as defence mechanisms undergoing in response in an *in vivo* setting would provide new insight into an otherwise unknown area.

1.6 Overview and Aims

The primary focus of this thesis is the development and optimisation of bio-spectroscopic imaging techniques to investigate changes in epicuticular wax and metal composition during plant development and induced stress. This involves, Aim1: correlating alterations in the biochemical composition and distribution of epicuticular waxes (varying species and anatomical location). Aim 2: developing and applying a non-invasive protocol to monitor plant epicuticular waxes (caused by seasonal change, plant maturation, or disease), Aim 3: investigating diffusible metal cations (K^+, Ca^{2+}) of plant leaves in response to altered physiology caused by disease. The contents of each chapter and how aims will be investigated is detailed below.

Chapter 2: This chapter addresses all the methods used for experiments discussed in chapters 3, 4 and 5, outlining specific parameters, sample types and instruments used for analysis.

Chapter 3 (Aim 1): This chapter will demonstrate the use of benchtop ATR spectroscopic protocols to help characterise differences in the epicuticular wax layer with respect to bulk analytical techniques. Differentiation between eucalyptus species Karri, Marri, Tuart and Wandoo will be analysed via benchtop ATR and further

distinguished using principal component analysis (PCA). A study looking into anatomical regions including adaxial, and abaxial leaves during leaf maturation will be distinguished using spectroscopic protocols and validated with the use of SEM in order to verify that the wax changes observed are indeed a result of changes of chemical variation. This was further validated using Synchrotron ATR-FTIR microspectroscopy, which investigates variations in anatomy of epicuticular wax on the sub-cellular level. Finally, synthetic wax extractions are utilised to isolate components of epicuticular wax to distinguish potential changes associated with leaf maturation, adaxial/abaxial anatomical and species differences.

Chapter 4 (Aim 2): This chapter discusses the development and application of non-invasive protocols to monitor waxes as a function of plant health; validating infrared reflectance spectroscopic analyses of the epicuticular wax layer via application to four case studies:

1) Investigating age and seasonal variation in the epicuticular wax layer, with respect to anatomical structures of the plant leaf (stem, veins, cuticle, adjacent to cuticle) in eucalyptus species.

2) Investigating age variation in the epicuticular wax composition and distribution, with respect to anatomical structures of the plant leaf (stem, veins, cuticle, adjacent to cuticle) in eucalyptus species, under *in vivo* conditions.

3) Investigating changes in variation in the epicuticular wax composition and distribution during ethylene gas dossing in *Chamelaucium uncinatum* (Geraldton wax).

4) Investigating the impact of fungal infection on epicuticular wax and calcium oxalate composition and distribution in wheat (cv Magenta and Scout)

Chapter 5 (Aim 3): This chapter will describe the development and adoption of current Synchrotron XFM techniques to investigate plant health via diffusible ions K^+ and Ca^{2+} as biomarkers during infection. Case studies involving different wheat species

during Ptr infection were utilised, to gain a better understanding of metabolic processes involved during pathogenic attack, and how plants defend themselves in response. The development and monitoring of K^+ as a marker of plant health was investigated through means of traceability using a Rb^+ surrogate, due to low emission energies of K^+. Finally, the use of 3D confocal imaging was used to understand the effects of *Pyrenophora trictici-repentis* and how deeply it effects plant tissue using Ca^{2+} as a biomarker within the infection site.

CHAPTER 2

Experimental

2.1 Introduction

This chapter summarises the statistical, sample cultivation, and experimental methods used throughout this study. For the analysis of data collected in this research, a combination of chemometric analysis [principal component analysis (PCA)], *t*-tests, as well as one and two-way ANOVAS were used to compare data sets, with the choice of specific statistical approach dependent on the experimental design.

2.2 Plant Models Used to Develop and Test Spectroscopic Protocols for the Analysis of Epicuticular Waxes

This research used eucalyptus species as an experimental model to study epicuticular waxes. Eucalyptus species were chosen due to their abundance, ease to cultivate, and because their epicuticular wax layer has been well studied and characterised at the bulk and microscopic levels. Four different species of eucalyptus were chosen for these studies: *Eucalyptus diversicolor* (cv Karri); *Corymbia calophylla* (cv Marri); *Eucalyptus gomphocephala* (cv Tuart); and *Eucalyptus wandoo* (cv Wandoo or "white gum"). These 4 species of eucalyptus were used for ATR-FTIR method development studies (Chapter 3.2). Tuart was chosen for further studies developing *in situ* imaging and investigating ageing and seasonal variational changes. *Eucalyptus gomphocephala* (cv Tuart), *Eucalyptus Wandoo* (cv Wandoo), *Eucalyptus diversicolour* (cv Karri), *Corymbia calophylla* (cv Marri) were all locally sourced from a Western Australian plant farm, saplings were housed and maintained in 9 L plastic potting containers and were filled with local soil (swan coastal plain of Perth, Western Australia), and watered with reticulation twice a week, except for rain months in winter. Immature (<5 cm max length) and mature leaves (> 10 cm max length) from different seasons were taken for analysis, for multiple comparisons in infrared spectroscopy studies.

2.3 Model System to Investigate Flora Ripening on Epicuticular Wax

Chamelaucium uncinatrum commonly known as Geraldton wax in Western Australia was used as a model plant to study the effect of flora ripening on the epicuticular wax layer. Geraldton wax was chosen for this study due to its accessibility at Curtin University as it is a native Australian shrub that blossoms/grows through late winter – spring and is low maintenance. Geraldton wax was sourced from Curtin University, south of building 500 near PM3 parking lot where a variety of plants are located in urban greenery. Due to it's low-maintenance minimal water is needed for its upkeep, the Geraldton wax was harvested during blooming seasons (winter and spring) and needles roughly of the same size were collected for both immature and mature analysis.

The use of ethylene promoters with Geraldton wax samples was used to accelerate plant postharvest, as an experimental tool to study epicuticular waxes during plant maturation one common ethylene promoter which was used during this experiment is Ethephon (Figure 19). During this experiment two Geraldton wax branches of the same size were placed in 300 mL beakers with 50 mL of H_2O and placed in a large 25 L container. Within container 1, a 5 mL solution of sodium hydroxide (NaOH (10%)) was added to a 15 mL conical flask and added to the container. Within container 2, a 5 mL solution of NaOH (10%) was added to 0.5 mL Ethephon (480g/L) solution and the 15 mL conical flask was placed into the container. Time comparisons from 24, 48 hrs and a week were taken of triplicate needles (immature and mature).

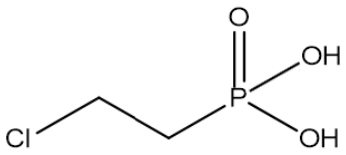

Figure 19: *Molecular structure of common ethylene promoter; Ethephon*

Figure 20: *25 L containers being filled with Geraldton wax and ethylene solution/procedural blank solution (left) Geraldton wax places in flask with ethylene/procedural blank solution placed next to it (right).*

2.4 Plant Models of Epicuticular Wax Changes during Crop Disease

The analytical methods developed in this thesis (infrared reflectance analysis of epicuticular waxes, X-ray fluorescence analysis of elemental plant nutrients), were subsequently applied to study crop disease. Specifically, two wheat cultivars were analysed (scout and magenta) with and without a common fungal infection, yellow spot disease. Wheat samples were cultivated by crop scientists within the Curtin Centre for Crop Disease and Management (CCDM), Fatima Naim and Lilian M.V.P Sanglard. *Triticum aestivum* (cv Scout) was the main wheat used for method development. A second wheat cultivar (cv Magenta) was also analysed in the final proof of concept studies. Wheat was utilised for the analysis of yellow spot disease caused by *Ptr*. (133) Wheat seeds were sown in 2.1 L pots and grown and maintained in Curtin University's glasshouse throughout the year. Glasshouse temperatures range between 10 and 25 ºC. The pathogenic isolate of Ptr, race 1 isolate M4 (ToxA and ToxC producing) was utilised for the inoculation of wheat leaves. The isolate was cultured following the growth conditions previously described by Moffat et al. (134) Conidia were harvested in water and a 10 µL droplet containing ~30 conidia was placed onto the adaxial side of the leaf. A single leaf of 6–7 week old plants was spot inoculated. Leaves were analysed ranging from 2-8 days post inoculation. To help facilitate infection, the glasshouse humidity was maintained at ≥95% via a fitted misting system (Idrobase Fog Extra, Italy) for 48 h (Figure 21).

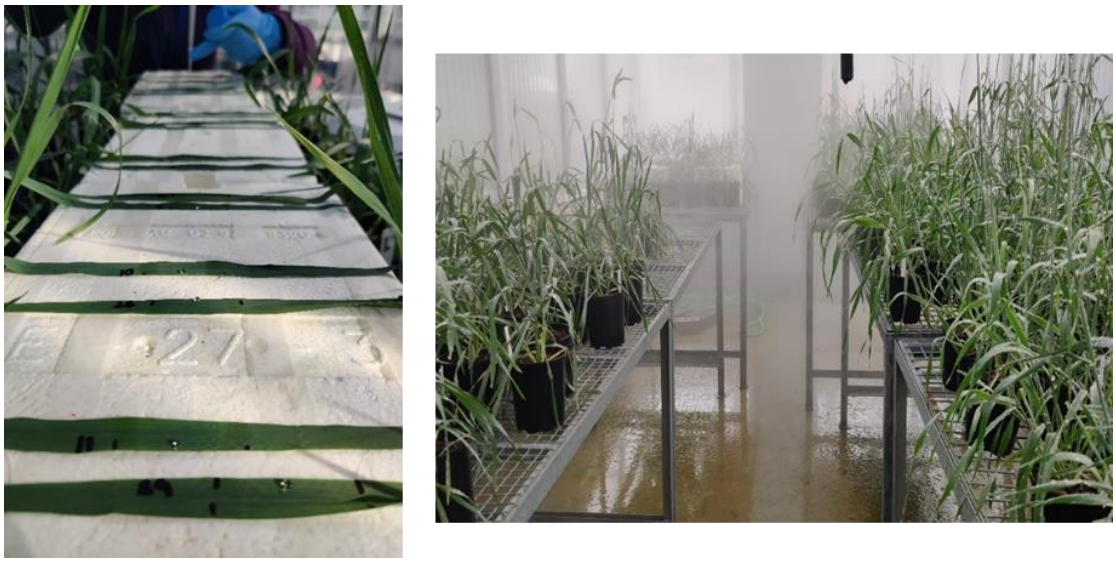

Figure 21: *Image of wheat leaves fixed on to a flat platform with 10 uL inoculation of Ptr placed on the leaf surface (left) glasshouse with misting system in action (right)*

2.5 Chemical Extraction and Analysis of Epicuticular Waxes

Eucalyptus *Marri* was extracted using two methods outlined below. The first method involved the general extraction of waxes from eucalyptus *marri*, entire leaves were submerged in ether and separated. The second method involved delicate cotton swabbing of *marri* leaves on both adaxial and abaxial sides in order to extract the epicuticular wax layer for the separation and purification of specific components.

Method 1:

To extract epicuticular waxes from the whole leaf surface, Marri leaves (110.61 g). were submerged in ether for 20 minutes (it is crucial to not submerge the leaves for too long, otherwise waxes from underneath the epicuticular wax layer will start to be extracted). The extract was reduced under pressure and ^{1}H NMR used to determine presence of fatty acids/aromatics. The fatty acid solid extracts were then separated by dissolution in dichloromethane (DCM) followed by vacuum filtration (crude yield: 1.24 g). Solid fatty acid crystals and a DCM solution was collected. The solid extract was dissolved in tetrahydrofuran (THF), a solid ppt was vacuum filtrated and the remainder solution was columned. The column was dry loaded with petroleum spirits 40-60 ºC (P.S (40-60 ºC)). 15% Ethylene acetate (EtOAc)/P.S (40-60 ºC) solution was used for the first 500 mL fraction. 30% ETOAC/P.S (40-60 ºC) were used to collect fractions 2-5 in which 2 fractions coeluted (3.25 L). 50 and 75% ETOAC/P.S (40-60 ºC) (100 mL each) was then used to check to see if anymore fractions remained. 5 Total fractions were collected and 1:99 methanol (MeOH)/DCM TLCs ran to ensure separation had occurred. Fraction 5 contained 2 fractions that co-eluted, and was recrystalised from MeOH. All fractions were analysed via ^{1}H NMR.

Method 2:

The second method allowed for an investigation into adaxial and abaxial epicuticular waxes in Marri leaves. One leaf was swabbed on the abaxial side with EtOAc using a cotton ball and the solvent evaporated under reduced pressure to yield an oil (5 mg). The same process was performed on the adaxial side of the leaf to give an oil (4 mg). The cotton ball was washed with MeOH to ensure all wax was released. An extraction to separate acids, phenols and neutral was conducted in 20 mL sample vials. $NaHCO_3$

(10 mL, 5%) was added to EtOAc (10 mL) solution containing the crude top lead wax. The organic layer was then washed twice with $NaHCO_3$ (10 mL, 5%), The aqueous solution was then acidified via HCl (36%) ~5 mL and organics extracted via EtOAc (30 mL x3). ^1H NMRs for all fractions were prepared.

2.6 Optimisation of Sample Preparation and Tissue Sectioning Parameters

Both cryo-microtome and microtome techniques were trialled to find optimal sectioning parameters. Common microtome embedding media involves paraffin and polyester waxes, however this was not suitable for these studies due to the ability of paraffin and polyester waxes to leach or redistribute the epicuticular waxes on leaf surfaces. When trying to section via microtome, it was found that eucalyptus leaves were too flexible, resulting fractionating/tearing. To counter this, a cryo-microtome was utilised due to its ability to increase sample rigidity through freezing. To prevent ice-crystal formation, rapid sample freezing is required. Liquid nitrogen was initially trialled however it is well known that a vapor barrier is easily formed due to its low heat constant, and often ends up acting as an insulator to the inner tissue sample, leading to slow and uneven freezing prone to fragmenting for large tissue samples. (135) Therefore, to increase rate of freezing, samples were flash frozen with a mixture of isopentane and liquid nitrogen slurry. Isopentane was utilised due to its high thermal conductivity, avoiding liquid nitrogen's formation of a vapor barrier. (136) Once the sample was flash frozen, the sample could be prepared for cryo-sectioning or stored in a -80 ^oC freezer for use at a later time.

Initial sectioning trials consisted of sectioning leaf samples with no embedding media, to emulate the closest possible "natural tissue section" however, it was found the leaf tissue was prone to shattering due to the thinness, and rigidity of the sample. An embedding medium optimal cutting temperature (OCT) was then trialled, on the sample, to help stabilise the tissue stabilisation, which was subsequently found to markedly improve section qualities (Figure 22).

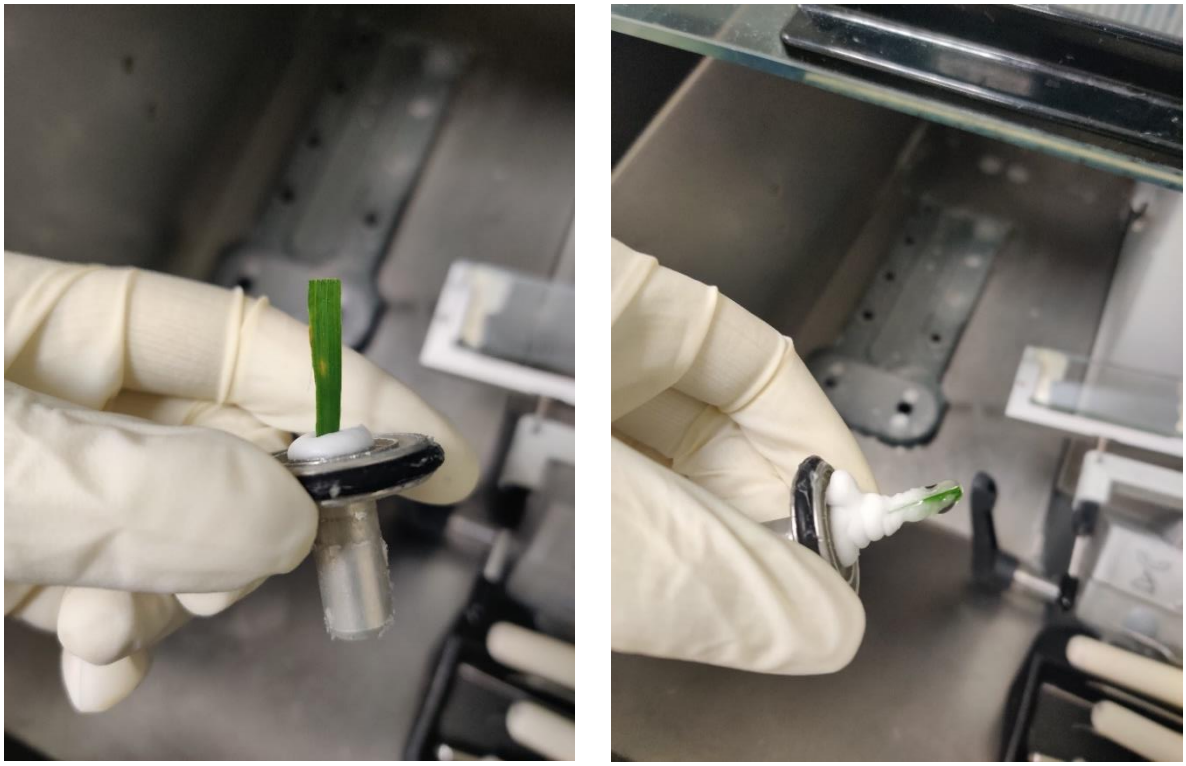

Figure 22: *Wheat embedded vertically on cryo-microtome sectioning mount (left), wheat embedded onto cryo-microtome mount with OCT embedding surrounding the tissue structure (right)*

OCT embedding is made up of non-reactive chemicals including polyvinyl alcohol and polyethylene glycol. (137) The benefits of using OCT as a cryo-sectioning embedding medium is due to its low solidifying temperature (-10 ºC) and its unreactive nature with biological samples. When using OCT, the optimum cutting temperatures were found to range from -15 ºC to -20 ºC. The optimal cutting temperature differed between species, with -17 ºC found to be optimal for Tuart leaves, while the optimal cutting temperature was -20 ºC for wheat variants Finally, the thickness of tissue sections is an important consideration for sample preparation. It was found that 15 µm was an optimum thickness for both eucalyptus and wheat samples, minimising the extent of section tearing, folding, and curling. A section thickness of 15 µm also assisted in sub-cellular imaging, as plant cells are typically around 50 µm in size.

All tissue which was sectioned for imaging was collected via CHIRIs Leica cryostat, housed at Curtin university, samples were embedded via OCT. Temperatures were kept at -18 ºC prior to sectioning and on average kept at ~ -20 ºC during sectioning. Samples were collected on CaF_2 disks, SiN chips or general microscope slides (Figure 23).

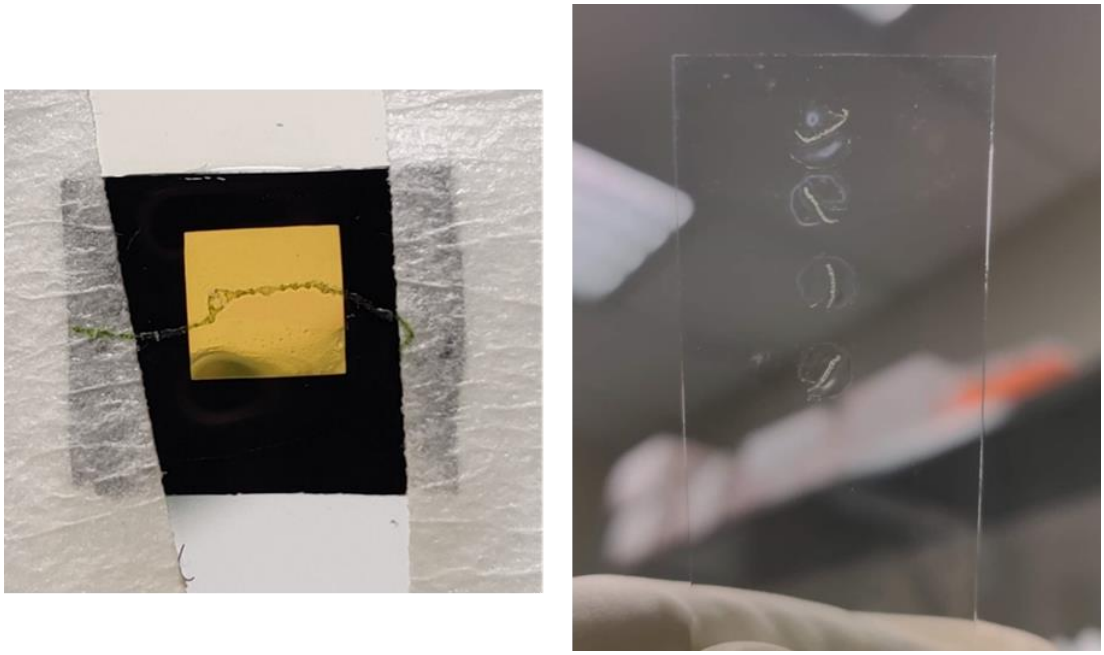

Figure 23: *tissue sections of wheat on silicon nitride chip (left) and microscope slide (right)*

2.7 General Optical and Fluorescent Microscopy Parameters

Fluorescent and optical images of eucalyptus leaves were captured using a fluorescent microscope at 4x and 10x magnification (Olympus upright BX-51 with Olympus DP70 camera and cellSens standard software) housed at Curtin University's CHIRI facilities. Optical images of eucalyptus and wheat were also collected at ANSTO's Australian Synchrotron Infrared Microscopy beamline using an optical stereomicroscope (Leica MZ7.5).

2.8 Benchtop Attenuated Total Reflectance – Fourier Transformed Infrared Spectroscopic Analysis of Eucalyptus Leaves

ATR studies were performed at Curtin University's chemistry building using a Nicolet iS50, ThermoFisher Scientific spectrometer. This spectrometer works on a single-bounce (reflects once) ATR module, and includes a diamond crystal with a refractive index of 2.4, KBr beam splitter (350 – 7800 cm^{-1}), tungsten-halogen white light source, with a deuterated triglycine sulfate (DLaTGS) detector. ATR-FTIR studies were mainly used on the four eucalyptus variants to investigate wax differences between species on an overall unspecified anatomical region for both adaxial and abaxial, immature and mature leaf studies. A background scan consisting of 256 scans was done before every leaf analysis to keep consistent with slight environmental changes within the lab, leaf samples were analysed with 64 scans at a spectral resolution of 4 cm^{-1}. For solid samples a pressure arm is used to ensure contact between the sample and the diamond is consistent, due to leaves being very soft in nature as a solid sample, when pressure from the arm was applied, the sample often squished letting out the contents from inner tissue as which often led to huge water peaks and inaccurate chemical information pertaining to the epicuticular wax layer. To counteract this, a spatula between the sample and pressure arm was placed to disperse the pressure that was centralised at its point region into a wider area, ensuring that the leaf sample was still maintaining sufficient contact, but the data obtained was only coming from the outermost epicuticular wax layer on the surface of the leaf (Figure 24). All data was ATR corrected, and spectra were analysed via OPUS v7.0 software. Statistical analysis for ATR-FTIR was undertaken using principal component analysis for four eucalyptus species Karri, Marri, Tuart and Wandoo. Separation based on overall ATR spectra (400 – 4000 cm^{-1}) corrected for CO_2 was used with 5 replicates per species (n=5). All principal component analysis data was processed using Unscrambler v10.1.

Figure 24: *Spatula implemented between pressure arm and sample utilised for eucalyptus ATR analysis.*

5 immature (<5 cm max length) and mature leaves (< 10 cm max length) of each eucalyptus species *karri, marri, tuart* and *wandoo* were picked for ATR-FTIR studies on the same day and atmospheric conditions, all spectra were ATR corrected upon collection. The ATR crystal was cleaned with ethanol upon every spectrum collected, and new background references were taken after each leaf.

2.9 Analysis of Leaf Surfaces with Benchtop Fourier Transformed Infrared Reflectance Microscopy

FTIR reflectance microspectroscopic imaging was carried out at Curtin University's chemistry building using the Nicolet iN 10MX FTIR microscope, an 8 x 2 pixel liquid nitrogen cooled linear array detector, and 25 µm pixel size. Spectra were collected using 4 cm^{-1} spectral resolution with 16 co-added scans. When choosing a background reference for the reflectance spectra collected a range of metals were tested including

gold disks, aluminium disks, and aluminium foil. When picking a suitable background, a greater signal from the metal over sample is desirable, in this case all 3 background references tested were suitable, out of the 3 aluminium foil is more economically advantageous due to the ability to readily use new foil if it gets damaged or dirty, in comparison to the plates which are not only expensive, but are prone to scratching, leading to a reduced signal. The aluminium foil signal was reproducible consistently, and so reflectance images were collected from the surface of the foil under the same conditions and using the same parameters. FTIR-reflectance spectroscopy studies were undertaken for eucalyptus tuart, Geraldton wax needles and wheat scout and magenta varieties. Eucalyptus seasonal, age and live *in vivo* imaging between time points were undertaken, in the case of live *in vivo* imaging extra care had to be taken when placing the leaf to the IR motorised microscope mapping stage so that the leaf does not tear from the mounted plant, extra care was also taken when taping the leaf to aluminium foil in order to ensure the leaves tip and stem do not tear or get damaged during the imaging process (Figure 25). Statistical analysis for FTIR reflectance spectra using two-way ANOVA (unless otherwise stated via one-way ANOVA or *t*-tests where suitable) were performed using second-derivative intensity and position of the $\nu_s(CH_2)$ absorbance bands as the dependant variable, where leaf maturity, seasonal variation, anatomical region, ethylene gassed and infected leaves as independent variables. If significant statistical differences were identified via two-way ANOVA, post hoc testing was performed using *t*-tests, corrected for multiple comparisons using the Bonferroni method and alpha of 0.05 (two-tail testing). Statistical analysis was performed using GraphPad Prism v7.04.

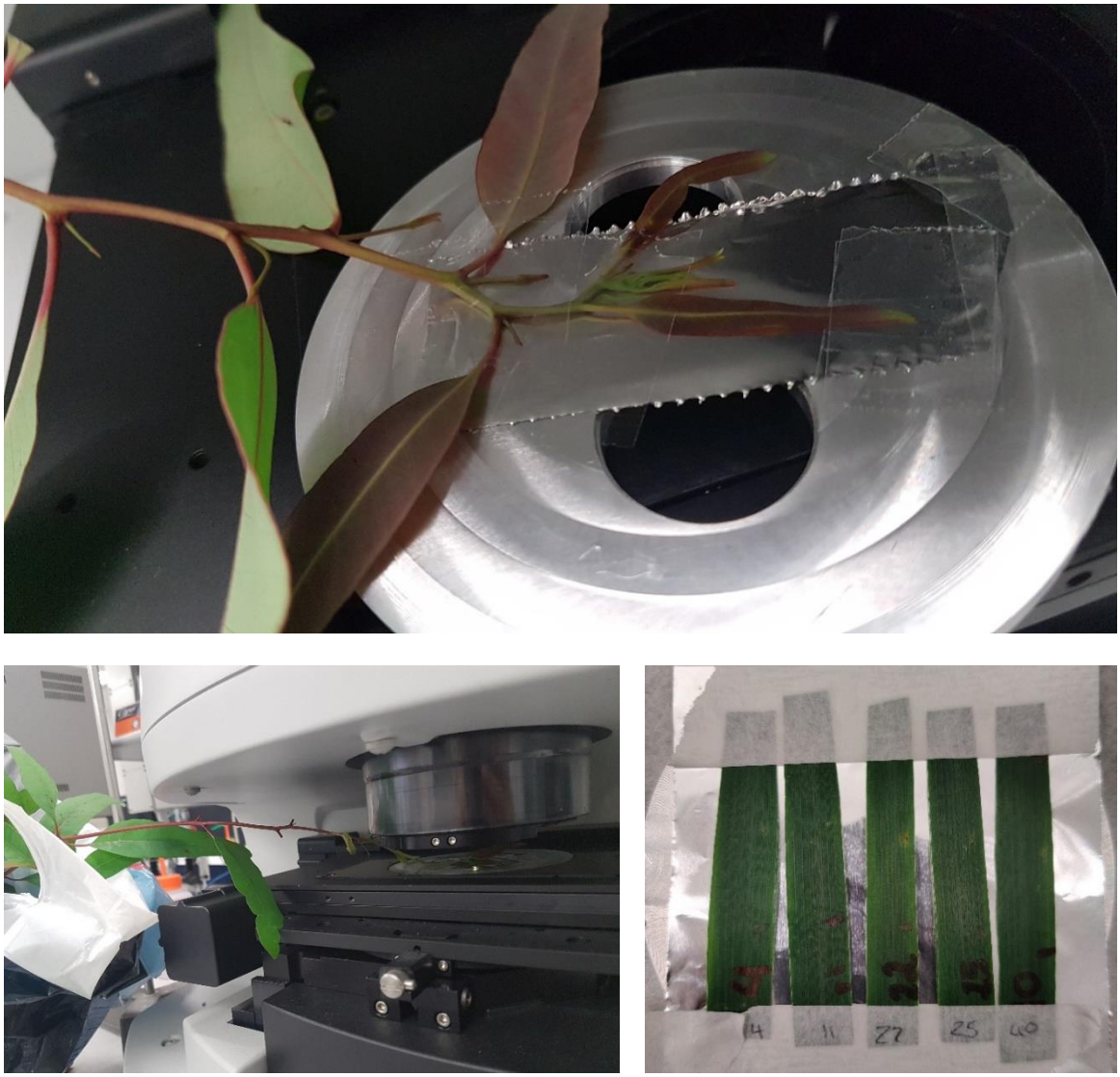

Figure 25: *live in vivo imaging of eucalyptus plant (top, bottom left) example of sample mounting for ex vivo wheat and eucalyptus leaves aluminium foil directly under sample (right)*

Geraldton wax ethylene gassing experiments involving different time points and immature/mature needles, and wheat studies involving control and Ptr infections along with different time points post infection were investigated. Spectra were analysed via OPUS v7.0 software and images were produced via Cytospec v2.00.03 and imageJ v1.50i for analysis.

2.10 Analysis of Leaf Sections with Focal Plane Array FTIR Spectroscopic Imaging

Fourier transform infrared spectroscopic imaging was undertaken at the IRM beamline at ANSTOs Australian Synchrotron. Eucalyptus leaves and K^+/Rb^+ doused wheat data were analysed. Both transmission and reflection techniques were trialled. Transmission imaging of the leaf sections were collected on CaF_2 windows using an offline Bruker Hyperion 2000 FTIR microscope, equipped with a liquid-N_2 cooled 64 x 64 element FPA detector and a 15x objective lens with numerical aperture (NA = 0.4), coupled to a Vertex 70 FTIR spectrometer (Bruker Optik GmbH, Ettlingen, Germany) (Figure 26).

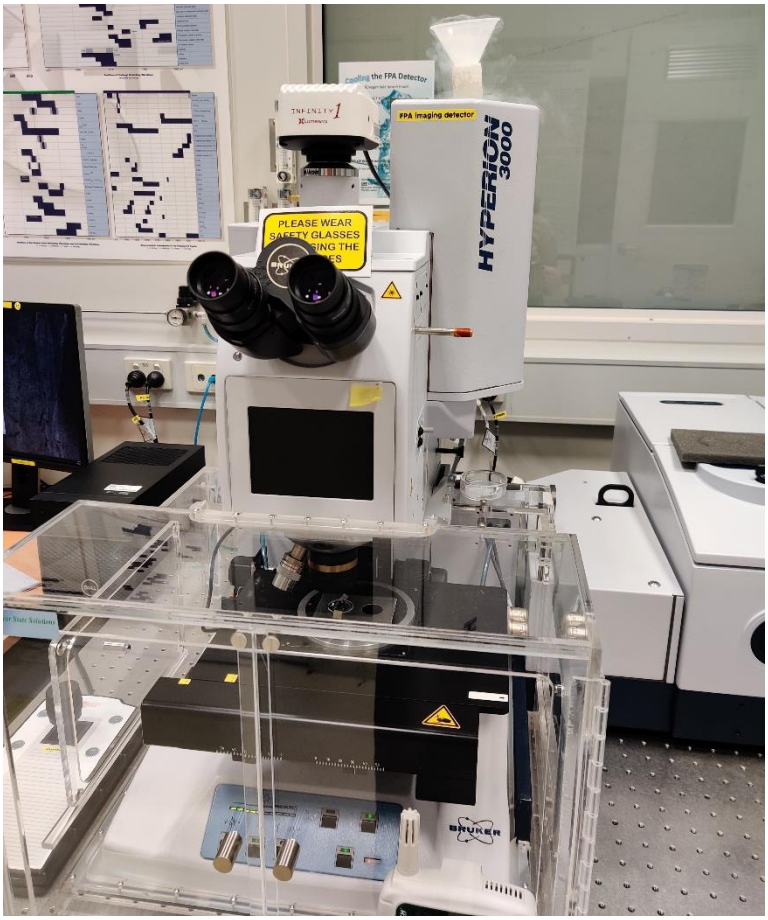

Figure 26: *Image of FTIR general set up with Focal Plane Array detector*

Under this optical configuration a single spectrum in each FTIR image represented molecular information acquired from a ~2.67 x 2.67 μm^2 area on the sample plane.

The spectral images were collected at 4 cm^{-1} spectral resolution, with 256 co-added scans using OPUS v7.2 imaging software. Background measurements were taken prior to sample spectral images, by focusing on a clean surface area of the CaF_2 substrate using the same acquisition parameters. When attempting reflectance imaging a background signal was never able to be obtained using a gold and aluminium disk as as background references, possibilities for this could be due to the numerical aperture (0.4) and 15x objective when comparing to the Nicolet iN 10MX FTIR microscope (0.7), however further investigations would be needed to confirm this. Data was analysed via OPUS v7.0 software and false colour images were further processed via Cytospec v2.00.03 and imageJ v1.50i software.

2.11 Synchrotron Attenuated Total Reflectance – Fourier Transformed Infrared Spectroscopic Analysis of Leaf Surfaces

Synchrotron ATR-FTIR was undertaken at ANSTOs Australian Synchrotron IRM beamline using the macro-ATR accessory, previously described by Meguya Ryu, et al. (138) The setup for the synchrotron macro ATR-FTIR uses a Bruker Vertex 80v spectrometer coupled with a Hyperion 3000 FTIR microscope, equipped with a liquid nitrogen-cooled (12-14 h) narrow-band mercury cadmium telluride detector (Bruker Optik GmbH, Ettlingen, Germany) (Figure 27).

Figure 27: *General ATR set up microscope and detector (left), Synchrotron ATR-FTIR beam mirrors/optics focus (right)*

Data collection was controlled using OPUS v7.2 software suite (Bruker Optik GmbH, Ettlingen, Germany). The macro-ATR-FTIR device was equipped with a germanium (Ge) ATR hemispherical crystal (*n*Ge = 4.0), which had a 250 µm diameter active sensing area. The optics incorporate a 20x IR objective (NA = 0.60, Bruker Optik GmbH Ettlingen, Germany). A background spectrum was recorded in air using 256 co-added scans and the sample spectra were recorded using 4 co-added scans once contact was made between the ATR crystal and leaf sample. The sample was mapped with the beam focus size of 1.9 µm and an effective step size of 0.5 µm. The spectra collected were recorded within a spectral range of 950-3800 cm^{-1} using 8 cm^{-1} spectral resolution. Scans were capped at ~8/9 hrs (overnight) and on average ran for 2-5 hrs depending on the plant tissue/stomata cells being investigated. Commonly, when you are undertaking macro-ATR-FTIR scans a nitrogen purge is undertaken to avoid atmospheric water vapour interferences with the spectra signal obtained, however due to leaf tissue being susceptible to drying out over time it was avoided to ensure that optimal lipid signals (2800-3000 cm^{-1}) were obtained as well as sample longevity. Synchrotron ATR-FTIR was conducted on eucalyptus species as a proof-of-concept study to be able to investigate changes in lipids seen on the epicuticular wax layer, investigations into Ptr infected wheat were also undertaken as a result looking into the effects of Ptr at the site of infection and adjacent tissue. Leaves were prepared by cutting a 2 cm^2 section of leaf and mounting it on an aluminium disc with double sided sticky tape, the sample was then raised, so that the top (adaxial) side of the leaf was in contact with the ATR crystal, scans were started as soon as possible to ensure the tissue stayed as fresh as possible. All spectra collected were ATR and atmospheric compensation corrected and data was analysed via OPUS v7.0 software, false colour images were produced using Cytospec v2.00.03 and imageJ v1.50i software.

Eucalyptus *leucoxylon* leaves were mounted to the synchrotron ATR podium where contact is made with a clean hemispherical germanium crystal ensuring that enough contact was made to get a clear signal, whilst keeping the leaves integrity intact. Analysis ensued following the methods outlined above, large “coarse” areas were used as cellular identification compromising of 2 µm step size and ranging in pixel size depending on the size of the cell. While for smaller “fine” sub-cellular scans a step

size of 0.5 µm was utilised to ensure sub-cellular detail could be seen and as a result the pixel area size was greatly reduced to ensure viable mapping times.

2.12 Elemental Mapping of Intact Leaves and Leaf Sections with 2D (MAIA) and 3D (Vortex) X-ray Fluorescence Microscopy

2D and 3D elemental mapping of wheat leaf sections and whole leaves were undertaken at ANSTO's Australian Synchrotron XFM beamline. The instrumental setups for both 2D and 3D imaging using two different MAIA and Vortex detectors are outlined in Daryl L. Howard et al. (109, 139, 140) A monochromatic incident beam of 15.8 eV is focused using a Kirkpatrick-Baez mirror microprobe and slits to an approximate size of ~1 µm spot on sample leaves. During 2D imaging X-ray emissions were acquired via low latency 384 channel Maia detector running in event mode to improve data acquisition times. The sample was mounted directly in front of the incident beam and the Maia detector positioned behind to allow for backscatter geometry thus allowing improved sensitivity (Figure 28).

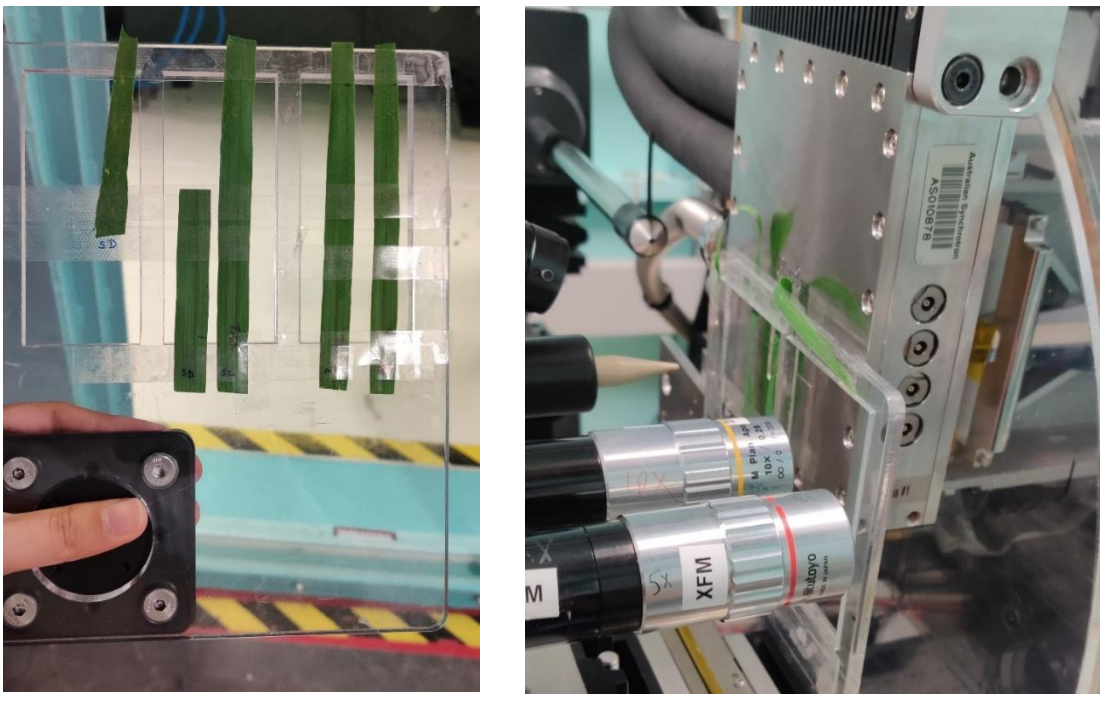

Figure 28: *Sample mounting and placement 2D Maia XFM imaging, samples located directly in front of incident beam and detector located behind.*

During 3D imaging X-ray emissions were collected via four-element Hitachi Vortex ME3 silicon drift detector, similarly to the Maia's event mode the vortex data is run in list mode to improve acquisition times. 3D imaging differs slightly to 2D imaging in mounting and detector placement, to avoid picking up scattering signals, while the sample is mounted directly in front of the incident energy it is mounted at a 45 º angle, as such the detector is placed at a right angle relative to the incident energy beam (Figure 29).

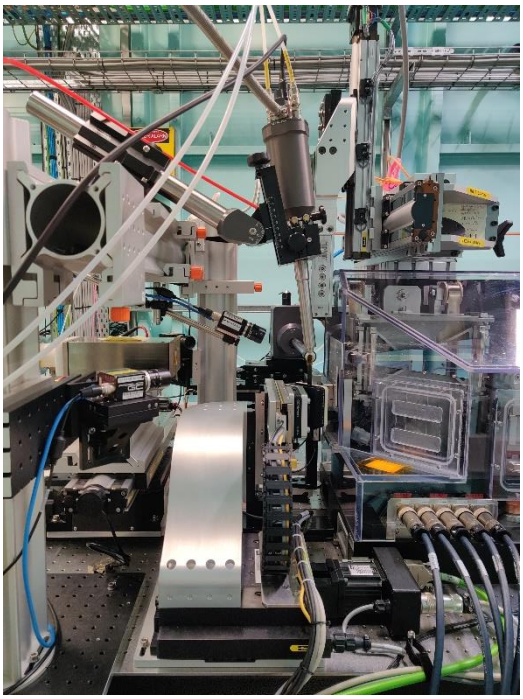

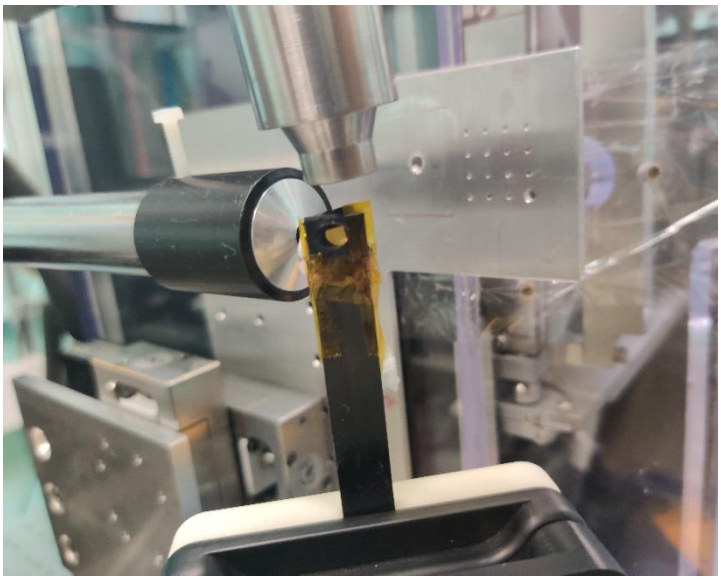

Figure 29: *Sample mounting and placement, for 3D XFM confocal imaging, Vortex detector seen at a right angle relative to incident beam, and sample mounted at a 45 º angle with cryo-stream found directly above.*

A cryostream is also equipped directly above the sample mount to maintain tissue integrity and stop the sample from any movement that may come about during natural drying of the tissue. In both 2D and 3D imaging cases the samples are raster scanned relative to the beam, in 2D imaging a conventional x, y, z directional movement is used however in the case of 3D imaging it slightly changes to compensate the 45 º angle sample location resulting in x', y and z' directional movement. Elemental foils

(Micromatter, Canada) with a known composition were used to calibrate data. Both tissue sections and whole wheat leaves were analysed during this study, to make sure accurate elemental quantification values the density and air pathing between the sample and detector were taken into consideration. During 2D imaging, sectioned 15 µm and whole wheat (cv Scout) leaf samples doused with and without varying concentrations of Rb^+ and infected with Ptr were analysed at 10 µm spot sizes, with a dwell time of 1 ms per pixel at 18500 eV. 3D imaging samples were collected in 10 µm cross section increments of wheat doused with and without enrichment Rb^+ collected with a 1 ms dwell time and 1 micron step size. Data was analysed and extracted into workable elemental map TIFF files using ASCI Geopixie software, images were further processed through ImageJ v1.50i software.

2.13 Scanning Electron Microscopy

SEM images of both eucalyptus and wheat leaves were taken using GRDCs Joel JCM-6000 plus at Curtin University. A sample of approximately 1 cm^2 section of leaf was deposited onto a SEM stub using carbon tape, making sure not to touch the area of interest to ensure that the crystal images obtained of the wax were untouched (Figure 30).

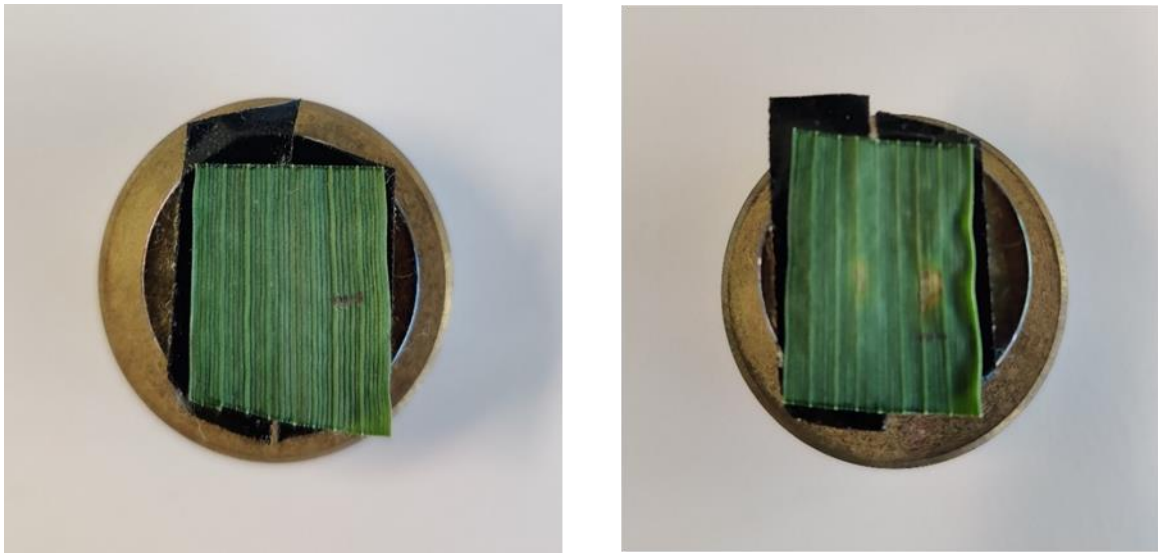

Figure 30: *Mounted images of wheat sections prepared for SEM imaging control (left) infected (right)*

The stub was coated with gold at an elevation height of 20 cm for 2 minutes using a smart coater (DII-29030SCTR) just before imaging. To avoid any tissue damage energy levels were kept around 5 kV when imaging, it was found at around 10-15 kV the tissue would damage before imaging could take place, and stomata would often change morphological shape almost immediately. Images ranging from 10 µm – 200 µm in size were collected and analysed for epicuticular wax differences of both healthy and infected tissue as well as immature and mature tissue.

CHAPTER 3

A Proof of Concept: Detecting Epicuticular Wax Distribution Using Attenuated Total Reflectance – Fourier Transformed Infrared Techniques

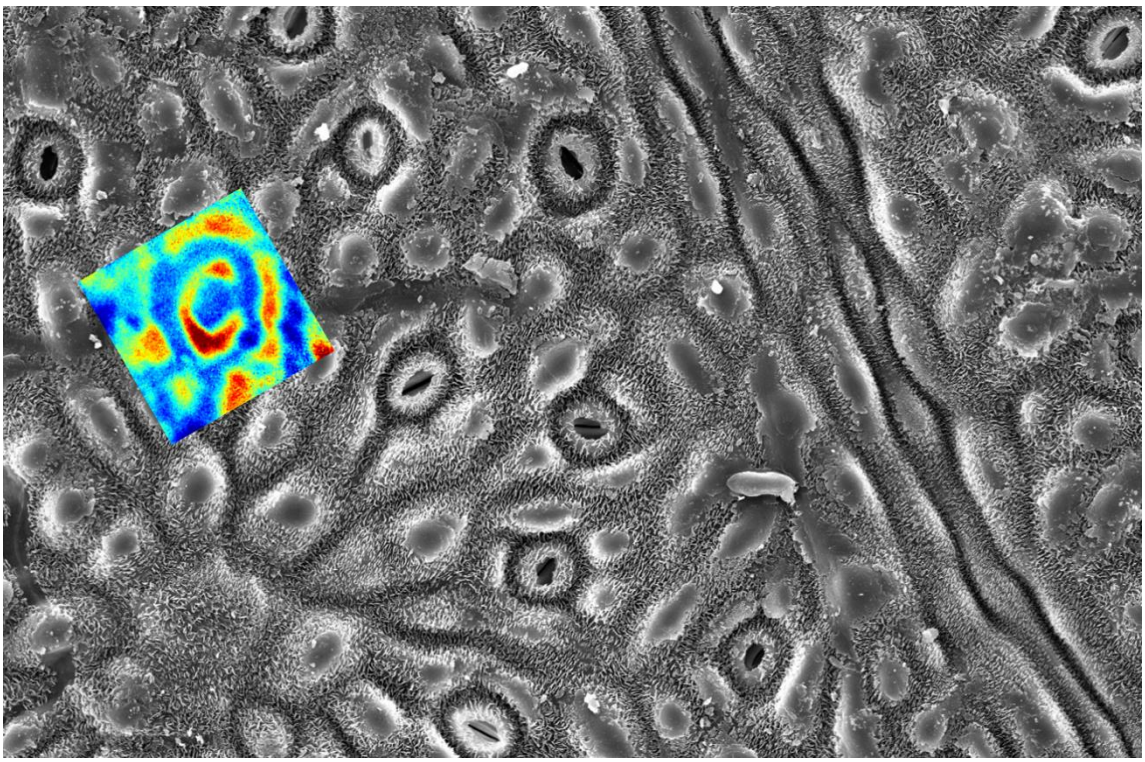

Components of the following chapter has data previously published in Royal Society of Chemistry: Jitraporn Vongsvivut, David Pérez-Guaita, Bayden R. Wood, Philip Heraud, Karina Khambatta, David Hartnell, Mark J. Hackett, Mark J. Tobin, ***Synchrotron macro ATR-FTIR microspectroscopy for high-resolution chemical mapping of single cells*** Analyst **2019** *144*, 3226-3238
DOI: 10.1039/D1AN90049H

3.1 Introduction

Monitoring the effects of seasonal variation, changing climate, soil quality, and disease on plant fitness is important to both agricultural and environmental industries. In particular, the ability to develop methods capable of robust assessment of plant health, *in situ*, or *in vivo* is sought after. As already described in chapter 1, the epicuticular wax layer is sensitive to plant fitness, and due to its location on the leaf surface, analysis of epicuticular wax is compatible with *in situ* or *in vivo* assessment of plant health. The primary aim of this chapter was to investigate the capabilities of Fourier transform infrared (FTIR) spectroscopy for detecting chemical difference between epicuticular waxes, using a series of model experimental systems. As epicuticular waxes are located on the surface of plant leaves, the surface sensitivity of attenuated total reflectance (ATR) – FTIR spectroscopy has been used for experiments in this chapter.

Eucalyptus species are easily recognised by their epicuticular wax coating, which gives rise to the characteristic touch and appearance of their leaves. Not surprisingly, due to the range of climates and growing conditions that Eucalyptus species have adapted to, there is well established variation in the epicuticular wax layer between species. Therefore, Eucalyptus species are well suited as a readily available, low maintenance, model system to develop and test capabilities for *in situ* analysis of the chemical composition of epicuticular waxes. To demonstrate proof-of-concept, ATR-FTIR spectroscopy has been applied in this chapter to detect changes in epicuticular wax composition associated with inter-species variation, and intra-plant variation (i.e., variation in wax composition between different anatomical regions, such as adaxial and abaxial leaf surfaces). While the ATR-FTIR spectroscopic measurements were found to differentiate between eucalyptus species, and between different anatomical regions, an association between leaf surface morphology and spectroscopic signal was observed. This highlights that ATR-FTIR spectra do require interpretation with caution, and with consideration of sample surface morphology (which can affect the degree of contact made with the leaf surface, influencing signal strength).

After validating the capability of FTIR spectroscopy to detect changes in epicuticular waxes, this chapter has investigated the spatial resolution that ATR-FTIR

spectroscopy can provide, the extent to which wax distribution and be related to plant leaf anatomy. Specifically, ATR-FTIR-spectroscopy was optimised at a synchrotron radiation light source, to provide a method capable of imaging (mapping) wax distribution on the leave surface at sub-cellular spatial resolution. Although ATR-FTIR spectroscopy was shown capable of studying epicuticular waxes, at the cellular level, the results also highlight the method is destructive as a result of contact between the sample and ATR crystal. Therefore, ATR-FTIR spectroscopy was shown to be compatible with *in situ* assessment of epicuticular waxes, but not longitudinal *in vivo* monitoring. Lastly solvent extractions of the epicuticular wax layer were undertaken using ether washes, and various purification methods to elucidate individual species present within the epicuticular wax layer, for further identification using ^{1}H NMR techniques.

3.2 Results and Discussion

3.2.1 Investigating the Capability of ATR-FTIR Spectroscopy to Detect Differences in Epicuticular Wax Composition in Four Eucalyptus Species

In this experiment, ATR-FTIR spectroscopy was applied to detect changes in the chemical composition of epicuticular waxes between four different eucalyptus species (cv Karri, Marri, Tuart and Wandoo). The ν(C-H) stretching region (2800 – 3000 cm^{-1}), more specifically, methyl $\nu_s(CH_3)$ 2860 – 2880 cm^{-1} and methylene $\nu_s(CH_2)$ 2840 – 2860 cm^{-1} stretching modes were chosen as spectroscopic markers to investigate epicuticular waxes. ATR-FTIR spectra were collected from five replicate leaves from the four Eucalyptus species (cv Karri, Marri, Tuart, Wandoo). The comparison of average spectra showed large inter-species variation was observed with respect to the intensity of absorbance bands attributed to epicuticular waxes ν(C-H) 2800 – 3000 cm^{-1}, ester carbonyl ν(C=O) 1700 – 1770 cm^{-1} and δ(C-H) 1400 – 1480 cm^{-1}, as shown in Figure 31**A-D**.

To better understand the inter-species spectroscopic variation, chemometric analysis was undertaken to confirm whether spectra contained sufficient chemical information to differentiate between the four eucalyptus (karri, marri, tuart, and wandoo) species. As can be seen in Figure 31**E,F**. principal component analysis of ATR-FTIR spectra collected from either adaxial or abaxial leaf surfaces provided good ability to differentiate between the 4 different species. The best visual separation between species, for spectra collected from adaxial leaf surfaces was observed in the 2D PC score plots of PC1 vs PC3. The best visual separation between species for spectra collected from abaxial leaf surfaces was seen for the 2D PC scores plots of PC1 vs PC2. Not surprisingly the PC2 loadings for PC1 and PC3 (Figure 31**G,H**) and PC1 and PC2) show strong loadings in spectroscopic regions corresponding to the absorbance bands of waxes [ν(C-H) 2800 – 3000 cm^{-1}, ester carbonyl ν(C=O) 1700 – 1770 cm^{-1}) and δ(C-H) 1400 – 1480 cm^{-1}]. Interestingly, spectra collected from the Tuart eucalyptus species showed the largest visual separation from other eucalyptus species, for spectra collected from both abaxial and adaxial leaf surfaces.

The results from PCA analysis of ATR-FTIR spectra collected from the 4 different eucalyptus species agree well the literature, specifically it is well established that different eucalyptus species can have widely varying epicuticular wax content. (141-143) These results therefore, help demonstrate the suitability of ATR-FTIR spectra to identify difference in plant biology through analysis of the epicuticular wax layer. Due to the large differences seen in the wax layer of the tuart species, this species was chosen for further intra-species analysis to investigator how the epicuticular wax layer changed as a function of plant anatomy (adaxial vs abaxial leaf surface) and plant age (immature vs mature leaf age).

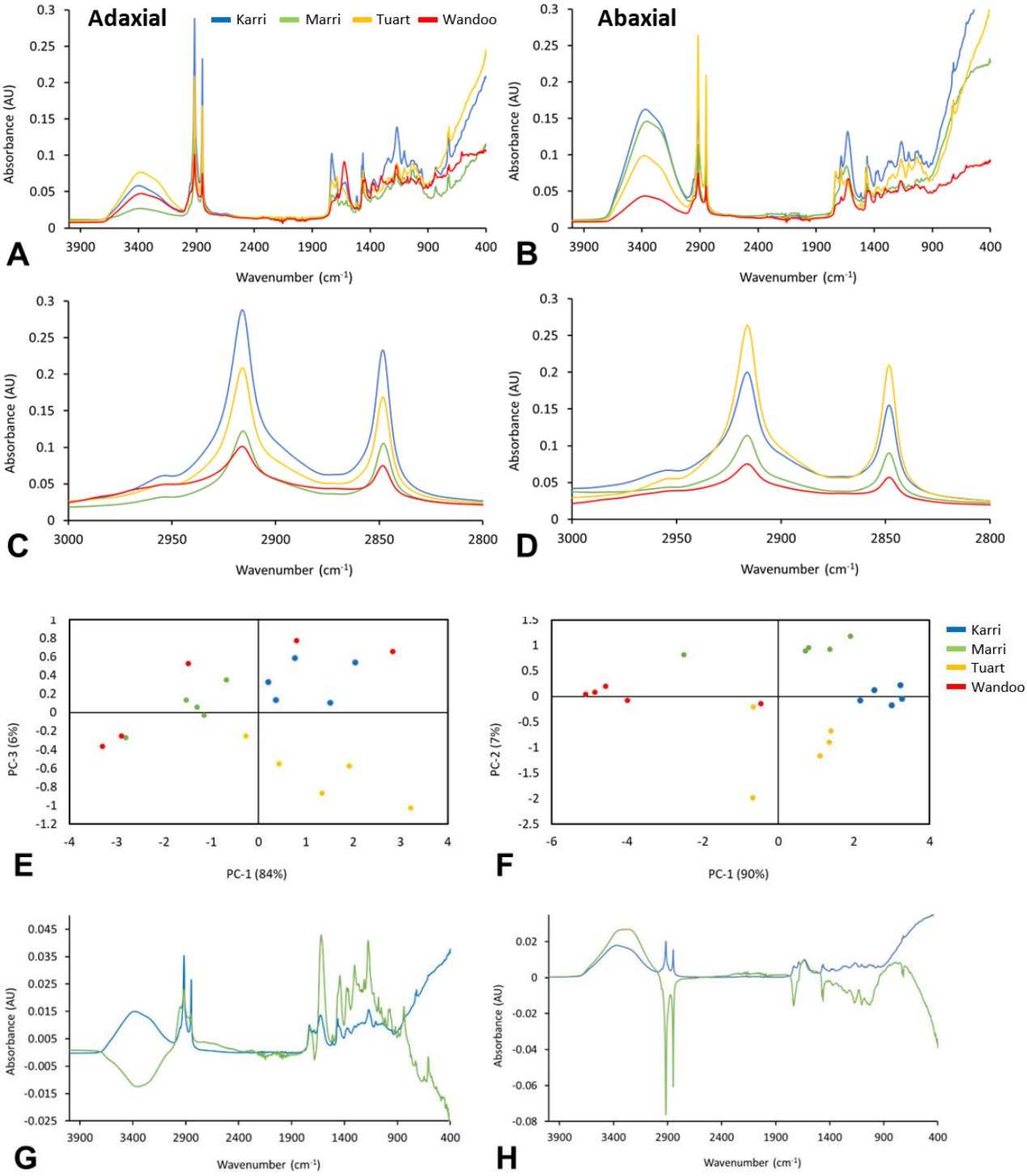

Figure 31: *ATR-FTIR overview spectra of four **mature** eucalyptus species (adaxial left, abaxial right) (Karri: blue, Marri: green, Tuart: yellow, Wandoo: red) and zoomed in ν(C-H) (2800-3000 cm^{-1}) region, demonstrating disparity in wax (lipid) content between species **A-D**. 2D score plots from PCA showing the distribution of four eucalyptus species Karri (blue) Marri (green) Tuart (yellow) Wandoo (red) comparing species grouping for different anatomical regions (adaxial left, abaxial*

*right) in mature leaves **E,F**. Factor loading distributions (adaxial left, abaxial right) showing where principal component PC-1 (blue), PC-2 (right, green), and PC-3 (left, green) separation has been attributed to for different eucalyptus species **G,H**.*

3.2.2 Investigation of Epicuticular Waxes in Different Leaf Regions: A Comparison of ATR-FTIR Spectra Collected from Abaxial and Adaxial Leaf Surfaces

The eucalyptus gomphocephala (*tuart*) species was chosen to investigate if ATR-FTIR spectra detect differences in epicuticular waxes located on the adaxial or abaxial leaf surfaces. On average the abaxial surface displayed greater intensity (relative to adaxial surface) for absorbance bands associated with epicuticular waxes, [ν(C-H) 2800 – 3000 cm^{-1}, ester carbonyl ν(C=O) 1700 – 1770 cm^{-1}) and δ(C-H) 1400 – 1480 cm^{-1}]. The results seen in Figure 32**A,B** seemed somewhat surprising, as the literature generally indicated increase wax content on the adaxial (sun facing) surface, in order to better protect the plant from water loss however, initial ATR results showed an increase of overall wax signals on the abaxial surface of the leaf. (4) Therefore, to help explain the unexpected differences in ATR-FTIR spectra collected from abaxial and adaxial leave surfaces, SEM imaging was undertaken. When looking at the adaxial and abaxial leaf surfaces as seen in SEM images Figure 32(**C-D**), clear difference in the wax distribution and structure was seen on surface. Specifically, the adaxial surface appears to have large columns of wax in between smaller needle like crystalline features (Figure 32**C**). In contrast, the abaxial surface appear to be devoid of large column like structure, containing only finely intertwined needle like crystal structures (Figure 32**D**). These visual comparisons of SEM images appear consistent with the literature, and indeed based on surface coverage and the size of the "column like structures" one would expect the adaxial surface to contain the greater wax content (relative to the abaxial surface). (144, 145) The SEM images however, highlight that irrespective of wax content, the surface topology is different between abaxial and adaxial surface. This is an important consideration for ATR-FTIR spectroscopy, due to the short-penetration depth of the evanescent wave, the majority of the spectral signal come from the first micron above the crystal surface. Consequently, flat sample surfaces that maximise surface contact between sample and crystal result in strong spectral signal unlike irregular surfaces. It is therefore, concluded that the stronger

intensity observed in ATR-FTIR spectra of the abaxial surface is not the result of increased wax content, but rather the result of more homogenous and evenly distributed wax structures that give rise to better surface contact with the ATR crystal. This highlights an important limitation of the ATR-FTIR method, that while it is well suited for *in situ* measurement of sample surfaces, quantitative analysis is often difficult (or impossible) when surface morphology differs between samples.

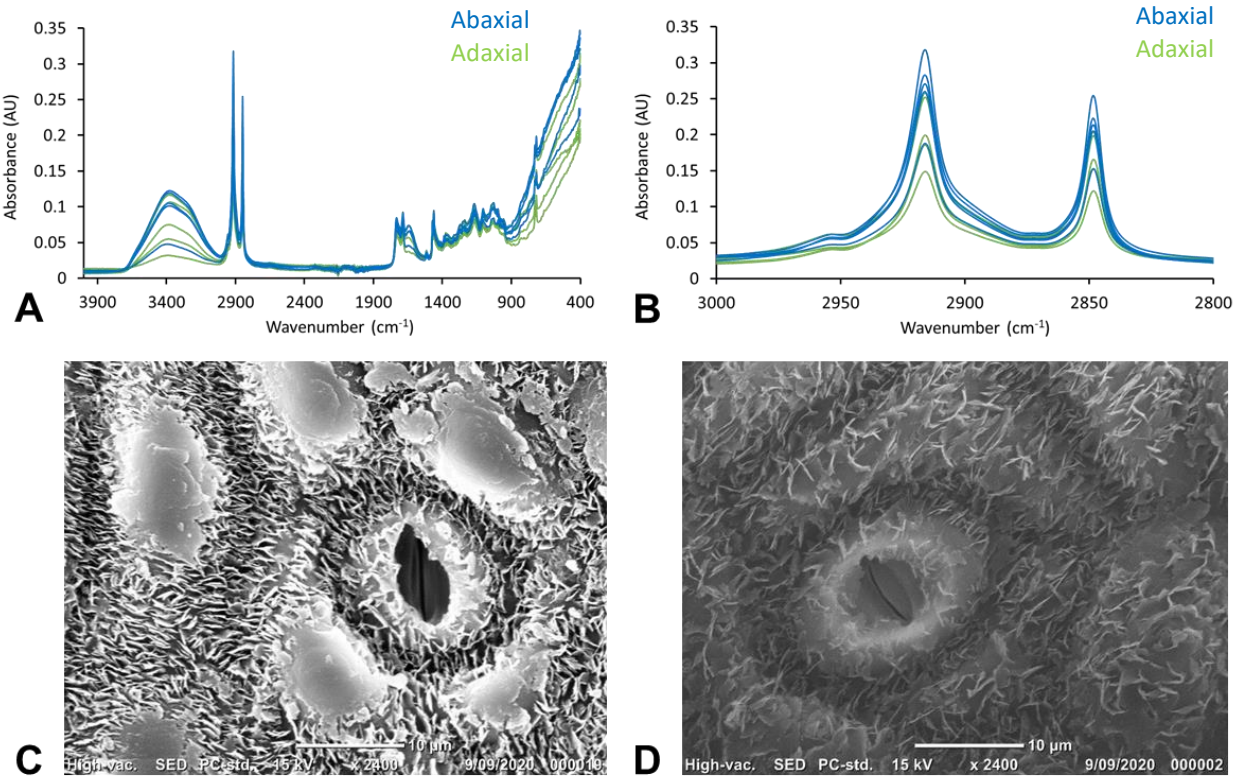

Figure 32: *ATR-FTIR individual spectra of **mature** eucalyptus tuart (5 adaxial (green), 5 abaxial (blue)) in overall (400-4000 cm^{-1}) and lipid C-H (2800-3000 cm^{-1}) stretching regions, demonstrating disparity in wax (lipid) content between adaxial and abaxial surfaces **A, B**. SEM images of eucalyptus tuart mature leaves adaxial (**C**) displaying "column like" structures throughout the plant tissue, and abaxial (**D**) displaying distribution of epicuticular wax crystallinity scale = 10 µm.*

When comparing spectra of immature adaxial and abaxial eucalyptus *tuart* leaves, consistent spectral differences between adaxial and abaxial spectra was not observed, with respect to absorbance bands associated with epicuticular waxes [ν(C-H) 2800 –

3000 cm^{-1}, ester carbonyl ν(C=O) 1700 – 1770 cm^{-1}) and δ(C-H) 1400 – 1480 cm^{-1}] (Figure 33**A,B**). Further investigations with SEM imaging revealed very similar morphology between the adaxial and abaxial leaf surfaces (Figure 33**C-D**). In particular, with both the adaxial and abaxial leaves contain intertwined needle crystalline features that are consistent throughout the leaf tissue (Figure 33**C**). Along with crystalline similarity, there were few cellular structures in the form of stomata and other epidermal cells present during leaf maturation (Figure 33**E**). This homogeneity helps solidify contact with the ATR crystal, most likely leading to similarities in spectra being observed.

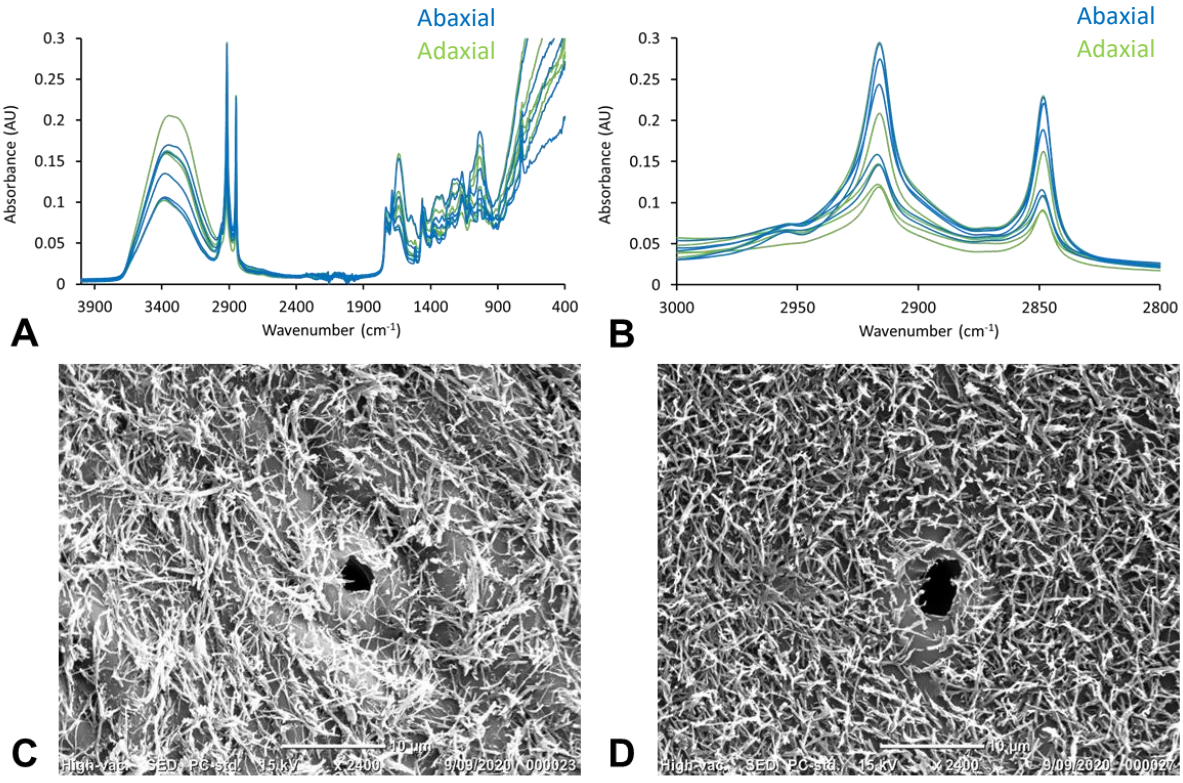

Figure 33: *ATR-FTIR individual spectra of **immature** eucalyptus Tuart (5 adaxial (green), 5 abaxial (blue)) in overall (400-4000 cm^{-1}) and lipid ν(C-H) (2800-3000 cm^{-1}) stretching regions, demonstrating disparity in wax (lipid) content between adaxial and abaxial surfaces **A, B**. SEM images of eucalyptus Tuart immature leaves adaxial (**C**) and abaxial (**D**) displaying distribution of epicuticular wax crystallinity scale = 10 µm.*

3.2.3 Investigation of Spectroscopic Differences in ATR-FTIR Spectra Collected from the Surface of Tuart Leaves at Different Stages of Leaf Maturation (Immature vs Mature)

Substantial spectroscopic differences were observed between ATR-FTIR spectra collected from the adaxial surface of immature and mature tuart leaves (Figure 31 **(3.2.1)**). Specifically, greater intensity was observed across all absorbance bands attributed to epicuticular waxes [ν(C-H) 2800 – 3000 cm^{-1}, ester carbonyl ν(C=O) 1700 – 1770 cm^{-1}) and δ(C-H) 1400 – 1480 cm^{-1}], for spectra collected from young leaves relative to mature leaves (Figure 34**A,B**). As was the case with comparisons of adaxial vs abaxial leaf surfaces, the spectroscopic changes could be due to differences in wax content on the surface, or surface morphology. To investigate surface morphology, SEM images were collected from the adaxial surface of young and mature tuart leaves. Not unexpectedly the results highlight a relative homogeneous distribution of needle like wax crystals on the surface of young leaves, with large "column like" features observed in mature leaves. Thus, due to the differences in surface morphology, it is difficult to ascribe the increased spectral intensity observed in young leaves to either increased wax content or a different surface morphology (and therefore, better contact with the ATR crystal).

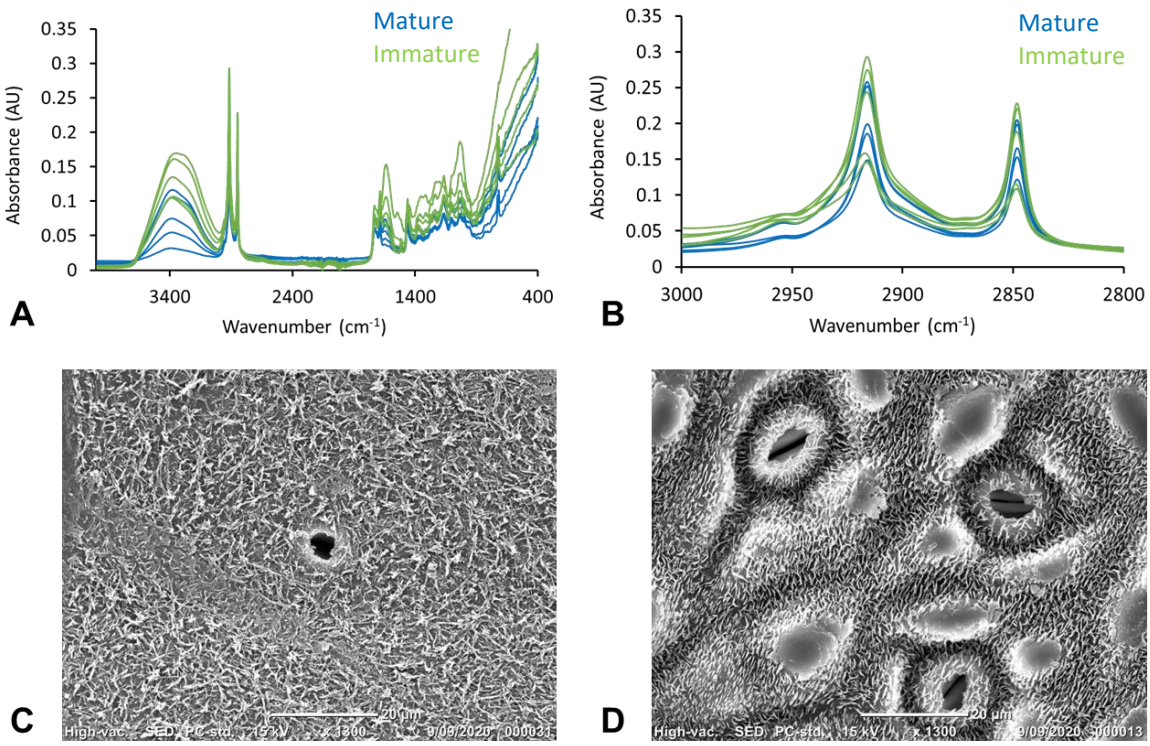

Figure 34: *ATR-FTIR individual spectra of immature (green) and mature adaxial (blue) eucalyptus tuart leaves in overall (400 – 4000 cm^{-1}) and lipid ν(C-H) (2800 – 3000 cm^{-1}) stretching regions, demonstrating disparity in wax (lipid) content between species **A, B**. SEM images of eucalyptus tuart adaxial leaves immature (**C**) and mature (**D**) showing distribution differences of epicuticular wax layers (webbed vs flaky structure) and crystallinity. Scale = 20 µm.*

3.3 Application of ATR-FTIR coupled to a Synchrotron Lightsource, to Reveal Sub-cellular Epicuticular Wax Distribution on Leaf Surfaces

The previous sub-sections (3.1, 3.2) have established that ATR-FTIR spectroscopic analysis of the epicuticular wax layer on leaf surfaces can differentiate between different eucalyptus species, leaf surfaces (abaxial vs adaxial) and leaf development (young vs mature). The differentiating capability appears to result from differences in wax content but also differences in the leaf surface morphology (with difficulty to differentiate between the two). The results of the previous sections were obtained with bulk spectroscopic analysis, and as such, do not shed light on wax changes that might be occurring at the cellular or sub-cellular spatial scale across the leaf surface.

Understanding the capability of FTIR spectroscopy to study spatially resolved changes in epicuticular waxes is important for several reasons. Firstly, in future applications of developed methods (e.g., Chapter 4.2.4 - 4.2.6) it might be important to associate changes to wax content associated with specific parts of the leaf (e.g. anatomical features). Secondly, it might be important to associate changes in wax content with disease progress (e.g. Chapter 4.2.8 – 4.2.10). Therefore, the capability of FTIR spectroscopy for spatially resolved investigations of epicuticular waxes was deemed important for future method developments.

To investigate the epicuticular wax layer at higher spatial resolution, a synchrotron light source was used. Due to the high brightness of synchrotron light, there is sufficient photon flux to provide adequate spectral signal to noise ratio when using small aperture sizes selected to achieve diffraction limited spatial resolution. Further, due to the use of high refractive index ATR crystals, the diffraction limited spatial resolution is improved relative to traditional transmission FTIR microscopy (as described in Chapter 1.2.4).

Due to the difficulty of transporting flora across Australian state borders (quarantine and biosecurity regulations), synchrotron radiation ATR-FTIR spectroscopic method development took advantage of Eucaltyptus trees growing onsite at the Australian synchrotron. Specifically, investigation into the epicuticular wax formation and distribution in *Eucalyptus leucoxylon* ("yellow gum") was undertaken.

Due to the small size of the Ge micro-ATR crystal, care needed to be taken when making contact between the leaf and micro-ATR-crystal tip, so as not to damage the wax layer or rupture the leaf cells. The sudden appearance of strong ν(OH) absorbance bands in the ATR-FTIR spectrum was used as an indicator of water contact on the crystal, a marker of cell rupture, and if this occurred, a new region of the leaf was chosen for analysis. The regions of interest analysed with micro-ATR-FTIR were selected from the bright field optical image, which enabled regions of interest to be defined around specific cells. Two representative examples of micro-ATR-FTIR spectroscopic mapping are presented in Figure 35 and Figure 36. In each case,

distribution of water [ν(OH) 3000 – 3500 cm^{-1}], wax [$\nu_s(CH_2)$ 2845 – 2865 cm^{-1}] and proteins [$\nu_s(CH_3)$ 2865 – 2885 cm^{-1} and amide I 1600 – 1700 cm^{-1}] can be observed. These biochemical distribtions provide straight forward visualisaiton of cells on the leaf surface (cell location indicated by higher water and protein content), with greater wax content surrounding the cell.

Within the cell of Figure 35, several distinct protein enriched regions are observed, one circular (diamater ~ 10 µm), the other eleptical (length ~5 µm). The size, shape and location of these features are consistent with the nucleus and chloroplast respectively. Not unexpectedly the water content is inverseley correlated with protein content within the cell (e.g. where there is high protein there is less water, and vice versa), which in consistent with the existence of cell nucleus and chloroplasts surrounding by the cytosol.

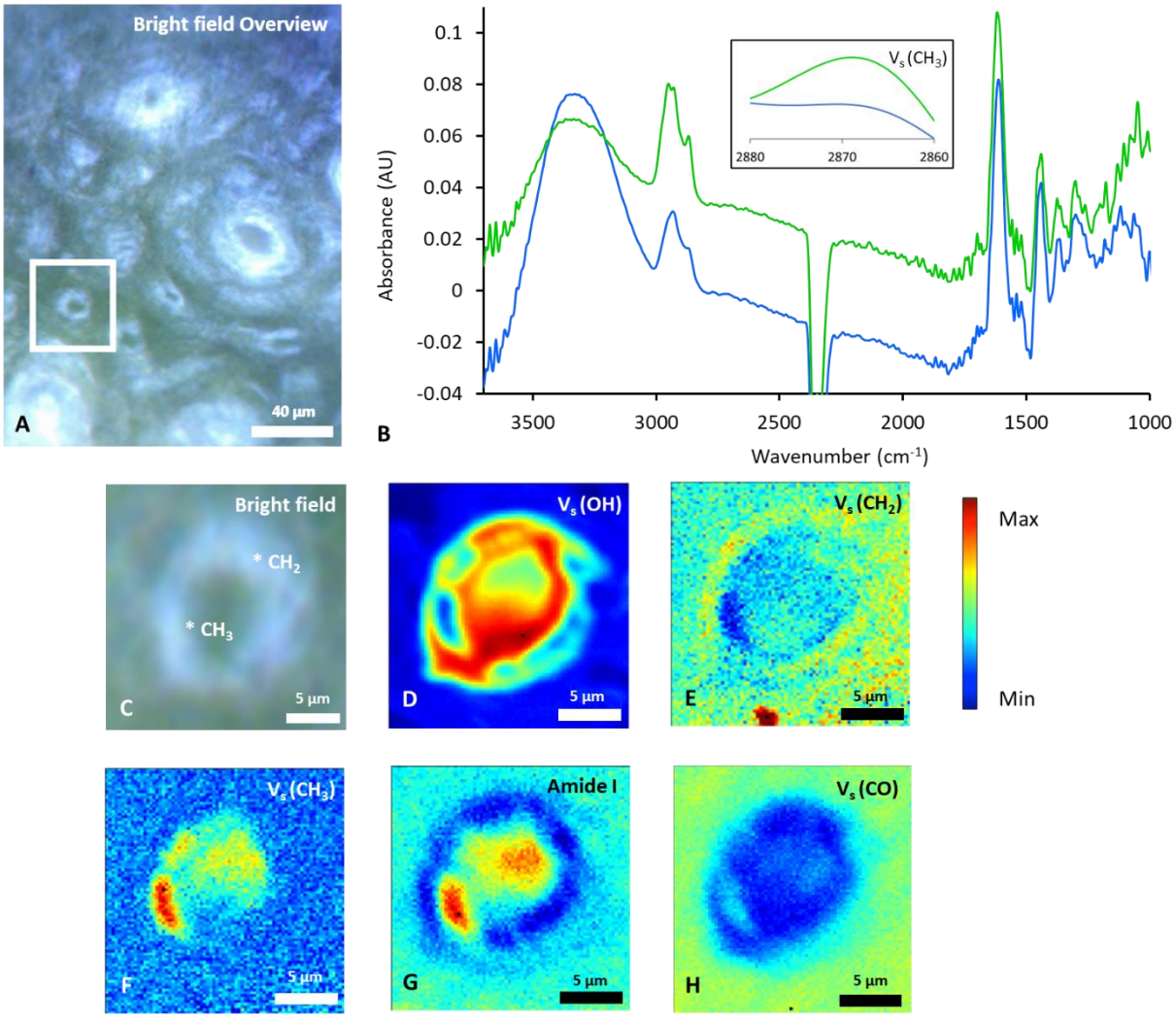

Figure 35: *Synchrotron macro ATR-FTIR showing sub-micron mapping of epicuticular wax distribution of an unknown cell in eucalyptus leaf section brightfield overview, Asterix of CH_2 and CH_3 regions taken for representative spectra (A, C). Representative synchrotron macro ATR-FTIR spectra showing differences seen throughout protein, [(amide I 1600 – 1700 cm^{-1}) and ($\nu_s(CH_3)$ 2865 – 2885 cm^{-1})], lipid, ($\nu_s(CH_2)$ 2845 – 2865 cm^{-1}), alcohol, (ν(OH) 3000 – 3500 cm^{-1}) and ν_s(C=O) 1670 – 1820 cm^{-1}), groups, (green spectra $\nu_s(CH_3)$ imaging region, blue spectra $\nu_s(CH_2)$ imaging region indicated in C.) (B). false-colour images of representative functional groups (D-H).*

The representative macro-ATR-FTIR image shown in Figure 36 was collected from the location of a stomata. Stomata are a type of cell structures located on the epidermis of leaf tissue that controls the rate of gas exchange between CO_2 influx and H_2O and O_2 efflux, aiding in photosynthesis and maintaining hydration. Key differences when looking at the chemical makeup of stomata cells structures, is that there is a lack of methylene groups present within the guard cells that make up the stomata (Figure 36**E**), this is to be expected as chemical signalling of guard cells (influx and efflux) occurs predominately from inorganic potassium and chloride ions. While the adjacent lipid epicuticular wax deposits seen are rich in methylene (Figure 36**E**). A methyl signal could still be seen within the guard cells which agrees with strong expression of the pectin methylesterase gene in guard cells and essential for stomatal function (Figure 36**F**). (146, 147). The composite images of methylene and methyl displayed in Figure 36**E,F** show that a heterogeneous wax distribution based on the intensity of the methylene groups is observed, with the greatest wax content found between cell walls (rich in methyl groups) with chemical intensities shown in Figure 36**B**.

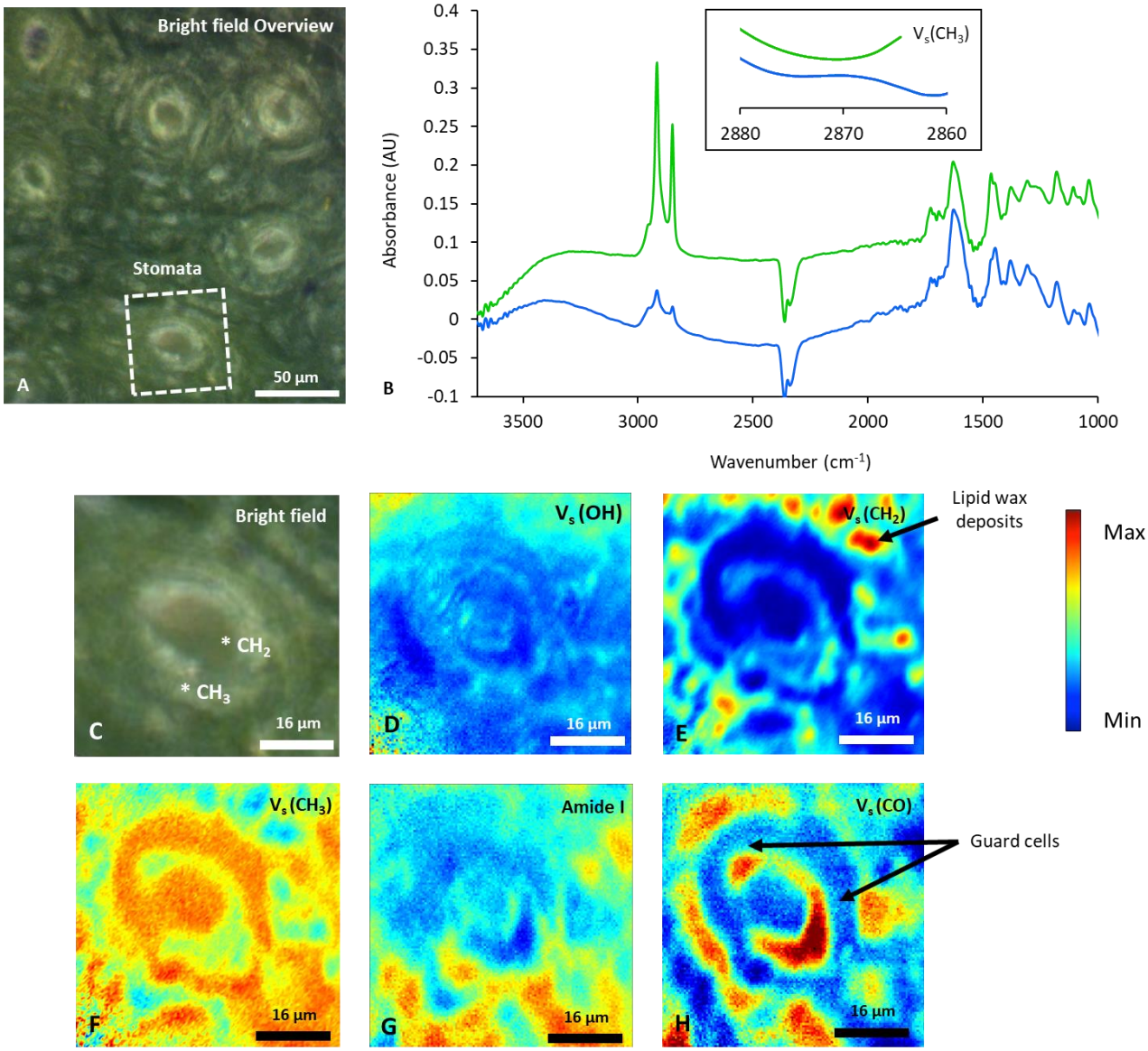

Figure 36: *Synchrotron macro ATR-FTIR showing sub-micron mapping of epicuticular wax distribution of an Stomata cell eucalyptus leaves brightfield overview (A, C). Representative synchrotron macro ATR-FTIR spectra showing differences seen throughout protein, [(amide I 1600 – 1700 cm^{-1}) and (ν_s(CH$_3$) 2865 – 2885 cm^{-1})], lipid, (ν_s(CH$_2$) 2845 – 2865 cm^{-1}), alcohol, (ν(OH) 3000 – 3500 cm^{-1}) and carbonyl, (ν(C=O) 1670 – 1820 cm^{-1}), groups, (green spectra ν_s(CH$_3$) imaging region, blue spectra ν_s(CH$_2$) imaging region indicated in C.) (B). false-colour images of representative functional groups (D-H).*

This data highlights that synchrotron macro ATR-FTIR mapping microspectroscopy has the potential to fill the gap between bulk analysis of epicuticular wax composition and EM imaging at nanoscale spatial resolution. Being able to distinguish chemical compositional changes at higher resolution on plant tissue surfaces using synchrotron ATR-FTIR opens up possibilities of using infrared reflectance techniques to identify biomarkers of plant health.

3.4 Using Ether Extractions to Reveal Individual Waxes Present on the Surface of Epicuticular Waxes in Eucalyptus Leaves

While ATR-FTIR has demonstrated potential to study epicuticular waxes, the chemical specificity of FTIR is still relatively limited compared to other techniques. An investigation into the separation and purification of different wax molecules was therefore attempted. From the five fractions present after column extractions as detailed in Chapter 2.5 fraction one was analysed as it had the greatest amount of crude mass volume. The crude ^{1}H NMR indicated the potential presence of ursolic acid which is a molecule found in the waxy surface of eucalyptus leaves and commonly found in eucalyptus oils (Appendix - ^{1}H NMR Spectrum (400 MH_z, DMSO)
Crude - Fraction 1: Marri Extraction). Typical ^{1}H NMR peaks for ursolic acid include ^{1}H NMR ($CDCl_3$) = δ 0.88 to δ 0.9 (m, methyl protons), δ 1.29 to δ 1.93 (m, 25H, CH2 and CH protons), δ-1.3, 2H (cyclohexane), δ-2.0, 1H (OH from alcohol), δ-4.52 (olefinic protons), δ-11.0 (1H (OH from carboxylic acid). (148-150) After further purification via 10% ethyl acetate and petroleum spirits (40-60 ºC) followed by a 50/50% EtoAc/Pet spirits separation the ^{1}H NMR was found to hold impurities as multiple peaks not associated to ursolic acid were still present (Appendix - ^{1}H NMR Spectrum (400 MH_z,$CDCl_3$) “Purified” - Fraction 1: Marri Extraction). Possibilities as to what these impurities are include molecules similar to ursolic acid that are present within the epicuticular wax layer, this could include triterpenes such as oleanolic acid, and ursolic acid lactone, two major constituents of epicuticular waxes alongside ursolic acid. When groups of molecules of the same relative size and polarity are present isolation and identification of waxes can prove to be difficult while looking at ^{1}H NMR of large molecular sizes, proving hydrogen peak identification to be strenuous. ATR-FTIR shows a few characteristic peaks, indicating chemical signals

of waxes, however, we do not know whether this is due to their only being one or two types of waxes present on the epicuticular surface, or an average of many different types, ^{1}H NMR helps to prove the latter, as having complex ^{1}H NMR with multiple H-peaks helps identify the presence of different waxes, as well as determining wax concentration differences on the surface of eucalyptus leaves. Due to time restraints research priority was focused on furthering investigations into reflectance techniques, and therefore further purification and investigation into individual molecules present in epicuticular waxes is needed.

3.5 Conclusions

Benchtop ATR is a well-known spectroscopic technique with capability to detect subtle changes of epicuticular waxes in leaves. This study has demonstrated this capability as proof-of-concept using immature and mature as well as adaxial and abaxial leaf tissue. This now opens opportunities for case studies involving plant health to be investigated. The use of chemometrics during benchtop ATR studies helped differentiate and better represent changes between eucalyptus species in what would otherwise look like a complex set of spectra. When looking at differences, PC-1 components contained >80% of spectral variation which came from the lipid 2800-3000 cm^{-1} C-H stretching region helping confirm that the spectral signal was arising from long chain waxes.

The capability to study epicuticular wax distribution using Synchrotron ATR-FTIR microspectroscopy at high spatial resolution, and the ability to correlate wax constituent with plant anatomical structures, such as the cell wall and stoma cells, has reinforced the possibility to monitor plant health through *ex vivo* spectroscopic methods. As this chapter as demonstrated the ability to study components of plant physiology based on FTIR spectra obtained from leaf surface, however it also revealed that ATR-FTIR is not compatible with *in vivo* longitudinal monitoring. Therefore, chapter 4 will aim to extend method development, using reflectance-FTIR as a non-destructive method to monitor plant epicuticular waxes *ex vivo* and *in vivo*.

CHAPTER 4

Development and Application of Fourier Transformed Infrared Reflectance Microspectroscopy to Investigate Epicuticular Wax Distribution on Leaf Surfaces

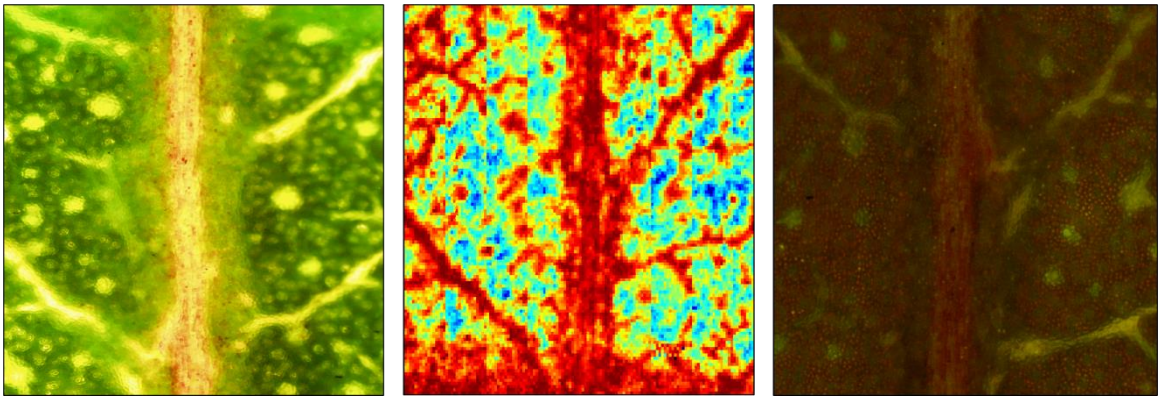

Components of the following chapter has data previously published in Advanced Science: Karina Khambatta, Ashley Hollings, Georgina Sauzier, Lilian M. V. P. Sanglard, Annaleise R. Klein, Mark J. Tobin, Jitraporn Vongsvivut, Mark R. Gibberd, Alan D. Payne, Fatima Naim, and Mark J. Hackett ***"Wax On, Wax Off": In Vivo Imaging of Plant Physiology and Disease with Fourier Transform Infrared Reflectance Microspectroscopy***. Advanced Science **2021** *8* (19), 2101902
DOI: 10.1002/advs.202101902

4.1 Introduction

Analysis of the epicuticular wax layer on the surface of plant leaves can provide a unique window into plant physiology and responses to environmental stimuli. Well-established analytical methodologies can quantify epicuticular wax composition, yet few methods are capable of imaging wax distribution *in situ* or *in vivo*. This chapter reports the first use of Fourier transformed infrared (FTIR) reflectance spectroscopic imaging as a non-destructive and *in situ* method to investigate variation in epicuticular wax distribution at 25 μm spatial resolution. Case studies demonstrate *in vivo* imaging of alterations in epicuticular waxes during leaf development and *in situ* imaging during plant disease or exposure to environmental stressors. It is envisaged that this new analytical capability will enable future *in vivo* studies of plants to provide insights into how the physiology of plants and crops respond to environmental stresses such as disease, soil contamination, drought, soil acidity, and climate change.

Wax synthesis is intrinsically linked to metabolism within the plant, hence unique differences in metabolism manifest in species-specific epicuticular wax composition on the leaf surface. (4, 151, 152) The composition of epicuticular waxes are influenced by seasonal variation, leaf age, and plant health. (11, 151, 153) Therefore, these alterations in wax composition and distribution may serve as a marker of plant health and response to environmental stimuli.

Although there is substantial published literature using chemical extraction followed by chemical identification methods to study epicuticular waxes, such methods remove important spatially resolved information. Further, chemical extraction methods are not compatible with *in vivo* analysis. FTIR and Raman spectroscopic techniques possess a distinct advantage allowing for direct and *in situ* measurement with minimal sample preparation, negating the need for solvent extraction of waxes from the leaf surface. Whilst FTIR and Raman microspectroscopy are often performed on thin sections, the ATR-FTIR technique can be used to analyse the surface of the sample regardless of its thickness. (154) However, as demonstrated in Chapter 3 the process of making physical contact between the ATR crystal and leaf surface can damage the leaf tissue, and it is therefore not suitable with *in vivo* longitudinal time course studies.

Here, we report the use of FTIR microscopy and a linear array imaging detector configured in reflectance geometry to image epicuticular waxes at 25 μm spatial resolution across large areas of the leaf surface within a reasonable time frame (1–2 h). Collection of spectra in a reflectance geometry is advantageous as it does not require physical contact to be made between the leaf surface and external accessory (e.g., ATR crystal), and is therefore truly non-destructive. This capability has enabled differentiation between major leaf anatomical structures (including stomata, veins, and stem), and has identified differences in epicuticular wax composition between young and mature leaves, and across seasons.

This chapter also demonstrates the use of FTIR reflectance microscopy to monitor changes of epicuticular wax in Geraldton wax needles, while under the effects of ethylene gas. Ethylene is a major plant hormone that causes acceleration in plant growth and senescence, it is commonly used in the agricultural sectors to hasten plant maturation and fruit ripening. (155, 156) The increase in plant growth and senescence has been observed to have direct impact on the epicuticular wax distribution, which was reflected in FTIR reflectance spectra.

Last, this chapter demonstrates the capability of this method to monitor changes of epicuticular waxes on wheat leaves infected with a necrotrophic fungal pathogen, *Pyrenophora tritici-repentis* (Ptr). The pathogen causes yellow spot disease, which has devastating impact on crop yields. (23, 133) The plant–pathogen interactions induce detectable spectroscopic alterations to the wax layer, highlighting the capability of FTIR reflectance microscopy as a future tool to study the pathology of this disease.

4.2 Results and Discussion

4.2.1 Demonstrating the Experimental Limitations Associated with Imaging Leaf Tissue Sections with Fourier Transform Infrared Transmission Spectroscopy and Raman Microscopy

Initially, FTIR transmission imaging and Raman microscopy was undertaken in order to analyse plant tissue cells adjacent to the epicuticular wax layer. The process of sectioning enables imaging of interior leaf tissue structures that are not visible from the outer surface, such as lignin rich cell walls. (157-162) Sectioning unfortunately, can damage the exterior surface of the leaf sample and does not adequately preserve epicuticular wax distribution (Figure 37). The false colour images seen in Figure 37**B,D** during FTIR transmission imaging, and 37**I** during Raman microscopy shows a discontinuous epicuticular wax layer, indicative of sample-preparation induced damage resulting in reduced spectral signals from the $\nu_s(CH_2)$ lipid regions as seen in Figure 37**E,J**. These results highlight the benefit of non-destructive *in situ ex vivo* or *in situ in vivo* imaging capabilities for the analysis of epicuticular waxes.

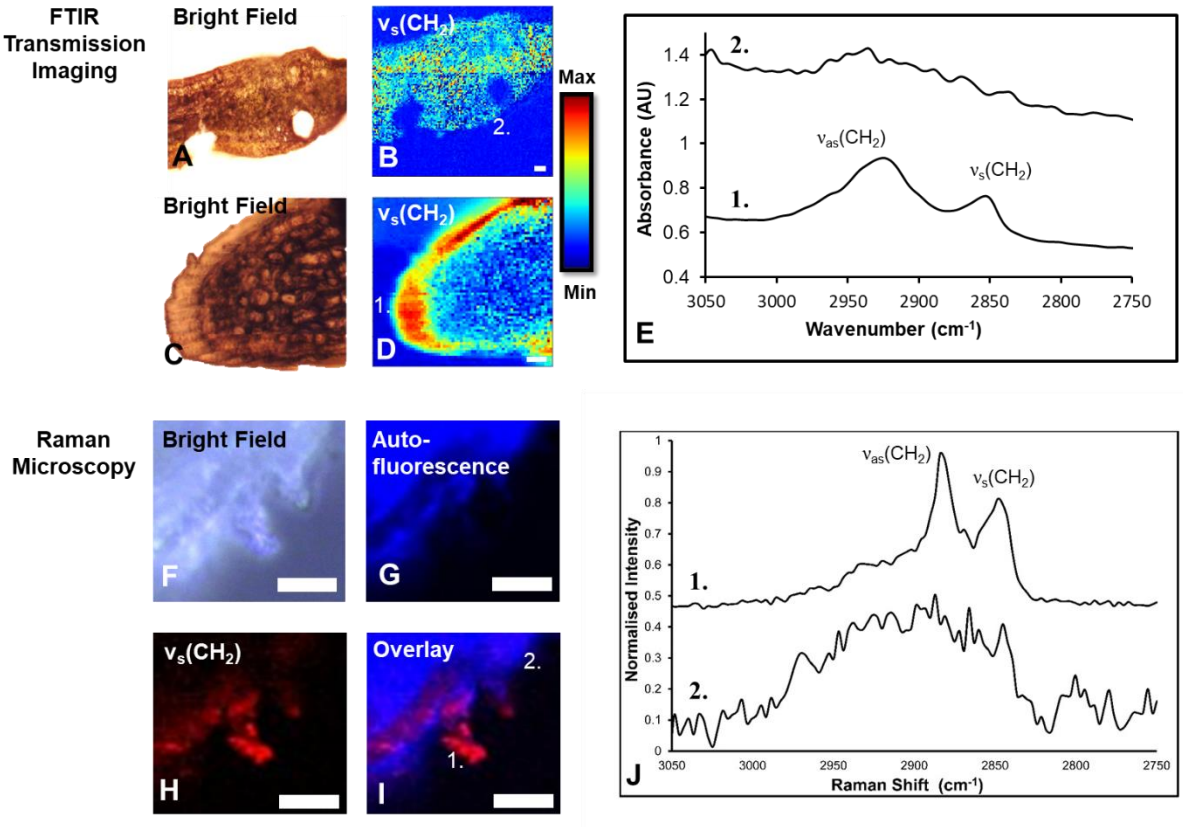

Figure 37: *The epicuticular wax layer is not consistently preserved in leaf sections, as observed through FTIR spectroscopic imaging (A-E), and Raman microscopy*

analysis (F-J). Bright field images reveal sample morphology (A, C). FTIR spectroscopic imaging revealed that the wax layer was absent in some sections (B), but present in other sections (D). False-colour functional group images in (B) and (D) were generated from integrated area under the curve for the $\nu_s(CH_2)$ absorbance band (2840 – 2865 cm^{-1}). Representative FTIR spectra from image positions 1 (good wax preservation) and 2 (poor wax preservation) are shown in (E). Raman microscopy analysis of leaf sections (F-I) yielded similar conclusions. The bright field image (F), and the autofluorescence Raman image reveals leaf structure (G), and the false-colour functional group images generated from integrated area under the curve for the $\nu_s(CH_2)$ absorbance band 2840 – 2865 cm^{-1} reveals location of epicuticular waxes (H). Overlay of the autofluorescence and epicuticular wax image reveals inconsistent preservation of epiculatular wax on the leaf surface (I). Representative Raman spectra from image positions 1 (good wax preservation) and 2 (poor wax preservation) are shown in J. Scale bar B-D, F-I = 5 µm.

4.2.2 Development of a Non-destructive Imaging Method to Study Leaf Surfaces, using Fourier Transform Infrared Reflectance Microscopy

Collection of FTIR spectra in a reflection geometry is advantageous, as it inherently doesn't require contact of optical components with the leaf (as is the case for ATR-FTIR), and it doesn't require sectioning of the leaf tissue (as is the case for transmission-FTIR). Therefore, this thesis investigated FTIR reflectance as a potential technique compatible with non-destructive *in situ* (*ex vivo* or *in vivo*) analysis of leaf surfaces. An example of an FTIR reflectance spectrum is shown in Figure 38. Importantly, the FTIR reflectance spectra collected from the surface of a plant leaf demonstrate sufficiently strong infrared reflectance signal across the ν(C-H) region (2800–3000 cm^{-1}, corresponding to light wavelengths of ≈3.3–3.6 µm). The detection of this signal enables characterization of epicuticular waxes. The spectroscopic features show intense $\nu_{as}(CH_2)$ and $\nu_s(CH_2)$ spectral features, but minimal contribution from $\nu_{as}(CH_3)$ and $\nu_s(CH_3)$ absorbance bands, which support long chain aliphatic wax as the main source of the reflectance signal (Figure 38**C-E**). The strong negative peaks in the spectra for $\nu_{as}(CH_2)$ and $\nu_s(CH_2)$ vibrational modes support the proposition that the signal is originating from a thin-film effect, consistent with infrared reflection absorption spectroscopy (IRRAS) (Figure 38**D**). (52, 54, 55) The strong negative

signal results from increased reflectivity of light at these wavelengths, which indicates the presence of a thin molecular film, thinner than the wavelength of incident light, (50, 53) which is possible given that the epicuticular wax layer is typically 50–200 nm thick. (163) Therefore, owing to the strong IRRAS signal produced by the thin epicuticular wax layer on leaves, we demonstrate that FTIR reflectance microspectroscopy is sensitive to, and capable of imaging the epicuticular wax coating on leaf surfaces.

Despite the ability of ATR-FTIR to directly map epicuticular waxes on leaf surfaces (previously described in chapter 3), the requirement for physical contact between the ATR crystal and leaf surface prevents longitudinal time-course studies of the identical leaf region in living plants. FTIR reflectance microspectroscopy was therefore investigated as an alternative modality that may provide direct *in situ* analysis of epicuticular waxes compatible with longitudinal studies of plant development or disease progression. Similar to the synchrotron ATR-FTIR (SR-ATR-FTIR) spectra, FTIR reflectance spectra revealed the characteristic spectroscopic markers of waxes (i.e., intense $\nu_s(CH_2)$ and $\nu_{as}(CH_2)$ absorbance bands at 2848 and 2930 cm^{-1}, respectively) with minimal evidence of $\nu_s(CH_3)$ and $\nu_{as}(CH_3)$ absorbance bands (Figure 38**D,E**). In particular, the $\nu_s(CH_2)$ and $\nu_{as}(CH_2)$ bands were found to display a strong negative signal in the FTIR reflectance spectrum (Figure 38**D**), or strong positive peaks in the second derivative spectra (Figure 38**F**), which is characteristic of IRRAS effect. This effect arises from increased specular reflectance for wavelengths of light at which an absorption band occurs, relative to wavelengths that do not correspond to a resonant absorbance. (54) The intensity of the reflectance signal was found to vary across the leaf surface (Figure 38**G**) where wax crystals localize (revealed by SEM, Figure 38**H**), and thus provides a spectroscopic marker to image epicuticular wax in relation to leaf anatomy (Figure 38**I–K**). As can be seen in Figure 38**I– K**, FTIR reflectance imaging of the $\nu_s(CH_2)$ absorbance band revealed the location of key anatomical features of the leaf surface (stem, veins, and stomata tissue).

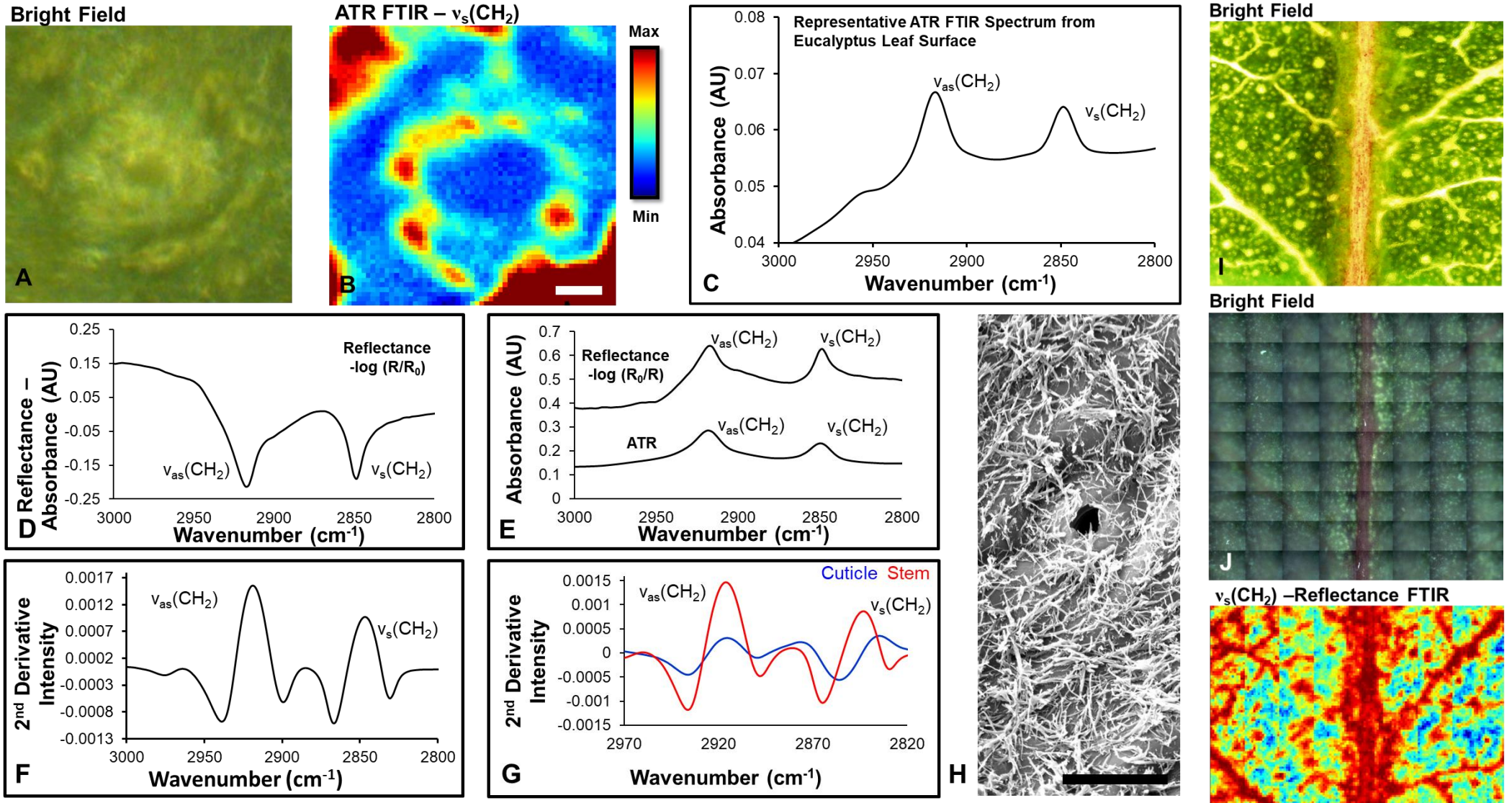

Figure 38: *Epicuticular waxes on the leaf surface can be measured in situ by SR-ATR-FTIR spectroscopy (direct contact, destructive method) or by FTIR reflectance spectroscopy (non-contact, non-destructive). A) Bright field image of stomata*

on the surface of a Eucalyptus leaf, which was then analyzed by SR-ATR-FTIR spectroscopy. B) False-color functional group images generated from integrated area under the curve for the $\nu_s(CH_2)$ absorbance band (2840–2865 cm^{-1}) in SR-ATR-FTIR spectra showing location of wax rich regions. Scale bar = 5 μm. C) Representative SR-ATR FTIR spectra of epicuticular wax. D) Representative FTIR reflectance spectra from the surface of the Eucalyptus leaf, and E) comparison of FTIR reflectance spectra with SR-ATR FTIR spectra. F) Representative FTIR reflectance second derivative spectra. G) Different anatomical locations on the leaf surface produce different FTIR reflectance spectral signatures, which can be observed in the second-derivative spectra. Spectra in (F) and (G) were not vector normalized prior to calculation of second-derivatives. H) Representative SEM image captured from the surface of the leaf, showing thin wax structures that contribute to the infrared reflectance properties of the leaf surface. Scale bar = 10 μm. I,J) Bright field optical microscope (white light illumination) image of plant leaf surface, showing the sample region that was then imaged with FTIR reflectance (10× magnification). These bright field images of the leaf imaged with FTIR reflectance were collected on a dedicated optical microscope (I) and the optical microscope coupled to the FTIR spectrometer (J). K) False-color FTIR reflectance functional group images of wax layer generated from second-derivative intensity of the $\nu_s(CH_2)$ absorbance band at 2848 cm^{-1}. Scale bar = 500 μm.

4.2.3 Investigating Different Metal Substrates as Background References for the Analysis of Leaf Surfaces with Fourier Transform Infrared Reflectance Microscopy

Different metal substrates, such as gold and aluminium foil were tested as background references. Background reflectance images were collected from the surface of aluminium foil and gold under the same conditions and using the same parameters (Figure 39**A**). Strong FTIR reflectance spectra were confirmed to occur using either aluminium foil or a reflective gold surface for background reflection. To further demonstrate that the reflectance signals observed from the leaf surface arise form epicuticular waxes, a series of leaf samples were analysed with and without wax removal (incubation in ether). The FTIR reflectance signal was observed to drastically decrease in the leaf samples following incubation in ether, helping confirm specificity of the reflectance signal to the epicuticular wax layer (Figure 39**B**).

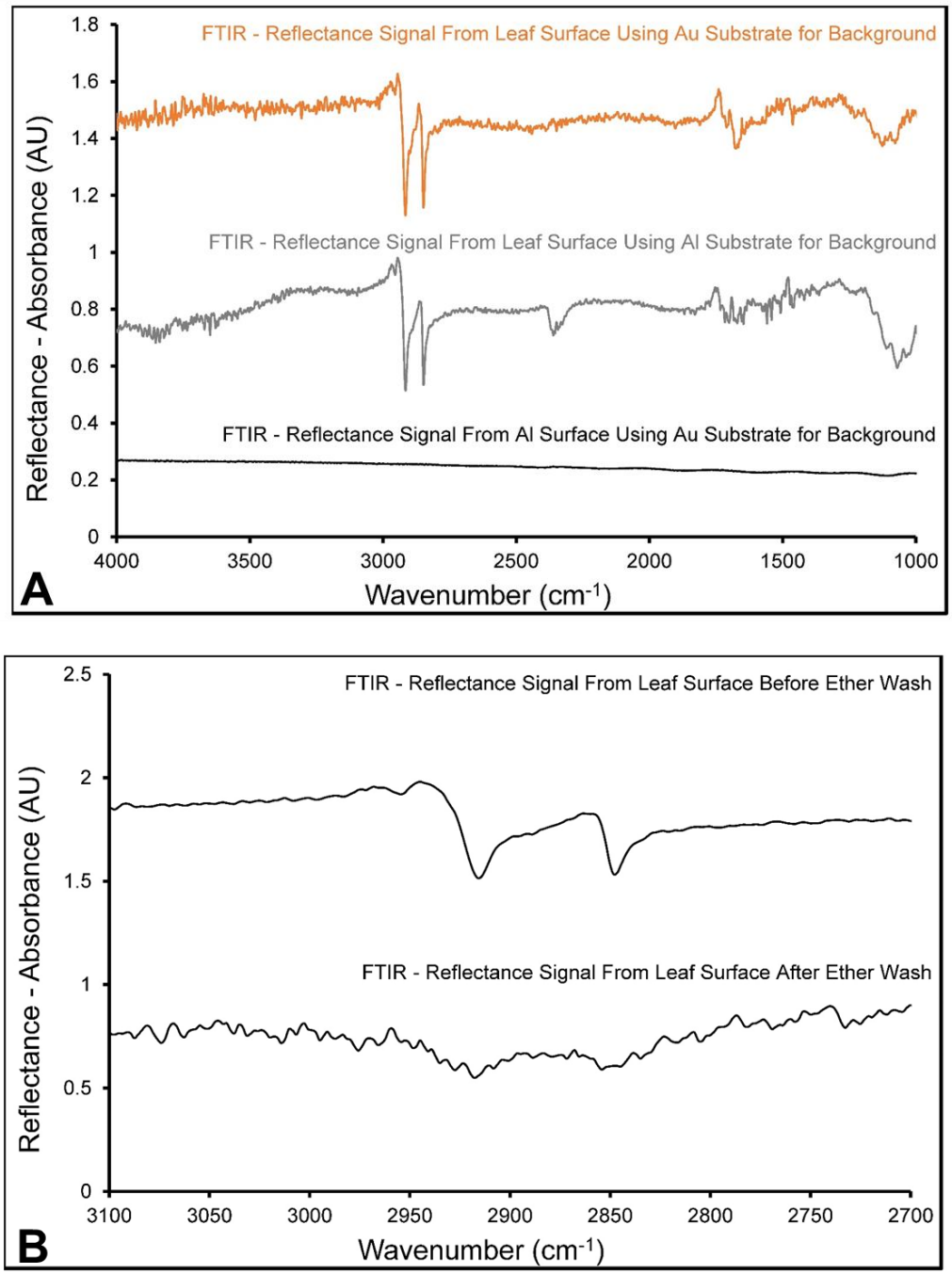

Figure 39: *FTIR reflectance signal of the epicuticular wax layer on plant leaf surface is observed independent of background substrate used (Au vs Al) (A). Incubation of leaves in ether ("Ether Wash") extracts waxes from the leaf surface and drastically reduces the FTIR reflectance signal (B).*

4.2.4 Studying Seasonal Variations in Fourier Transform Infrared Reflectance Spectra of Leaf Surfaces

It is well-established that the epicuticular wax coatings change as a consequence of seasonal variation. (11, 151, 153) The FTIR reflectance signal observed in Figure 40 demonstrates reproducible seasonal variation. Images of leaves collected and analysed during winter revealed a stronger reflectance signal of the $\nu_s(CH_2)$ mode relative to leaves collected in autumn (Figure 40**A–D**). Analysis of the intensity of the $\nu_s(CH_2)$ reflectance signals (measured as second derivative intensity at 2848 cm^{-1}), using five replicate leaves collected in autumn and winter, revealed a statistically significant effect of season on reflectance intensity ($p < 0.05$). Post-hoc testing (Figure 40**E**) indicated that the reflectance intensity was significantly stronger in leaf tissue regions (stem, vein, cuticle, and cuticle adjacent to stem) in winter relative to those in the autumn ($p = 0.03$, $p = 0.0006$, $p = 0.0005$, and $p = 0.002$, respectively). In addition to the increased reflectance intensity observed for leaves analysed in winter relative to summer, an associated shift in the band positions was also observed. In particular, a shift to higher wavenumbers of (CH) modes occurred in spectra collected from leaves in winter relative to those in autumn (Figure 40**C**). Two-way ANOVA revealed that the effect was statistically significant ($p < 0.0001$). Post-hoc testing (Figure X**F**) indicated that the shifts in band position appeared to be significantly different between the samples in autumn and winter across the stem, vein, cuticle, and cuticle adjacent to stem tissue regions ($p = 0.04$, $p = 0.00004$, $p = 0.0001$, and $p = 0.0005$, respectively).

In summary, these experiments have demonstrated that the resulting FTIR reflectance signal from the leaf surface significantly changes in response to seasonal variation. It is rationalised that the epicuticular wax layer becomes thinner in winter, as there is less risk of plant dehydration, and that the decreased wax thickness enhances reflectance intensity.

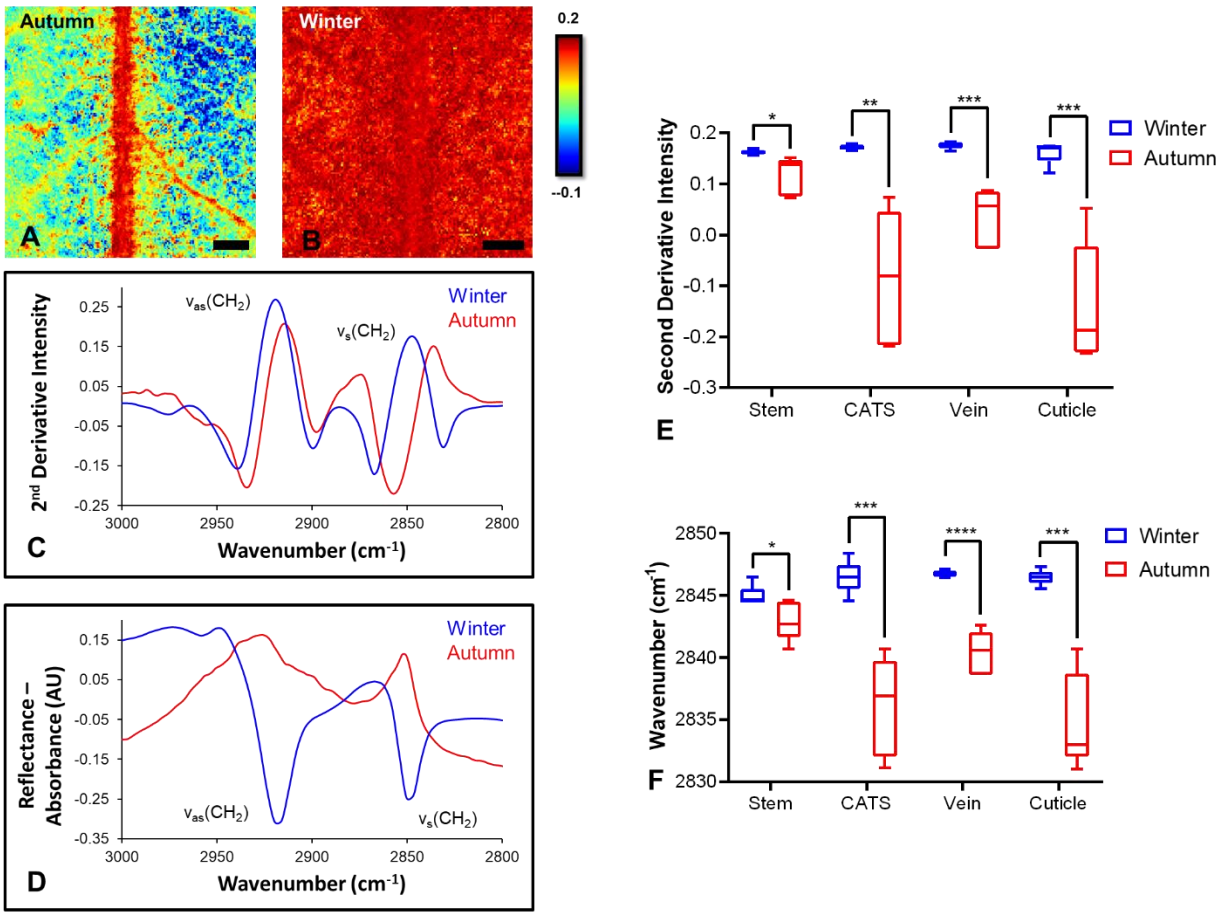

Figure 40: *FTIR reflectance spectroscopic imaging reveals consistent spectroscopic differences associated with seasonal variation, comparing leaves analyzed in autumn against leaves analyzed in winter. A,B) False-color functional group images of wax layer, generated from second-derivative intensity of the $\nu_s(CH_2)$ absorbance band at 2848 cm^{-1}, showing location of wax rich regions in leaves in autumn (A) and leaves in winter (B). Representative second-derivative spectra (C) and non-derivatized spectra (D) reveal the decreased reflectivity in spectra from leaves in autumn compared to winter, and show the shift of $\nu_s(CH_2)$ to lower wavenumbers in autumn compared to winter. E,F) Statistical analysis of replicates reveals that the observed differences in intensity (E) and peak positions (F) are significant. Data in (E) and (F) are presented as a box and whisker plots showing the mean, upper, and lower quartiles. Error bars show the standard deviation. All statistical testing was undertaken using a two-way ANOVA, followed by post-hoc testing, as described in the Experimental Section. Each experimental group consists of five replicates (n = 5). Post-hoc testing was performed with t-tests, corrected for four multiple comparisons*

*using the Bonferroni method and an alpha of 0.05 (two-tail testing). *p < 0.05, **p < 0.01, ***p < 0.001, ****p < 0.0001. Scale bar = 500 μm.*

4.2.5 Observed Variation in *ex vivo* Fourier Transform Infrared Reflectance Spectra Collected from Leaf Surfaces During Leaf Growth and Maturation

It is well known that epicuticular wax coatings change as a result of leaf maturation, (11, 151) which was also observed in ATR-FTIR analyses reported in Chapter 3. To further investigate the sensitivity of FTIR reflectance microspectroscopy to changes in epicuticular wax layer of leaves, the reflectance signals obtained from the surface of immature and mature *Eucalyptus* leaves were compared (Figure 41**A,B**). Similar to the results observed with seasonal variation, changes in the intensity of the reflectance signal and position of the (CH) bands was observed during leaf growth and maturation. Specifically, increased reflectance intensity and shifts to higher wavenumbers were observed for $\nu(CH_2)$ absorbance bands on the surface of immature leaves relative to mature leaves (Figure 41**C,D**). Statistical testing confirmed that leaf growth had a significant effect on reflectance intensity ($p < 0.0001$) and peak position ($p < 0.0001$). The intensity of the $\nu_s(CH_2)$ band (measured at 2848 cm^{-1}) increased in immature leaves across the stem, veins, cuticle, and cuticle adjacent to stem relative to mature leaves ($p = 0.02$, $p = 0.0007$, $p = 0.0006$, and $p = 0.003$, respectively) (Figure XE). Likewise, the position of the $\nu_s(CH_2)$ band shifted to higher wavenumbers in the immature leaves relative to mature leaves (Figure 3F), which was observed in the spectra collected across the stem, veins, cuticle, and cuticle adjacent to stem ($p = 0.01$, $p = 0.001$, $p = 0.0007$, and $p = 0.0009$, respectively). SEM images revealed substantial differences in wax structure between immature and mature leaves, with thin fibril-like structures observed in immature leaves, and larger agglomerates observed in mature leaves (Figure 41**G**).

Young leaves that have reduced surface area and therefore reduced risk of water evaporation have been shown to have a thinner wax layer compared to mature leaves. (163) This could account for the stronger FTIR reflectance signals observed in younger leaves relative to more mature leaves, and further supported by SEM imaging in this study (Figure 41). Critically, an investigation into the ability to reproduce these

observations when measuring leaf maturation *in vivo*, in a longitudinal study of leaf development was undertaken (Chapter 4.2.6).

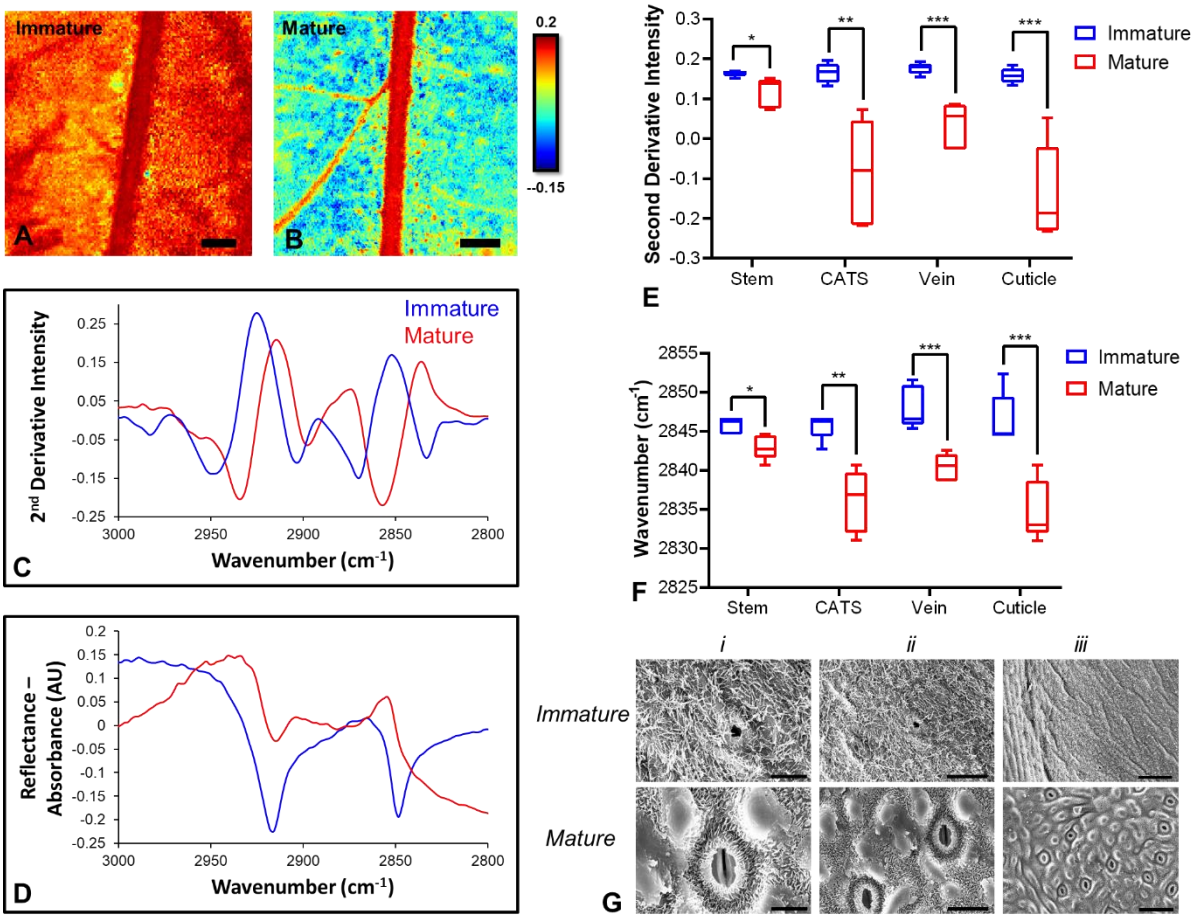

Figure 41: *FTIR reflectance spectroscopic imaging reveals consistent spectroscopic differences between young (immature) and old (mature) plant leaves. A,B) False-color functional group images of the wax layer, generated from second-derivative intensity of the $\nu_s(CH_2)$ absorbance band at 2848 cm^{-1}, showing location of wax rich regions in young (immature) leaves (A) and old (mature) leaves (B). Scale bar (A,B) = 500 µm. C) Representative second derivative and D) non-derivatized spectra reveal the decreased reflectivity in spectra from older (mature) leaves, and show the shift of $\nu_s(CH_2)$ to lower wavenumbers in older (mature) leaves, relative to younger (immature) leaves. E,F) Statistical analysis of five replicates from different morphological regions show that differences in peak intensity (E) and peak position (F) are significant for stem, the cuticle adjacent to the stem (CATS), veins, and cuticle, when comparing spectra from young (immature) and old (mature) leaves. Data in (E)*

*and (F) are presented as a box and whisker plots showing the mean, upper, and lower quartiles. Error bars show the standard deviation. All statistical testing was undertaken using a two-way ANOVA, followed by post-hoc testing, as described in the Experimental Section. Each experimental group consists of five replicates (n = 5). Post-hoc testing was performed with t-tests, corrected for four multiple comparisons using the Bonferroni method and an alpha of 0.05 (two-tail testing). *p < 0.05, **p < 0.01, ***p < 0.001. G) Representative SEM images of surface or immature and mature leaves, showing that the immature leaf surface contains thin, fibril-like wax structures, while large wax aggregates appear on the surface of mature leaves. Scale bar = 10 μm (i), 20 μm (ii), and 50 μm (iii).*

4.2.6 Observed Variation in Fourier Transform Infrared Reflectance Spectra Collected from Leaf Surfaces During Leaf Growth and Maturation *in vivo*

To demonstrate that FTIR reflectance microspectroscopy has capability to monitor changes to plant epicuticular waxes *in vivo*, and is therefore compatible with longitudinal studies, a series of experiments was undertaken to reproduce the leaf maturatuib results described above (Chapter 4.2.5), but in the same leaf imaged *in vivo*. To do this, five leaves were imaged in the exact same region 7 weeks apart (Figure 42**A-E**). The results from *in vivo* FTIR reflectance imaging (Figure 42**D–E**) were found to be consistent with the *ex vivo* measurements. Importantly, the decrease of reflectance signals and shifts of the characteristic $\nu_s(CH_2)$ band to lower wavenumbers was reproduced during maturation of leaves as measured *in vivo* (Figure 42**F**). The results were confirmed to be statistically significant using two-way ANOVA (p = 0.0006 and p < 0.0001 for signal intensity and band position, respectively). Post-hoc testing revealed that the intensity of the $\nu_s(CH_2)$ band (measured at 2848 cm^{-1}) increased in immature leaves across the veins and cuticle, relative to mature leaves (p = 0.02 and p = 0.002, respectively) (Figure 42**G**). Likewise, the position of the $\nu_s(CH_2)$ band shifted to higher wavenumbers in the immature leaves relative to mature leaves, in spectra collected across the vein and cuticle (p = 0.01 and p = 0.004, respectively) (Figure 4H). Differences between immature and mature leaves were not observed for the leaf stem or cuticle adjacent to stem.

This is the first time that *in vivo* time-course monitoring of changes in plant epicuticular waxes has been reported. Possibilities for future work includes live monitoring of crops benefitting the agricultural sectors when early signs associated to mechanisms involving changes in chemical composition can be observed.

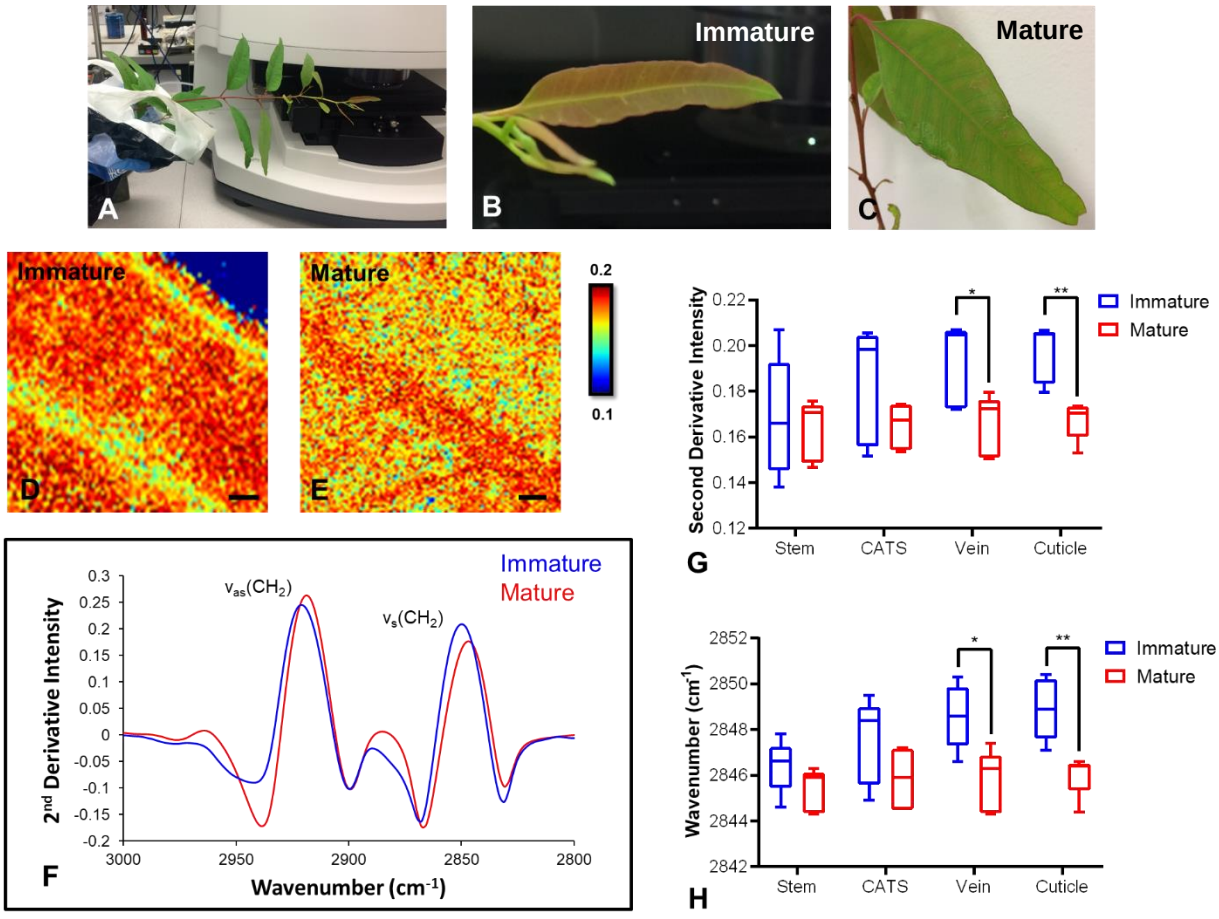

Figure 42: *FTIR reflectance spectroscopy enables longitudinal monitoring of epicuticular waxes. A–C) Representative optical images of the leaf of Eucalyptus sapling imaged at different time points depicting young (B) and 7 weeks older (C). D,E) False-color functional group images of wax layer, generated from second-derivative intensity of the $\nu_s(CH_2)$ absorbance band at 2848 cm^{-1}, showing increased intensity at 2848 cm^{-1} in the young leaf (D) compared to the same leaf 7 weeks later (E). F) Representative second-derivative FTIR reflectance spectra showing the shift of the $\nu_s(CH_2)$ band to lower wavenumbers, associated with leaf maturation. G,H) Statistical analysis of five replicates reveals differences in intensity (G) and peak positions (H) are significant for vein and cuticle and not for stem and cuticle adjacent to the stem (CATS). Data in (G) and (H) are presented as a box and whisker plots*

*showing the mean, upper, and lower quartiles. Error bars show the standard deviation. All statistical testing was undertaken using a two-way ANOVA, followed by post-hoc testing, as described in the Experimental Section. Each experimental group consists of five replicates (n = 5). Post-hoc testing was performed with t-tests, corrected for four multiple comparisons using the Bonferroni method and an alpha of 0.05 (two-tail testing). *p < 0.05, **p < 0.01. Scale bar (B,C) = 1 cm; (D,E) = 500 μm.*

4.2.7 Fourier Transform Infrared Reflectance Spectra of Ethylene Gassed Geraldton Wax

Geraldton wax is a Australia's leading native cut flower export, it is especially popular due to its various cultivars (ranging over 100) with unique colours and flower forms. (164) However, majority of Geraldton wax cultivars behave in the same way and are susceptible to ethylene exposure, resulting in shortened vase-lives. (164, 165) Varying studies utilising Ethephon (Figure 19) as a chemical ethylene promoter within several plants has been studied, looking at the resulting effects of ethylene gas on varying plants, reporting the abscission of flowers within a certain period so that subsequent flush of flowers occurs for harvesting, as well as its uses as a plant growth regulator in the case of different grains such as corn, maize, and sugar cane. (165-170) In the case of Geraldton wax sources of ethylene can occur from several places, this can include storage methods (where it is typically stored with ripening fruit and vegetables), engine exhaust fumes, environmental stressors or foliar, and soil borne diseases such as *Botrytis cinerea, Leveillula Taurica* (powdery mildew), *Alternaria alternata*. *Phytophthora* spp. and *Pythium* spp. to name a few. (164, 171, 172)

To further extend research into the use FTIR reflectance microspectroscopy to detect changes in plant physiology, case studies involving Geraldton wax with accelerated ageing (exposure to ethylene gas) was undertaken (following the preparation methods outlined in Chapter 2.3). Previous studies have looked at the effects of ethylene exposure on Geraldton wax postharvest, resulting in accelerating senescence, as well studies looking into the inhibition of ethylene release using ethylene antagonists such as 1-MCP in order to prevent and slowdown the ripening process. (173-175) Analysis

and changes as a result of ethylene gas have previously been reported through plant "vase-life", however, in-depth analysis of changes seen throughout the plant (e.g., changes in epicuticular wax) as a result haven't previously been looked at. These experiments provide an additional example, demonstrating the capability of FTIR reflectance spectroscopy to monitor changes to plant epicuticular waxes *in situ* in different plant species.

Initial studies on healthy Geraldton wax revealed spectroscopic differences during leaf maturation as seen in Figure 43 could be distinguished as was previously determined in Chapter 4.2.5. Once the spectroscopic foundations between immature and mature leaves was determined, distinctions between control and ethylene gassed needles (accelerated ageing) could be compared.

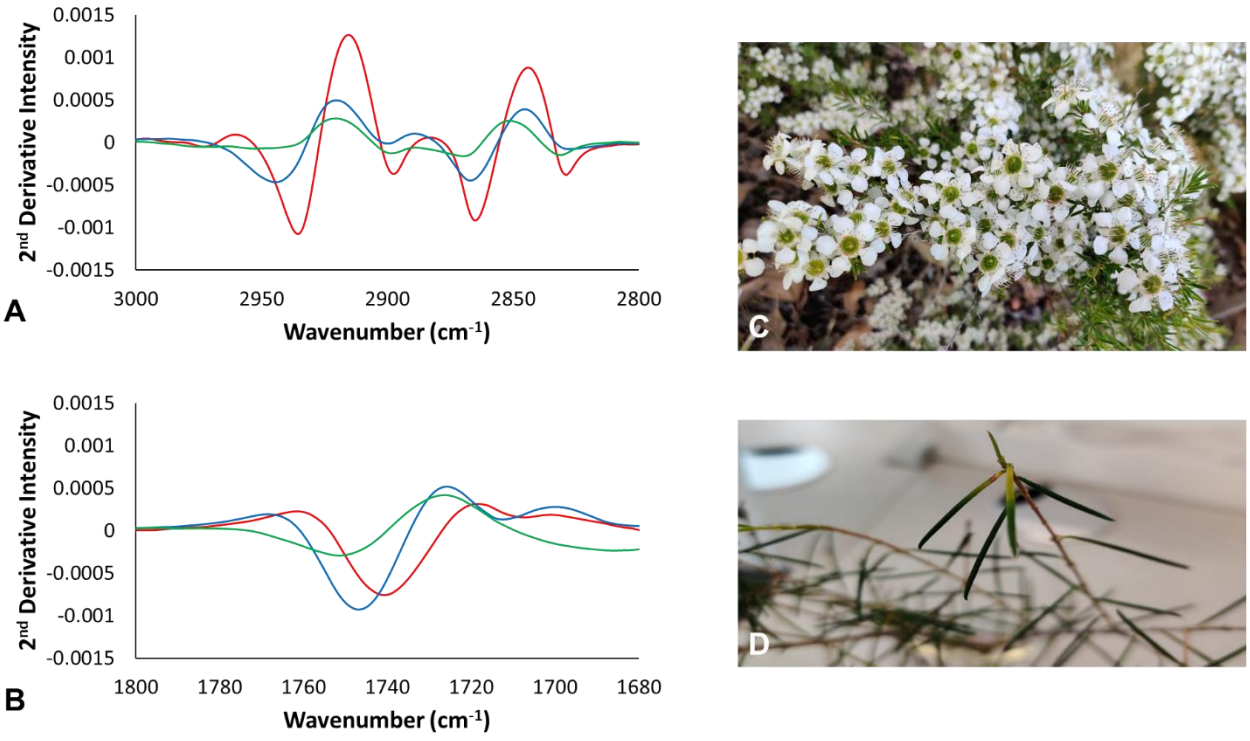

Figure 43: *FTIR reflectance spectroscopic imaging reveals spectroscopic differences associated with Geraldton wax (A,B), comparing different ages, mature (red), immature (blue), and sprouting needles (green). Spectral variance can be seen in* $\nu_s(CH_2)$ *peak intensity as well as slight* $\nu_s(CH_2)$ *shift in spectra (A), while changes in peak shift and intensity in* $\nu_s(CO)$ *region (B) can also be seen across different*

maturation stages. Representative Geraldton wax (C), where D displays needle-like leaf structures used for FTIR reflectance analysis.

A one-week time course between ethylene gassed and controlled Geraldton wax was undertaken, during which 4 different timepoints initial, 24 hr, 48 hr and one week were analysed. During this time the ethylene gassed Geraldton wax florets visibly fell off, after only 24 hrs, after 1 week the florets and majority of needles had also fallen off as the plant underwent senescence, while the control showed little to no senescence.

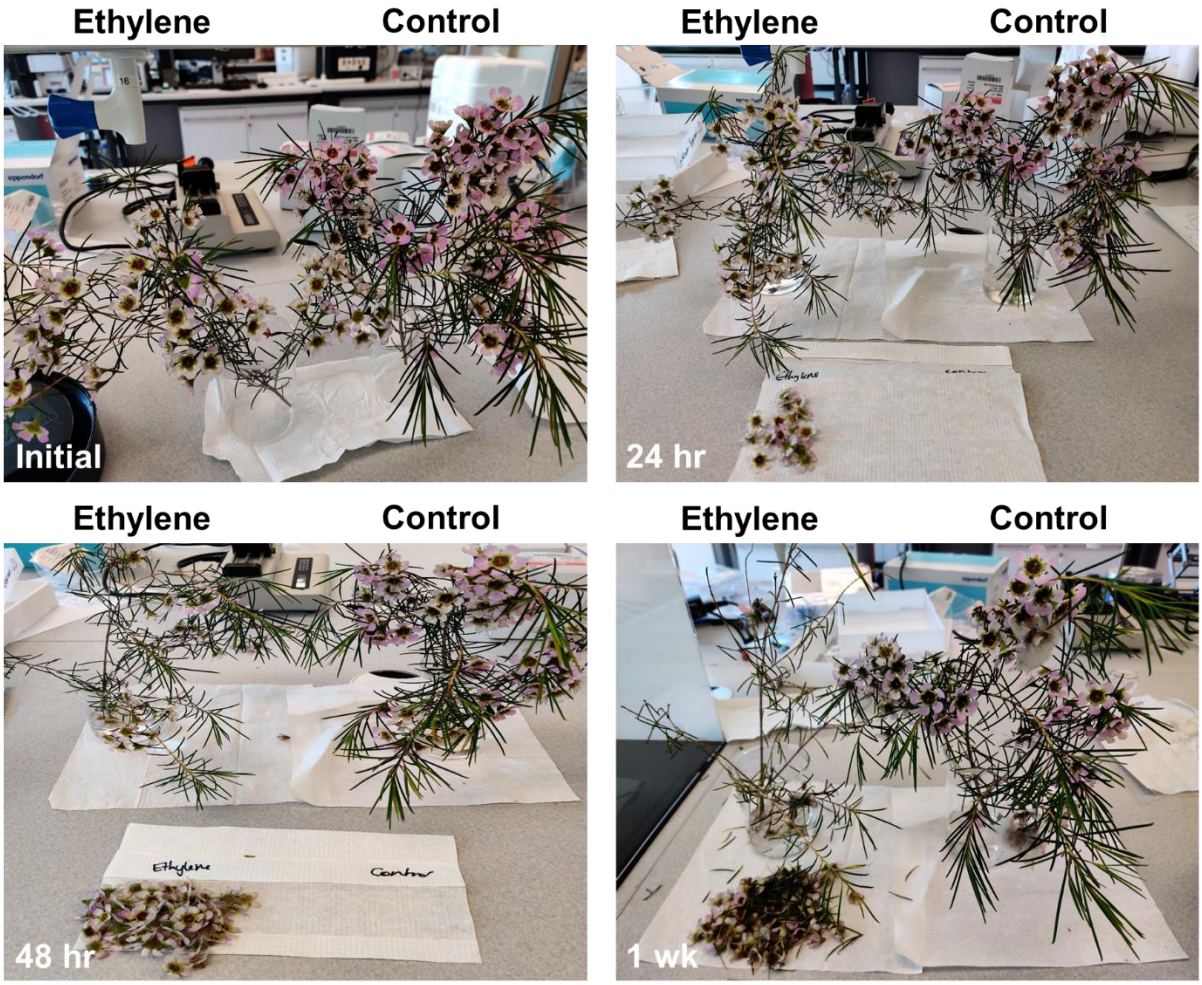

Figure 44: *Visual images of different time points taken during ethylene gassing time-course experiments including initial, 24 hour, 48 hour and 1 week studies. Ethylene gassed plants (Left) displaying significant flower loss over time in comparison to Geraldton wax controls (right).*

It is known that plants naturally release ethylene gas over time, however when higher concentrations of ethylene are present from external sources accelerated plant senescence occurs. FTIR microspecctroscopy was used to compare spectroscopic variations seen in epicuticular wax between ethylene gassed and un-gassed (control) Geraldton wax (Figure ZA-D). When examining FTIR results of Geraldton wax senescence, spectroscopic similarities were observed to the previous experiments investigating eucalyptus leaf maturation. Notably, a decrease in reflectance signals and shifts of characteristic $\nu_s(CH_2)$ band to lower wavenumbers was observed (Figure 45**E**). Two-way ANOVAs were performed comparing ethylene gassed and un-gassed Geraldton wax $\nu_s(CH_2)$ band intensity and wavenumber shifts in immature and mature needles (Figure ZF,G). It was found that while statistical significance between ethylene gassed and ungassed needles was found between varying ages, the relative *p* values found for signal intensity and band intensity were not statistically significant ($p = 0.3$ and $p = 0.1$). Post-hoc testing was performed on 24 hour ethylene gassed samples, with each group consisting of triplicate (n=3) replicates. The intensity of $\nu_s(CH_2)$ bands (measured at 2848 cm^{-1}) was found to have significant changed in mature needles ($p = 0.002$) while immature needles were not ($p = 0.2$), while wavenumber shifts of relative $\nu_s(CH_2)$ bands were found to be insignificant ($p = 0.2$, and $p = 0.07$, respectively) despite differences being present.

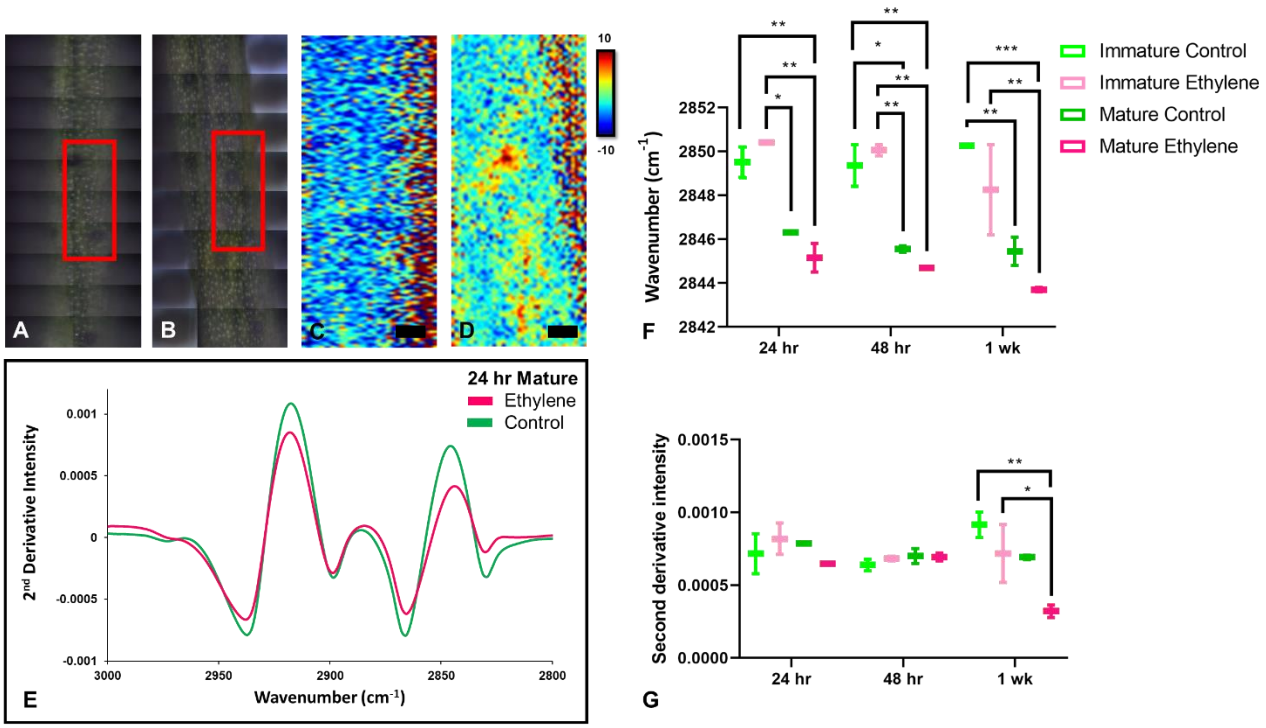

Figure 45: *FTIR reflectance spectroscopic imaging reveals consistent spectroscopic differences associated with leaf senescence as a result of ethylene gassing, comparing mature needles in a controlled environment after 24 hours against needles analysed 24 hours after ethylene gassing. A,B) False-color functional group images of wax layer, generated from second-derivative intensity of the ν_s(CH2) absorbance band at 2848 cm^{-1}, showing location of wax rich regions in mature 24 hour post gassing ethylene needles (C) and controlled needles (D). Representative mature 24 hour second-derivative spectra (E) reveal the decreased reflectivity in spectra from ethylene gassed needles in comparison to control and show a shift of ν_s(CH2) to lower wavenumbers in ethylene gassed compared to control. Statistical analysis of replicates reveals that the observed differences in peak position (E) and intensity (F) are significant. Data in (E) and (F) are presented as a box and whisker plots showing the mean, upper, and lower quartiles. Error bars show the standard deviation. All statistical testing was undertaken using a two-way ANOVA, followed by post-hoc testing, as described in the Experimental Section. Each experimental group consists of duplicates (n = 2). Post-hoc testing was performed with t-tests, corrected for three multiple comparisons using the Bonferroni method and an alpha of 0.05 (two-tail testing). *p < 0.05, **p < 0.01, ***p < 0.001. Scale bar = 100 µm*

Negligible differences in FTIR reflectance signals relating to the intensity and wavenumber $\nu_s(CH_2)$ band shifts were observed in Geraldton wax when comparing control/ethylene gassed pairings. However, differences between immature and mature leaves were still seen, similar to eucalyptus studies.

4.2.8 Fourier Transform Infrared Reflectance Spectra of Diseased Wheat Leaves During Progression of Fungal Infection

The capability and benefits of FTIR reflectance microspectroscopy were further demonstrated in a case study using wheat leaves infected with the fungal pathogen, Ptr, which causes yellow spot disease (Chapter 1). A set of infected (n = 5) and control (n = 5) wheat leaves were imaged (Figure 46) using FTIR reflectance imaging.

In the FTIR reflectance imaging data, a reduction of reflectance intensity and a subtle shift in position of the $\nu_s(CH_2)$ bands to higher wavenumbers were observed with increased proximity to the necrotic tissue (fungal infection resulting in dead tissue) in wheat (cv Scout rated susceptible to the disease) (Figure 46**E**). Statistical testing confirmed that the reduction in reflectance intensity was significant ($p < 0.01$); however, shifts in the peak position were not significant. The reduction in intensity of the ν_s(CH2) band (measured at 2848 cm^{-1}) was found to be significant both at the symptomatic, and in the asymptomatic tissue (p = 0.03 and p = 0.03) (Figure 46**E**). The later finding is significant as they confirm the presence of an impacted asymptomatic region where no visual signs of infection were present (Figure 46**A–D**), and thus FTIR reflectance imaging technique was shown to be capable of detecting subtle chemical differences in epicuticular waxes before visible leaf damage occurred.

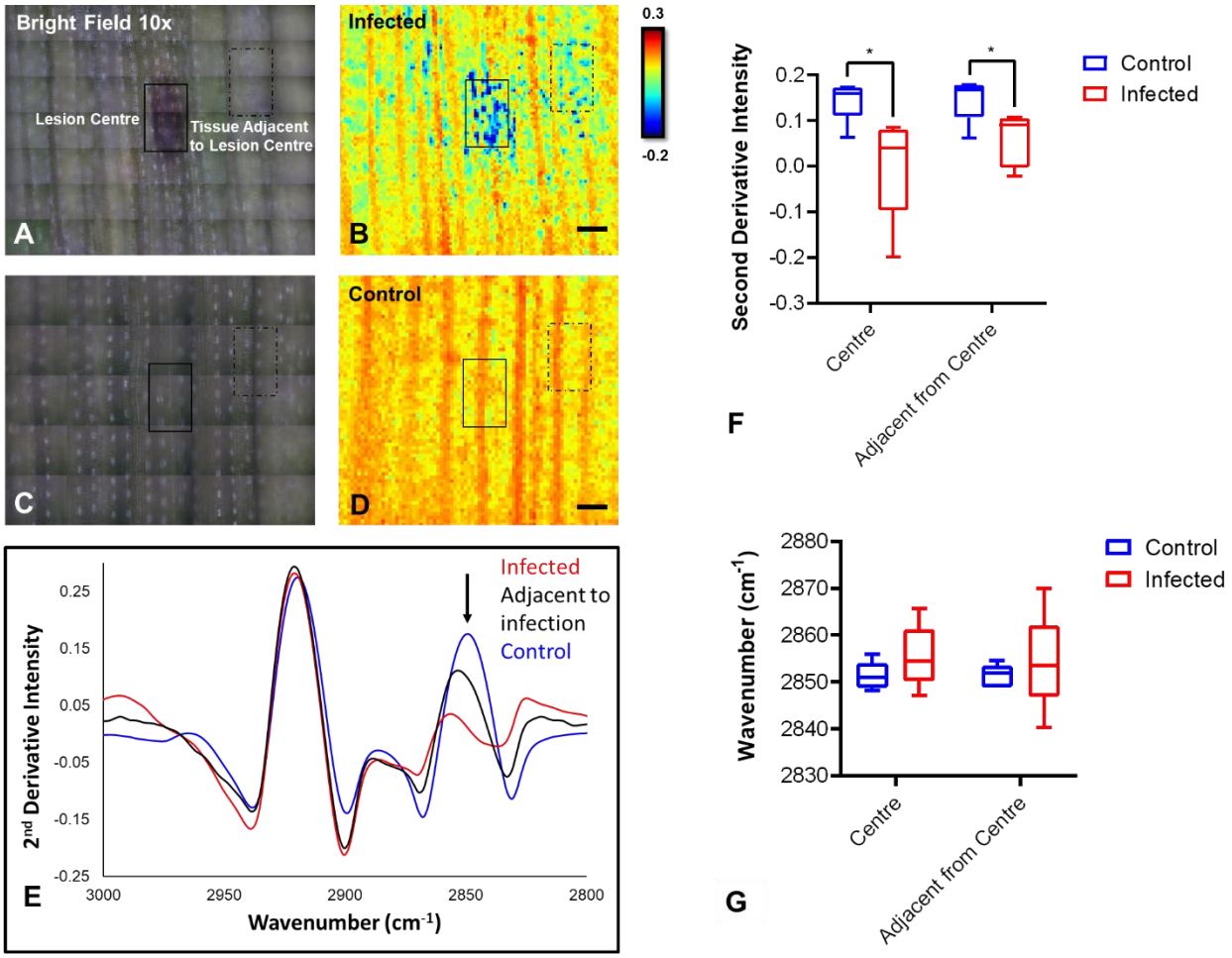

Figure 46: *FTIR reflectance spectroscopy enables monitoring of changes in epicuticular wax induced during plant–pathogen interactions in wheat (cv Scout). Bright field optical microscopy images (10× magnification) of control (A) and yellow spot infected (C) wheat leaf samples. FTIR reflectance false-color functional group images of wax layer generated from second-derivative intensity of the ν_s(CH2) absorbance band at 2848 cm^{-1} indicating differences between control (B) and infected (D) wheat leaf sections. Scale bar = 500 µm. Representative second-derivative FTIR reflectance spectra show the shift of the ν_s(CH2) band to higher wavenumbers closer to infected site (E). Statistical analysis of replicates reveals differences in intensity (F) but not in peak positions (G), between control and infected leaves. Data in (F) and (G) are presented as a box and whisker plots showing the mean, upper, and lower quartiles. Error bars show the standard deviation. All statistical testing was undertaken using a two-way ANOVA, followed by post-hoc testing, as described in the Chapter 2.9. Each experimental group consists of five replicates (n = 5). Post-hoc*

*testing was performed with t-tests, corrected for four multiple comparisons using the Bonferroni method and an alpha of 0.05 (two-tail testing). *p < 0.05.*

The detection of spectroscopic differences seen in wheat (cv Scout) prompted further investigation of the impact of Ptr infection in a moderately resistant wheat cultivar (cv Magenta) (Figure 47). It was found that the necrotic lesion in Magenta had larger intensity and peak shifts $\nu_s(CH_2)$ to lower wavenumbers in comparison to the lesion area in Scout ($p < 0.0001$) (Figure 47**E**). Large differences were present when looking at bright field optical and false colour images of Magenta infected with Ptr when comparing it to control (Figure 47**A-D**), differences seen across the surface epicuticular wax were further validated with SEM imaging, showing fungal hyphae on the surface of the symptomatic region (Figure 47**F**). The changes in the asymptomatic tissue were unremarkable with insignificant changes in intensity and wavenumber peak shifts for the $\nu_s(CH_2)$ band, the shifts seen were only statistically significant for the symptomatic region ($p < 0.0001$) (Figure 47**G,H**).

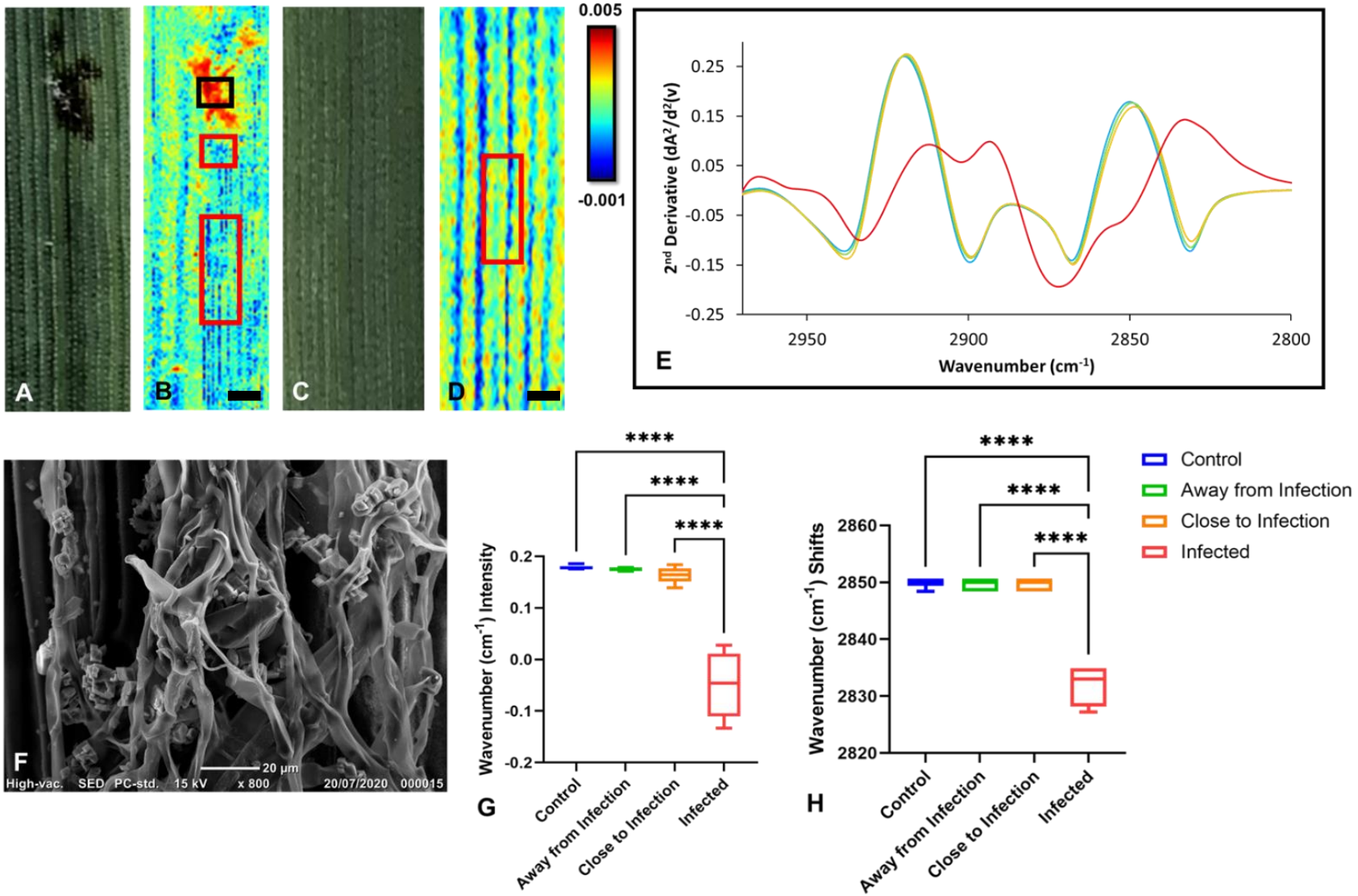

Figure 47: *FTIR reflectance spectroscopy enables monitoring of changes in epicuticular wax induced during plant–pathogen interactions wheat (cv Magenta). Optical bright-field images of infected (A) and control (C) wheat leaf sections. FTIR reflectance false-color functional group images*

*of wax layer generated from second-derivative intensity of the ν_s(CH2) absorbance band at 2848 cm^{-1} indicating differences between infected (B) and control (D) wheat leaf sections. Representative second-derivative FTIR reflectance spectra show the shift of the $\nu_s(CH_2)$ band to higher wavenumbers closer to infected site (E). Representative SEM image captured from the surface of the leaf, showing fungal hyphae on the surface of leaf section contributing to the infrared reflectance properties of the infected leaf surface (F). Statistical analysis of replicates reveals differences in intensity (G) and peak positions (H), between control and infected leaves. Data in (G) and (H) are presented as a box and whisker plots showing the mean, upper, and lower quartiles. Error bars show the standard deviation. All statistical testing was undertaken using an ordinary one-way ANOVA, followed by post-hoc testing, as described in the Chapter 2.9. Each experimental group consists of five replicates (n = 5). Post-hoc testing was performed with t-tests, corrected for four multiple comparisons using the Bonferroni method and an alpha of 0.05 (two-tail testing). ****p < 0.0001. Scale bar = 500 µm*

In summary, FTIR reflectance was able to reveal significant changes to the wheat epicuticular wax layer during the progression of disease. The wax layer directly on the surface of the symptomatic region was impacted the most compared to the surrounding asymptomatic tissue and the control leaf samples. Interestingly, the regions adjacent to the symptomatic tissue also showed significant spectroscopic changes despite no visible signs of leaf damage for the Scout cultivar only. This suggests that the epicuticular wax layer can potentially be an early dynamic marker of disease progression. This validation of FTIR reflectance imaging to detect crop disease has laid the groundwork to enable future mechanistic focused studies in a broad range of interacting systems to study plant tolerance to disease.

4.2.9 Fourier Transform Infrared Reflectance Spectra of Yellow Spot Infected Susceptible and Resistant Wheat Cultivars

Following the analysis of spectroscopic differences in wheat leaves during infection, a comparative analysis of two wheat cultivars rated susceptible (Scout) and moderately resistant (Magenta) to yellow spot disease, were undertaken. For this FTIR reflectance spectroscopy was used to analyse epicuticular waxes in the symptomatic regions and the asymptomatic regions (within the 1.5 mm of the symptomatic region).

Bright field optical images and false colour images displayed a clear difference in the symptomatic region in comparison to asymptomatic regions (Figure 48**A-D**). Spectral changes were observed for the symptomatic regions of Scout and Magenta (Figure 48**E**) with Magenta showing greater intensity and peak shifts $\nu_s(CH_2)$ to higher wavenumbers (Figure 48**E**). Despite these differences the spectral variations between the cultivars, the intensity and wavenumber shifts were not significant ($p = 0.69$ and $p = 0.052$ respectively) using paired t-tests (Figure 48**F,G**). When comparing reflectance spectra of healthy tissue with the infected symptomatic tissue, the degeneration of the wax region is obvious as a result of the infection, subsequently the otherwise prominent negative absorption in the $\nu_s(CH_2)$ wax peaks is no longer present. However, spectroscopic differences across the CH stretching region are still present. Therefore, additional spectral and statistical analysis was undertaken comparing both spectral intensity and peak shifts for bands centred at 2850 and 2915 cm^{-1}. It was observed that Scout had a much greater intensity and peak shift to higher wavenumbers for the ν(CH) band centre at 2915 cm^{-1} in comparison to Magenta (Figure 48**E**). The observed differences in peak intensity and wavenumber shift between species was found to be statistically significant ($p = 0.0009$ and $p = 0.017$ respectively) using paired *t*-tests (Figure 48**H,I**).

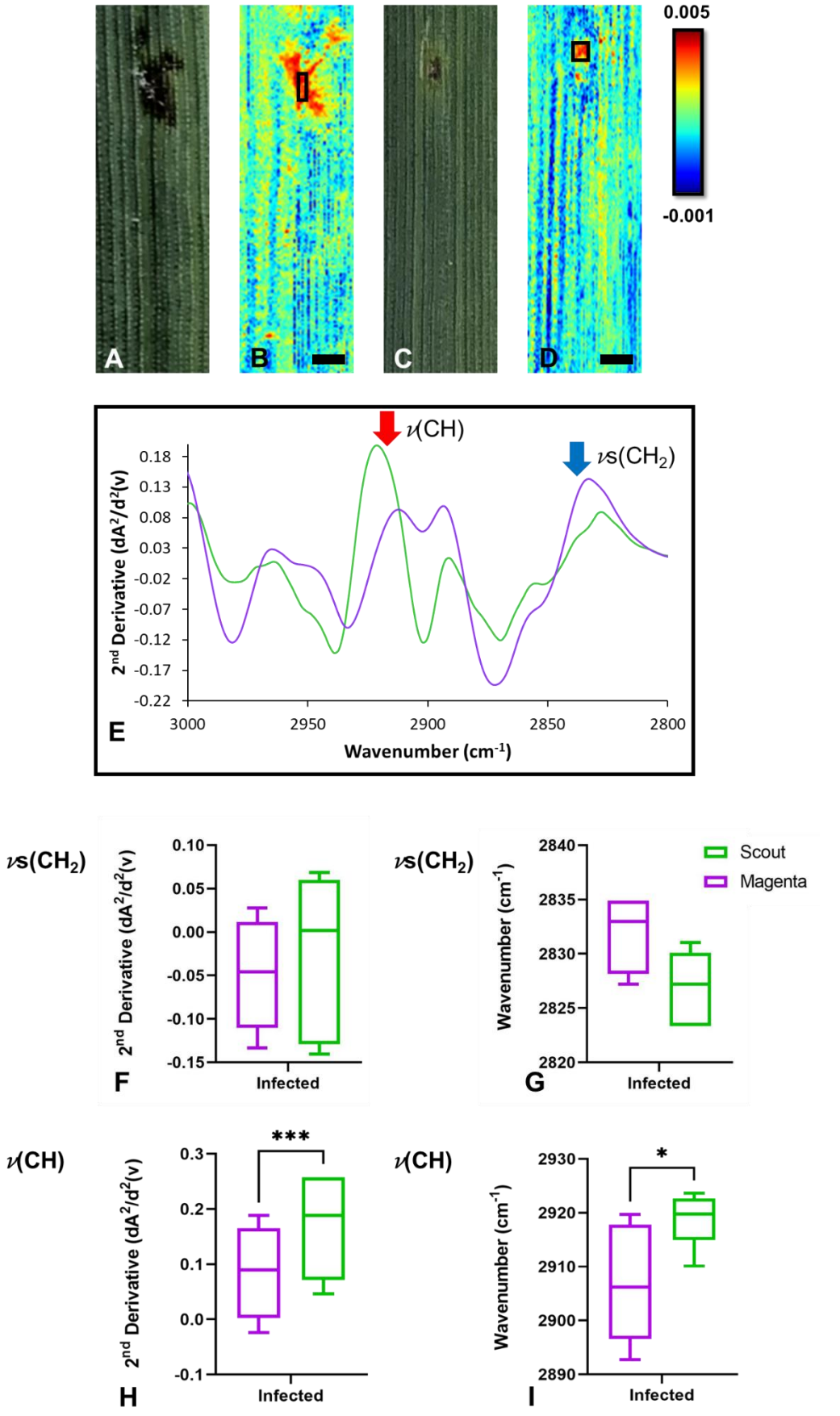

Figure 48: *FTIR reflectance spectroscopic imaging reveals spectroscopic differences associated with infection in two wheat cultivars (Magenta and Scout). Optical bright-field images of infected Magenta (A) and infected Scout (C) wheat leaf sections. False-*

colour functional group images of wax layer, generated from second-derivative intensity of the (CH) absorbance band at 2915 cm^{-1}, showing location of wax rich regions in Magenta (B) and Scout (D) cultivars. Representative second-derivative spectra (E) reveal a slight $\nu_s(CH_2)$ (blue arrow) and a large $\nu(CH)$ (red arrow) shift in spectra when comparing cultivars. Statistical analysis of replicate $\nu_s(CH_2)$ peaks observed no significant differences in intensity (F) and peak position (G), while differences observed in intensity (H) and peak position (I) for $\nu(CH)$ were seen to be statistically significant. Data in (F-I) are presented as a box and whisker plots showing the mean, upper, and lower quartiles. Error bars show the standard deviation. All statistical testing was undertaken using paired t-tests method and an alpha of 0.05 (two-tail testing). Each experimental group consists of five replicates (n = 5). Scale bar = 500 µm

Spectra of the asymptomatic region for infected Scout and Magenta leaf sections were also investigated to determine if increased susceptibility to yellow spot disease has direct effect on the epicuticular wax surface. Initial bright field and false colour images $\nu_s(CH_2)$ absorbance band at 2850 cm^{-1} displayed no clear differences between Magenta and Scout with unremarkable differences in wax distribution (Figure 49**A-D**), however it is important to note when looking at Figure 49**C,D**, a halo is present surrounding the necrotic lesion. Spectra between the two cultivars appeared visually similar with respect to peak intensities and shifts. (Figure 49**E**). The visual similarity was confirmed with statistical analysis which revealed no significant differences were present between areas adjacent to the necrotic lesion when comparing both intensity (p = 0.68) and wavenumber (p = 0.64) changes between Scout and Magenta using paired t-tests (Figure 49**F,G**).

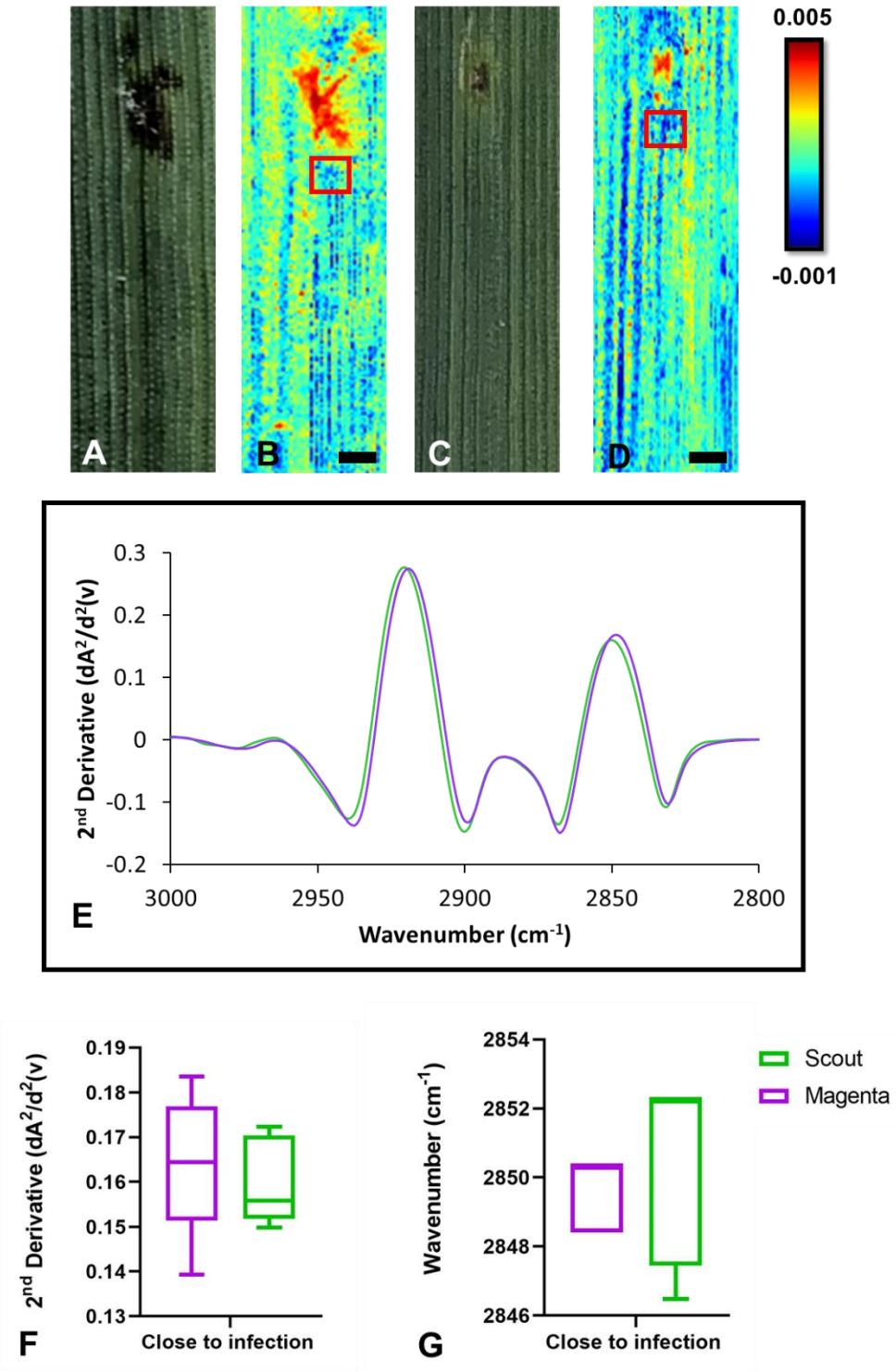

Figure 49: *FTIR reflectance spectroscopic imaging reveals spectroscopic similarities associated with the asymptomatic region of infected leaf, in Scout and Magenta. Optical bright-field images of infected Magenta (A) and infected Scout (C) wheat leaf sections. False-colour functional group images of wax layer, generated from second-derivative intensity of the ν_s(CH2) absorbance band at 2850 cm^{-1}, showing location*

of wax rich regions in Magenta (B) and Scout cultivars (D). Representative second-derivative spectra (E) reveal a slight $\nu_s(CH_2)$ shift in spectra when comparing cultivars. Statistical analysis of replicates reveals intensity (F) and peak position (G) are not significantly different. Data in (F) and (G) are presented as a box and whisker plots showing the mean, upper, and lower quartiles. Error bars show the standard deviation. All statistical testing was undertaken using paired t-tests method and an alpha of 0.05 (two-tail testing). Each experimental group consists of five replicates (n = 5). Scale bar = 500 µm

4.2.10 Fourier Transform Infrared Reflectance Spectra of Diseased Wheat Leaves Reveals Differences in Calcium Oxalate Accumulation in Wheat Infected with Ptr

When investigating spectroscopic differences between Scout and Magenta, a sharp absorbance band was observed at 1795 cm^{-1}, a spectral region normally void of absorbance bands in biological tissues (Figure 50**E,F**). A literature search indicated that the band could be assigned to calcium oxalate ν_s(CO). (176-178) Bright field optical and false colour FTIR functional group images generated from the calcium oxalate ν_s(CO) (1780 – 1820 cm^{-1}) band revealed presence of calcium oxalate in asymptomatic tissue immediately surrounding the necrotic lesion (Figure 50**A-D**). More interestingly, it can be seen that there is a greater concentration of calcium oxalate in Magenta (increased resistance to yellow spot disease) when compared to the highly susceptible Scout (Figure 50**C,D**) which may be a result of greater fungal hyphae density on the surface of infected Magenta tissue. SEM images displayed presence of crystal like structures, which maybe calcium oxalate crystals detected by FTIR on the surface of the necrotic lesion (Figure 50**G,H** respectively). When comparing the spectra of calcium oxalate between Magenta and Scout, no significant differences with respect to peak intensity or peak position were observed between stains ($p = 0.1$ and $p = 0.4$ respectively) (Figure 50**I,J**). However, the number and size of calcium oxalate deposits (Figure 51) was significantly greater in Magenta relative to Scout tissue (Figure 52, $p < 0.0028$).

The increased abundance of calcium oxalate in Magenta, which displays increased resistance to Yellow Spot disease was unexpected, however when comparing false-colour images of wheat between the two cultivars an increase in fungal hyphae in Magenta relative to Scout was observed and found to be concomitant with the bright-field images (Figure 50**A-D**). As the FTIR reflectance signal is highly surface sensitive, the calcium oxalate is therefore known to be located on the surface of the leaf (also supported by the SEM images), however it is unknown if the calcium oxalate on the surface of magenta is produced by the fungus, or by the wheat as a defence mechanism. Future studies involving naturally infected wheat samples from the field, could confirm whether the fungal hyphae grow on the leaf surface or if it is a result from artificial inoculation during glasshouse experiments. As a result, seeing whether Ca^{2+} oxalate is still present if there is no fungal hyphae growth using FTIR reflectance and SEM techniques would help determine the origin of the Ca^{2+} oxalate crystals. Nevertheless, due to wheat being a monocot the presence oxalate oxidase enzymes, would suggest that overtime calcium hotspots would be digested, leading to a depleting signal. To further investigate calcium accumulation and calcium oxalate in Yellow Spot disease, X-ray fluorescence microscopy was applied, which is described in the next chapter, Chapter 5.

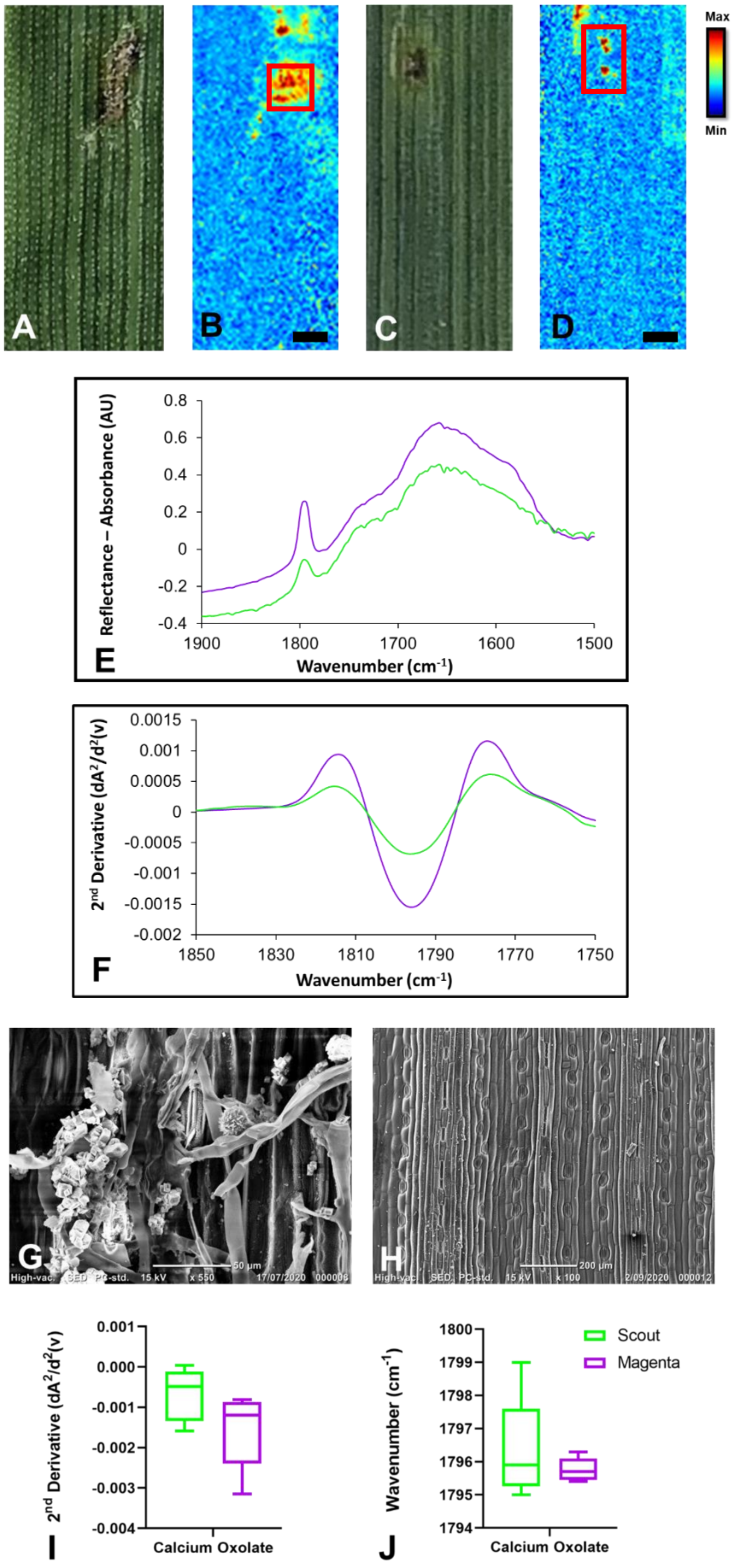

Figure 50: *FTIR reflectance spectroscopic imaging reveals spectroscopic differences associated between cultivars of Magenta and Scout when looking at calcium oxalate. Optical bright-field images of infected Magenta (A) and infected Scout (C) wheat leaf*

sections. False colour images of calcium oxalate, generated from second derivative intensity of ν_s(CO) absorbance band at 1795 cm^{-1}, showing locations of calcium oxalate in Magenta (B) and Scout (D) cultivars, in symptomatic regions. Representative raw and second-derivative spectra (E and F respectively) reveal changes in ν_s(CO) intensity and slight wavenumber shifts. SEM images display potential presence of calcium oxalate crystals present in both symptomatic (G) and asymptomatic regions (H). Statistical analysis of Scout and Magenta replicates reveals the observed differences in intensity (I) and peak position (J) are not different enough to be statistically significant. Data in (I) and (J) are presented as a box and whisker plots showing the mean, upper, and lower quartiles. Error bars show the standard deviation. All statistical testing was undertaken using paired t-tests method and an alpha of 0.05 (two-tail testing). Each experimental group consists of five replicates (n = 5). Scale bar = 500 µm (A-D) 50 µm (G) and 200 µm (H)

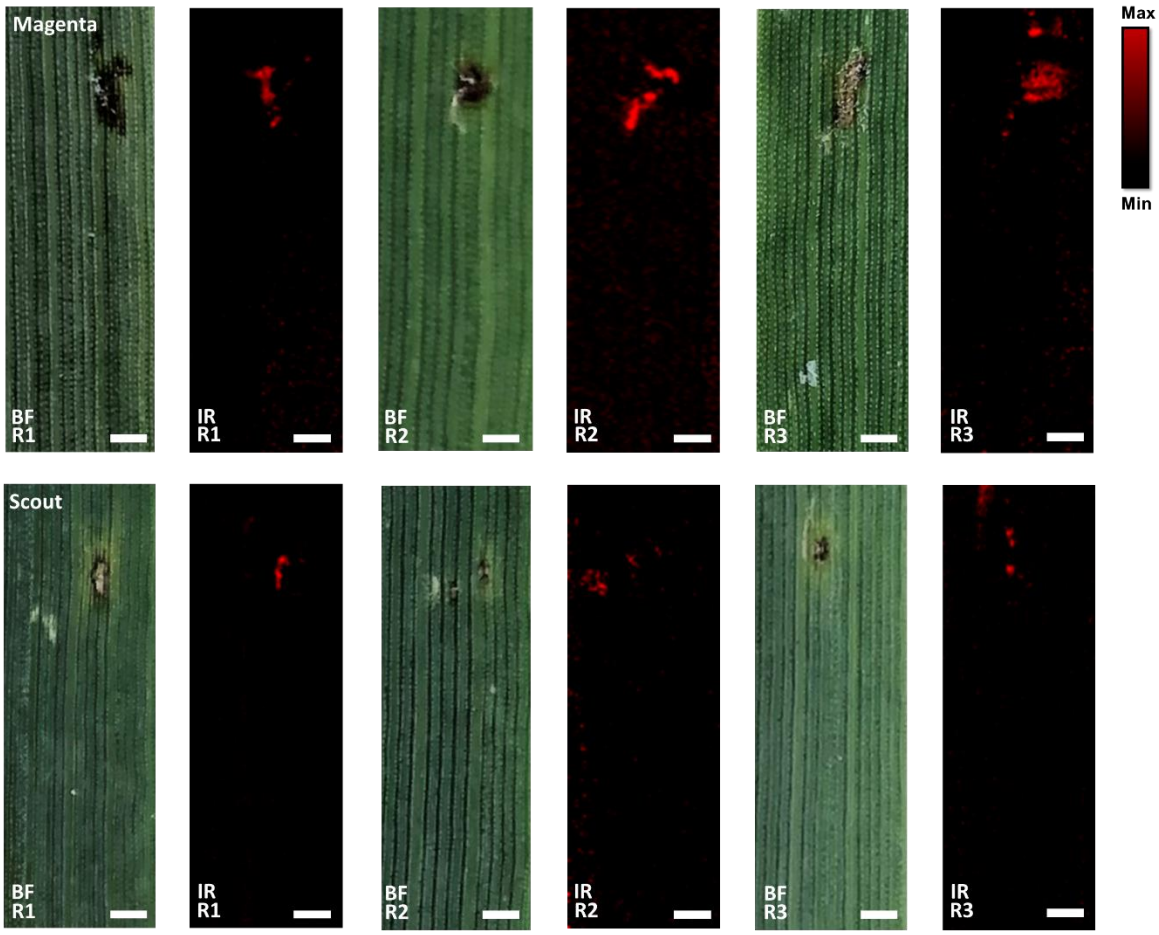

Figure 51: *Bright-field optical images (BF), Distribution of calcium oxalate ν_s(CO) absorbance band at 1795 cm^{-1} seen in red (IR), in 3 replicates (n=3) of wheat leaves*

infected with Ptr and harvested 6 days post inoculation for Magenta (Top) and Scout (Bottom) cultivars (R1-R3). Displaying an overall larger area of leaf surface containing calcium in infected Magenta leaf sections. Scale bar = 1 mm

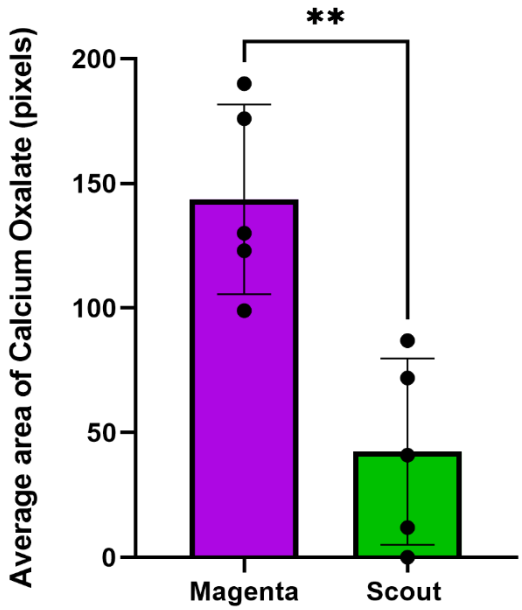

Figure 52: *Statistical analysis of average area of calcium oxalate (ν_s(CO) absorbance band at 1795 cm^{-1}) in pixels (of n = 5 for each species) reveals a significantly larger area in Magenta compared to Scout (p = 0.0028). Error bars show the standard deviation. All statistical testing was undertaken using student's t-tests method and an alpha of 0.05 (two-tail testing).*

4.3 Conclusions

This study has demonstrated and validated that FTIR reflectance microspectroscopic imaging can be used as a non-destructive chemical imaging tool for *in situ* and *ex vivo* or *in vivo* studies of plant epicuticular waxes. The FTIR reflectance spectra of the epicuticular wax layer vary with anatomical location on the plant leaf, and as a function of leaf maturation. While the first report of *in vivo* monitoring of plant epicuticular waxes was a success, care must be taken when drawing scientific conclusions from FTIR reflectance spectra, to avoid misinterpretation of the chemical information that they contain. Specifically, variation in the intensity of the reflectance

signal may result from variation in the wax content or variation in the thickness of the wax layer (which effects the extent of reflection). Nonetheless, this chapter has highlighted that plant physiology and response to disease can be imaged in associated to variation in the FTIR reflectance signal.

Future applications utilizing this method may include time course studies of the effects of various environmental stressors, such as disease, hyper-salinity, or soil contamination to enable dynamic analysis of the epicuticular wax layer. Such studies have the potential to yield important physiological insights to optimize mitigation or rehabilitation strategies to counter environment stress, to optimize crop harvests, and inform breeding programs. In addition, the method may find use as a non-destructive screening tool, to analyse large sample regions in order to identify smaller regions of interest for further analyses at higher spatial resolution using destructive techniques, such as ATR-FTIR mapping or MS approaches.

Lastly, FTIR reflectance microspectroscopy has revealed an apparent difference in calcium accumulation (varied surface accumulation of calcium oxalate) in two wheat cultivars infected with yellow spot disease. This observation was then investigated in further detail using X-ray fluorescence microscopy, as described in the next chapter, Chapter 5.

CHAPTER 5

Using Synchrotron X-Ray Fluorescence Microscopy to Characterise Changes in Calcium and Potassium Distribution in Infected Wheat Leaves

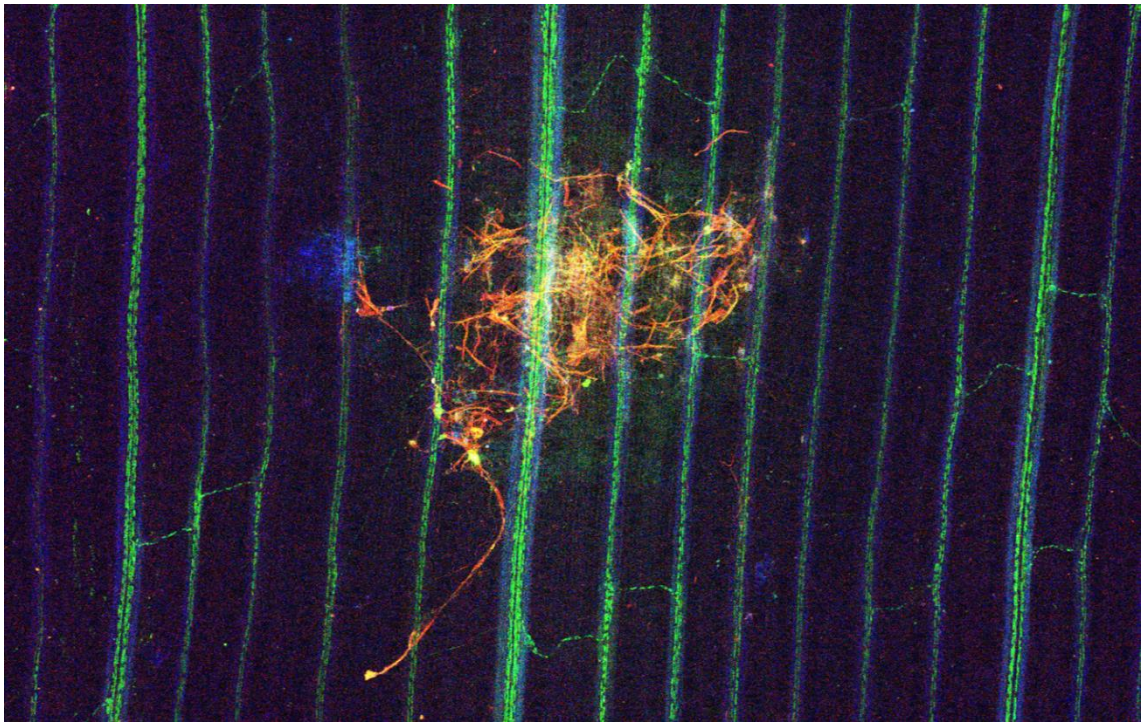

Components of the following chapter has data previously published in the Journal of Experimental Botany: Fatima Naim, Karina Khambatta, Lilian M. V. P. Sanglard, Georgina Sauzier, Julianne Reinhardt, David J. Patterson, Ayalsew Zerihun, Mark J. Hackett, and Mark R. Gibberd ***Synchrotron X-ray fluorescence microscopy-enabled elemental mapping illuminated the 'battle for nutrients' between plant and pathogen***. Journal of Experimental Botany. **2021** *72* (7), 2757-2768
DOI: 10.1093/jxb/erab005

5.1 Introduction

Metal ions such as K, Ca, Mn, Fe, Cu and Zn, are important macronutrients (K, Ca) or micronutrients (Mn, Fe, Cu, Zn), and are essential for plant development and growth. Plant fungal diseases (such as yellow spot, powdery mildew and leaf rust) are major biotic threats affecting wheat production, resulting in yield losses of up to 50%. (23) Understanding how plant physiology changes in response to the fungal infections, may reveal valuable information relating to disease pathology.

Current techniques that exist for the analysis of metal concentration and distribution within plants or tissue sections include X-ray fluorescence microscopy (XFM), laser ablation inductively coupled plasma spectrometry (LAICPMS), scanning electron microscopy coupled with X-ray spectroscopy (SEM), confocal microscopy among many more. All of these techniques have various advantages and disadvantages with respect to the analysis of metals within a plant specimen, which include: sample preparation time, detection limits, spatial resolution, and range of detectable elements. (179) Of the above listed techniques, XFM is one of the more favourable due to its straightforward sample preparation requirements, compatibility with analysis at ambient pressure (e.g., vacuum conditions not required), excellent detection limits, and micron spatial resolution, as previously described in Chapter 1. Although XFM is well suited to these experiments, a limitation is photodamage to the sample that can result in elemental redistribution. For the above reasons, XFM has found widespread use to determine and characterise transition metal distribution and abundance in numerous applications in the plant sciences. (98, 99, 103, 104, 180, 181) Despite the widespread application of XFM to study transition metal ions in the plant sciences, there has been relatively fewer studies using the technique to study the more mobile and diffusible metal ions from group 1 and 2, specifically K^+ and Ca^{2+}. This chapter has therefore, focussed on investigation and application of XFM to study K^+ and Ca^{2+} in the context of the plant sciences (specifically, wheat disease).

In Chapter 4 of this thesis, infrared reflectance methods were developed and then used to analyse the biochemical composition of the surface of leaves from wheat suffering yellow spot disease. The results pointed towards the presence of calcium oxalate

within the site of the necrotic lesion in infected leaves. Further, comparison across two different cultivars indicated reduced abundance of calcium oxalate in the cultivar with higher yellow spot resistance. These findings possibly implicate differences in calcium homeostasis in the underlying susceptibility/resistance of wheat to yellow spot disease. It is possible that the fungus *Pyrenophora tritici-repentis* releases oxalate, as a strategy to chelate Ca^{2+} ions, inhibiting numerous plant defence pathways otherwise activated by Ca^{2+}. As an example, plants are capable of detecting pathogen invasions and often the early response pathways include the redistribution of intracellular calcium. (85, 182) However, Monocotyledons such as wheat and barley contain oxalate oxidase enzymes, resulting in the digestion of calcium oxalate overtime, proposed to help maintain Ca^{2+} sensitive plant defence mechanisms. (183) One possibility for the accumulation of Ca^{2+} oxalate seen in infrared reflectance studies could be due to the artificial leaf surface inoculation of Ptr used in this disease model, which often leads to an abundance of fungal hyphae being present on the surface (where oxalate oxidase concentration is low, relative to internal plant tissue) and therefore enabling accumulation of calcium oxalate crystals. (184) An important question arising from the infrared reflectance studies is whether or not Ca^{2+} accumulates on the surface and internally within the leaf tissue, and is the distribution similar?

An important consideration when studying Ca^{2+} homeostasis is delineating between Ca^{2+} signals on the surface of the leaf (which is in direct contact with the fungal hyphae) and the Ca^{2+} signals that originate within the leaf tissue. This issue can be somewhat problematic for elemental mapping with XFM, where a 2D elemental map is generated from a 3D sample. One strategy to overcome this limitation is to use a confocal XFM optical configuration (as described in Ch1). Confocal XFM allows differentiation between 2D Ca^{2+} distributions recorded at different depths ("Z" position) within the sample. The first two objectives of this chapter were therefore, 1) to compare Ca^{2+} distributions (measured with XFM elemental mapping) between wheat cultivars resistant or susceptible to yellow spot disease, to help validate the findings observed using FTIR reflectance in Ch4 (i.e., increased calcium oxalate in resistant cultivar); and 2) use confocal XFM to determine if Ca^{2+} signals recorded from wheat levels originate from the leaf surface or from within the leaf tissue (or both).

Another integral macro nutrient required for plant health, in addition to Ca^{2+} is Potassium (K^+). As described in Chapter 1 of this thesis, K^+ is required for various transport and production of organics, activation of multiple enzymatic processes, regulation of osmotic pressure, and stomatal opening/closing functions. Given the immense value of K^+ to plant health, imaging the changes in K^+ distribution and concentration during crop disease is an important analytical capability to study disease pathways. XFM would appear as a technique well suited to image K^+ distribution (micron spatial resolution, vacuum conditions not required), but unfortunately K^+ has a relatively low atomic number (19) and therefore, low emission energies (Kα1 3314eV). This presents a significant challenge, as biological samples such as whole intact leaves (i.e., have not been sectioned) are relatively thick (~250 μm) leading to imaging distortions due to differences between the depth of penetration of the higher energy incident X-ray source, and the reduced escape depth of the lower energy K^+ Kα emission lines. (185) To overcome this problem, a method using Rb^+ as a surrogate for K^+ was developed, as Rb^+ mimics similar chemical and physiological properties of K^+, but with the added benefit of having a higher emission energy (Kα1 13395eV). Imagine Rb^+ distribution in plants, therefore, allows for more accurate monitoring of the distribution and concentration changes within whole/thicker wheat leaf samples.

Trace amounts of Rb^+ endogenously exist within plants; ranging between 0.54-30 mg/kg for grain and flour samples. (186) Previous studies have also shown that the relative toxicity for animals and plants with concerns to Rb^+ are relatively low and Rb^+ is often safe to use as a supplement for K^+.(187, 188) The final aim of this Chapter was to validate Rb^+ supplementation to plants, using Rb^+ as a surrogate for K^+, as an analytical strategy to assess 2D K^+ distributions from a larger volume of leaf tissue (i.e., less surface sensitive). This analytical capability is important as XFM elemental maps of transition metals (e.g., Fe, Mn, Cu, Zn) originate from the full thickness of leaf sections (as would Rb^+ maps), while K^+ maps originate primarily from the leaf surface. Therefore, the use of Rb^+ elemental maps as a marker of holistic plant health would enable more representative comparisons with transition metal maps (Fe, Mn, Cu, Zn), to better associate transition metal homeostasis with holistic plant health.

5.2 Results and Discussion

5.2.1 Utilising XFM to Associate Changes Seen in Calcium Distribution During Wheat Infection

Initial studies looking into calcium distribution in wheat (cv Scout and Magenta) using FTIR reflectance techniques (Chapter 4.2.10) displayed a change in calcium concentration relative to the presence of nectrotic infection. However, FTIR reflectance techniques are only capable of showing changes to the tissue at a surface level. Maia 2D XFM, pointed towards the presence of very fine and bright calcium hotspots on the surface, while lower intensity regions eluded to the presence of Ca^{2+} deeper within the plant tissue.

Longitudinal analysis of Ca^{2+} at different time points post infection revealed initial accumulation of calcium from 2 dpi to 4 dpi (Figure 53 **A**-**B**), followed by the depletion on the surface of wheat from 4 dpi to 8 dpi (Figure 53 **B**-**C**) in 4 replicate samples. This supports the idea that overtime the digestion of calcium oxalate occurs due to the presence of oxalate oxidase enzymes present in wheat (cv Magenta).

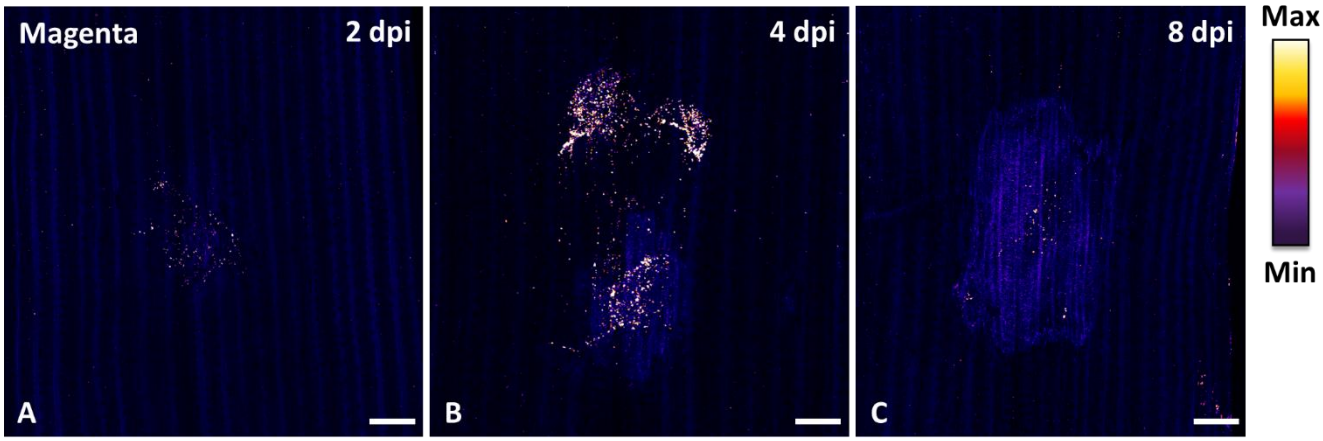

Figure 53: *2D Maia XFM false colour images of 2, 4 and 8 dpi, reveal the accumulation of Ca^{2+} 2-4 dpi and depletion of calcium during 4-8 dpi over time when comparing days post infection for wheat (cv Magenta). Scale bar = 1mm*

An investigation of Ca^{2+} distribution in *Triticum aestivum* cv Magenta and Scout was analysed 4 days post inoculation through the utilisation of XFM elemental mapping techniques. When analysing the Ca^{2+} metal distribution in wheat, the XFM elemental maps reveal accumulation of Ca^{2+} at the site of infection in both cultivars. (Figure 54) However, differences in the size of Ca^{2+} enriched lesions occurred between the cultivars (Figure 54), supporting findings found in IRM Chapter 2.4.10.

To investigate further the visual observations of increased Ca^{2+} accumulation in the Magenta cultivar, statistical analysis was undertaken to compare the total area encompassed by the Ca^{2+} accumulation. The statistical analysis demonstrated that the average total area of accumulated Ca^{2+} (Figure 55) was statistically significantly when comparing in Magenta relative to Scout tissue (Figure 55, $p = 0.0050$) Magenta is known to be more resistant to Ptr necrotic invasion in comparison to Scout, and therefore both the FTIR reflectance imaging results from Ch4, and the XFM elemental mapping results indicate increased abundance of Ca^{2+} enrichment in the more resistant wheat cultivar.

Consideration must be taken when interpreting the distributions of Ca^{2+} observed in infected whole wheat leaves. Due to the moderate Kα emission energy of Ca^{2+}, the Ca^{2+} distribution observed in Figure 53 arise form signal obtained from whole leaf, but with greatest sensitivity to Ca^{2+} localisations on or near the surface. This is an important consideration as the yellow spot fungus primarily grows on the leaf surface. Therefore, a question remains as to whether the Ca^{2+} accumulations observed during yellow spot infection occur on the leaf surface in association with fungal hyphae or does Ca^{2+} accumulate throughout the leaf. This prompted investigations into the possibility of using 3D confocal XFM, to observe how Ptr effects not only Ca^{2+} distribution in the surface and, also deeper within the leaf tissue.

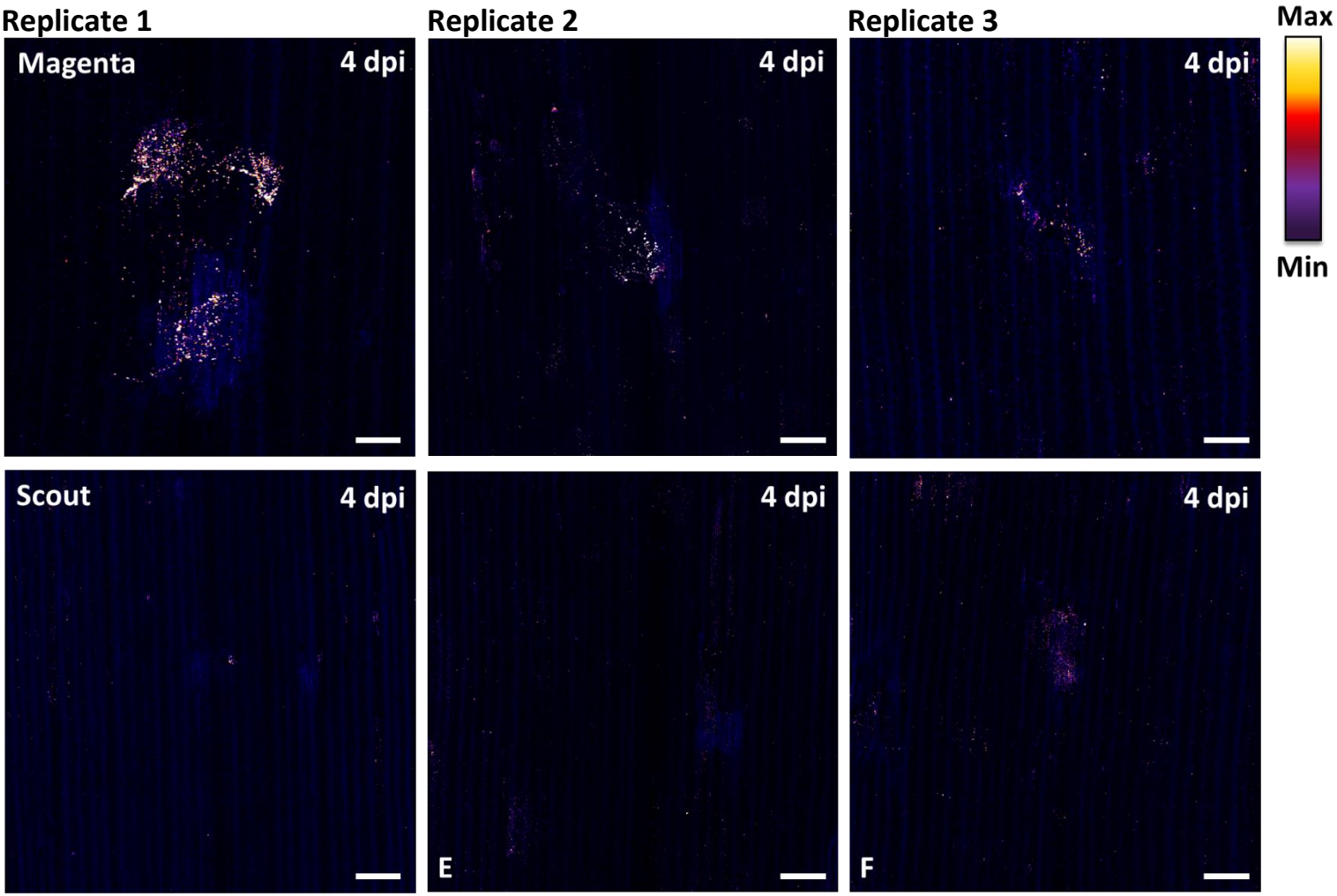

Figure 54: *2D Maia XFM false colour images reveal the presence of concentrated calcium hot spots around and within the necrotic lesion in Triticum aestivum cv Magenta and Scout cultivars after 4-days post infection. Scale bar = 1mm*

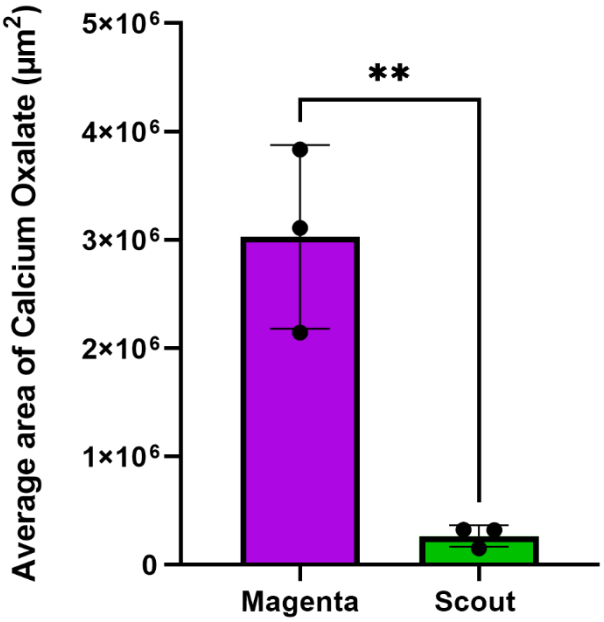

Figure 55: *Statistical analysis of Magenta and Scout replicates reveals the observed average area of calcium hot spots (Kα1 3691 eV) in µm² (of n = 3 for each species) having a much greater average area in Magenta when comparing to Scout (p = 0.0050). Error bars show the standard deviation. All statistical testing was undertaken using student's t-tests method and an alpha of 0.05 (two-tail testing).*

Following the investigations of Ca^{2+} distribution via 2D Maia XFM, 3D confocal XFM was chosen to investigate Ca^{2+} distribution at different tissue depths. This would confirm whether the changes being seen were mainly a result of surface Ca^{2+}, or whether Ca^{2+} present deeper within the plant tissue was also having an influence on the signal obtained.

Upon investigation with 3D confocal XFM (Figure 56) it can be seen that the Ca^{2+} distribution is most prominent on the surface of the wheat tissue, with highly localised Ca^{2+} accumilations and a distribution pattern following the surface growth of fungal hypae. However, confocal XFM maps acquired from deeper within the infected tissue reveal that the calcium accumulation is not just a surface phenomenom, with Ca^{2+} accumulation occuring up to 100 µm into the plant (Figure 56). Interestingly, the highly localised Ca^{2+} accumulations are only seen in images collected near the leaf surface (suggested to be calcium oxalate crystals), while confocal XFM maps from

deeper into the tissue reveal more diffuse Ca^{2+} accumualtion with an absence of focal "hotspots". When looking at theorised transmissions observed from different tissue thicknesses of leaf tissue, approximated to cellulose ($[C_6H_{10}O_5]_n$ Density = 1.5 g/cm^3) sample, it is observed that at ~3691 eV (Calcium's Kα emission energy) 35% of the Ca^{2+} signal is obtained (Figure 57). While a Ca^{2+} signal is still present at 100 µm. Consideration must be given as to whether the signal is lessened a result of less Ca^{2+} being present at the tissue site, and/or if it's a result of some self-absorption occurring. While it is still unclear whether or not the initial accumulation is a result of the hosts defence mechanism, or calcium oxalate accumulation as a result of artifical inoculation, it is evident that the presence of Ptr has an effect on Ca^{2+} homeostasis in the leaf tissue below the leaf surface.

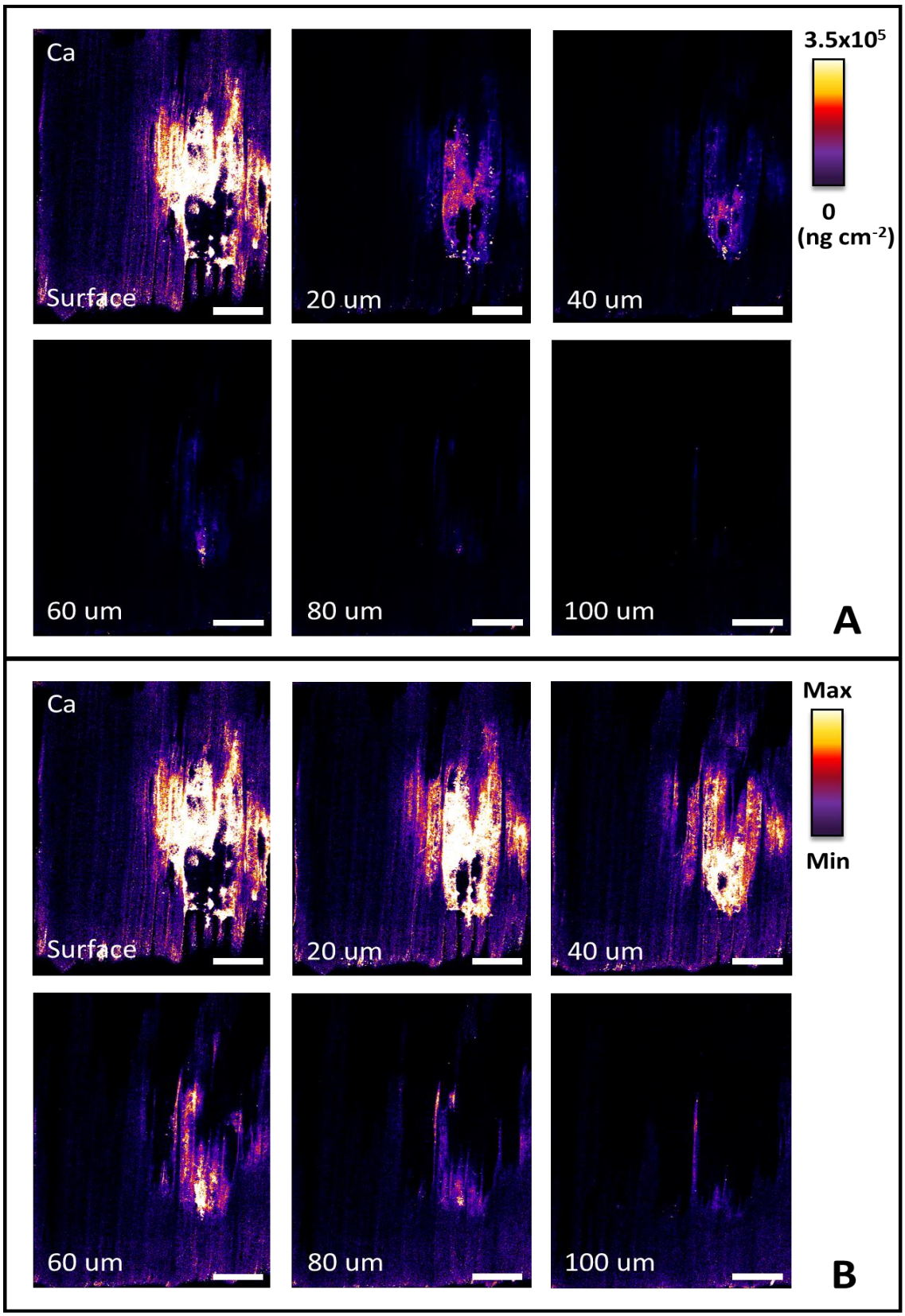

Figure 56: *Confocal 3D XFM false colour images showing calcium distribution at different depths of plant tissue. Quantitative scale (set A) and individual Min-Max scale (set B) Scale bar = 1mm*

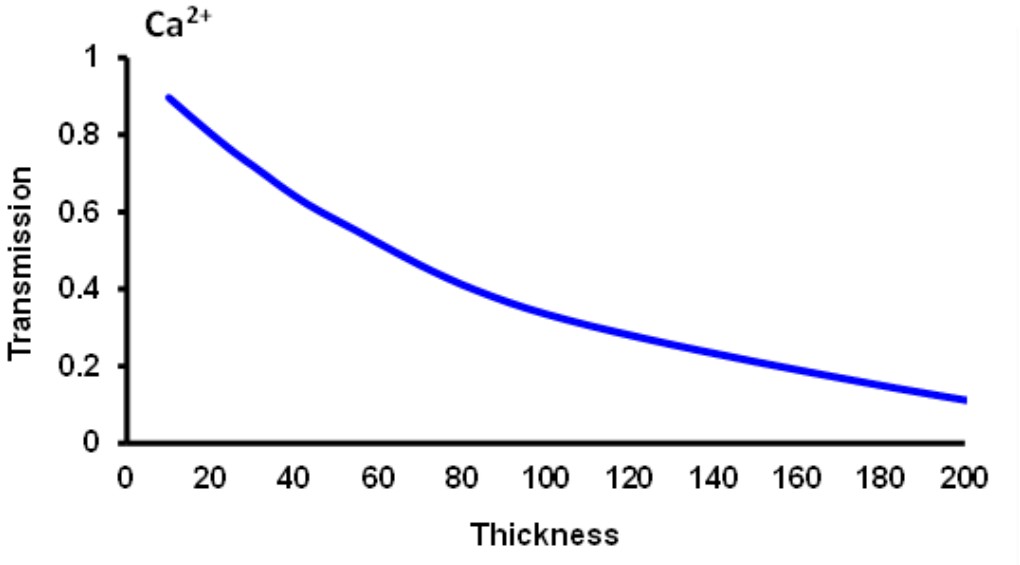

Figure 57: *Schematic reference of theorised Ca^{2+} transmission at different tissue thickness' using cellulose $[C_6H_{10}O_5]_n$ to approximate wheat tissue chemical composition and density.*

5.2.2 Developing Rb^+ XFM Tracing Protocols to Assess Changes to the Distribution of K^+, as a Marker for Plant Disease Pathology

Potassium exists as the K^+ ion in biology, is one of the most abundant elemental nutrients seen throughout a plant and is crucial to numerous physiological pathways that regulate plant health, and fitness. However, imaging K^+ distribution is often challenging due to its low Kα emission energy (~ 3300 eV). The low emission energy means X-ray emission from below the sample surface are easily absorbed by the sample, making it difficult to obtain sufficient signal response from internal leaf structures. Calculation of the expected X-ray transmission for a hypothetical 250 µm wheat sample, approximate to consist of cellulose ($[C_6H_{10}O_5]_n$ Density = 1.5 g/cm^3) (Figure 58) it is observed that at ~ 3300 eV (potassium's Kα emission energy) the transmission signal obtained from back of the sample (e.g., emission depth of 250 µm) is nearly 0%. This becomes problematic when wanting to look at whole wheat leaf samples, as the detected K^+ signal is mainly obtained from the sample surface, which may not represent the entire sample. This effect is not problematic for heavier elements

such as transition metals (Fe, Mn, Cu, Zn), which have higher energy emissions and therefore self-absorption becomes negligible.

One potential strategy to reveal K^+ distribution *in situ* within plant leaves is to image the distribution of a surrogate element, which has similar chemical properties but a higher emission energy. Such an opportunity is presented by Rb^+, which displays remarkably similar chemical and physiological function to K^+ in living cells. (125, 187) When observing Rubidium's transmission in a 250 µm cellulose sample at an emission energy of ~ 13395 eV transmissions of ~ 98% (Figure 58) are obtained meaning that the signal we observe from the sample is predominantly from the entire tissue in comparison to K^+ signal (as can be see, in Figure 58).

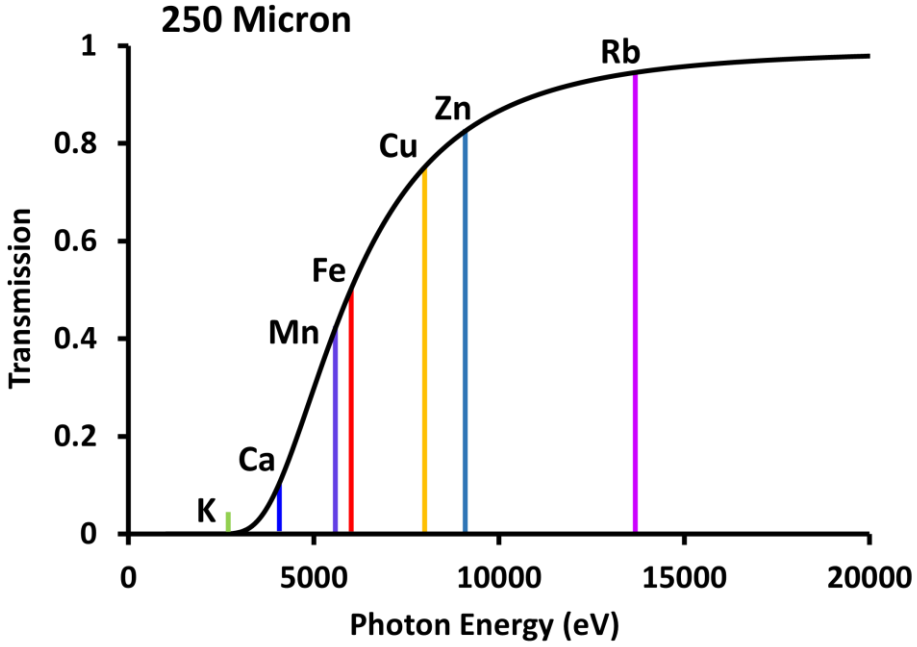

Figure 58: *Schematic reference of calculated X-ray attenuation in a 250 µm thick $C_6H_{10}O_5$ sample displaying transmission signal relative to the photon energy being distributed throughout the sample. Different line transmissions of varying metals, with key metals K^+ (green) line transmission ~ 0% of signal, Ca^{2+} (blue) line ~ 15% transmission, while Rb^+ (purple) line displays ~ 98% of rubidium would be detected within a 250 µm sample.*

A strategy to overcome analytical limitations associated with low K^+ X-ray emission energies, is to use of surrogate elemental marker with inherently higher X-ray emission energy. An ideal elemental for this is Rb^+, which shares many similar chemical properties to K^+, but has much higher Kα X-ray emission energy (13395 eV). In order to validate / develop Rb^+ elemental mapping as a marker of K^+ distribution, studies were first undertaken to test whether Rb^+ distribution followed the same trends as K^+. The initial work utilised XFM elemental mapping to compare localisation of Rb^+ and K^+ within 15 µm thick sectioned wheat (i.e., negligible self-absorption of Rb^+ and K^+ X-ray emission) and whole wheat leaf samples (Figure 59, 60). The wheat plants were grown with a watering regime containing 0%, 1% or 10% additional Rb^+ concentration, and, even in the case of no-added Rb^+ (0 % addition), a Rb^+ signal was obtained with sufficient signal/noise. However, for the sake of clearly representing Rb^+ and K^+ distribution overlaps, the following Figures 59-61 were taken from 10% doused Rb^+ plants, as due to time restraints, the whole wheat leaf images were only obtained from plants grown with the 10% Rb^+ addition water regime.

To assess whether K^+ and Rb^+ shared a similar distribution within the leaf tissue, elemental overlays (Figure 59**A-C**) and associations (Figure 59**D**) were used. As can be seen in (Figure 59**)**, strong co-localisation in elemental overlays (i.e., exclusively purple pixels produced from the overlay of blue Rb^+ and red K^+ pixels), and a linear association of Rb^+ and K^+ was present in the elemental association plots, for elemental maps from sectioned samples (e.g., thin samples with negligible self-absorption). The strong co-localisation and linear elemental association confirms that Rb^+ shares a very similar biological distribution as K^+ in the wheat leaf. However, when looking at elemental distributions in whole leaves (Figure 60**D**), higher concentrations of Rb^+ is seen in comparison to K^+. Further, the elemental associations from whole leaves revealed the presence of multiple clusters, whereas only a single cluster was observed in the elemental association from the thin sections. Similarly, the elemental overlays do not share the same degree of co-localisation as seen in the thin sections, as red and blue pixels are clearly evident in the elemental overlap. These results are interpreted to reflect mapping artifacts that result from self-absorption of the K^+ emission, with the K^+ elemental map largely arising from K^+ distributions near the leaf surface, while Rb^+ elemental maps represent the average throughout the whole leaf. As such, these

results provide strong support for the use of Rb^+ as a surrogate marker to image K^+ distribution in whole intact leaves.

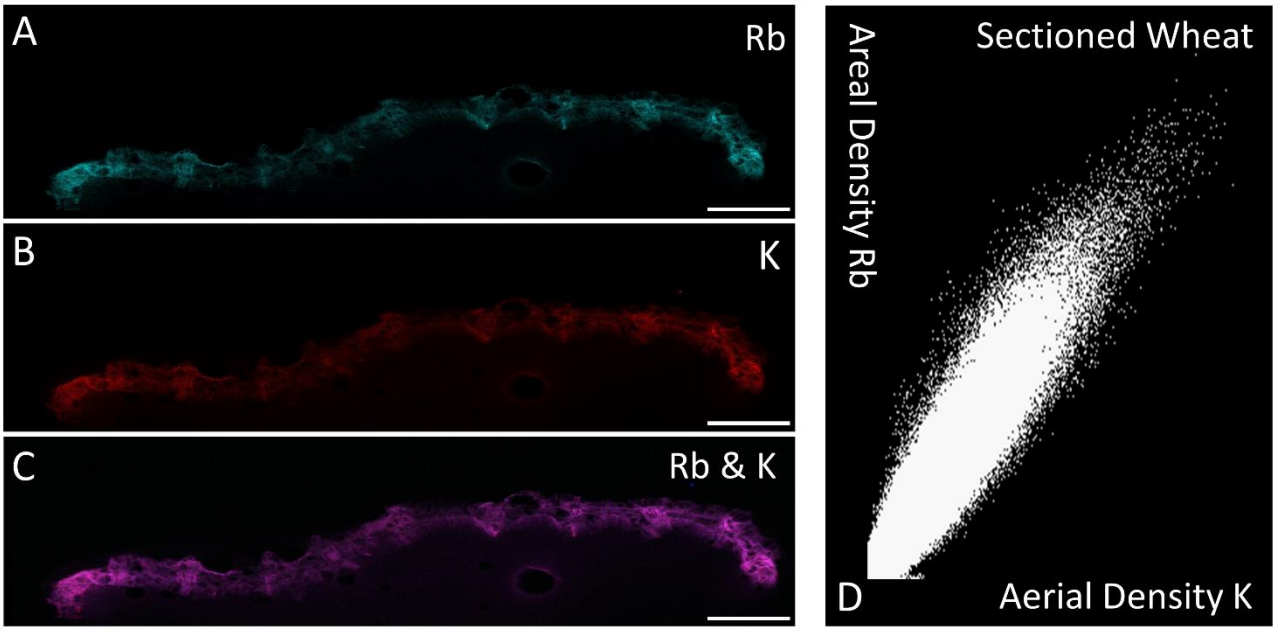

Figure 59: *15 µm thick sectioned Triticum aestivum cv Scout wheat samples analysed via 2D Maia XFM. False colour images showing distribution of Rb^+ (blue) (A) K^+ (red) (B) and an overlay image of both Rb^+ and K^+ (blue and red) (C) highlighting the overlap of Rb^+ and K^+ localisation. Areal density distribution of Rb^+ and K^+ in sectioned wheat display a linear correlation (D). Scale bar = 1mm*

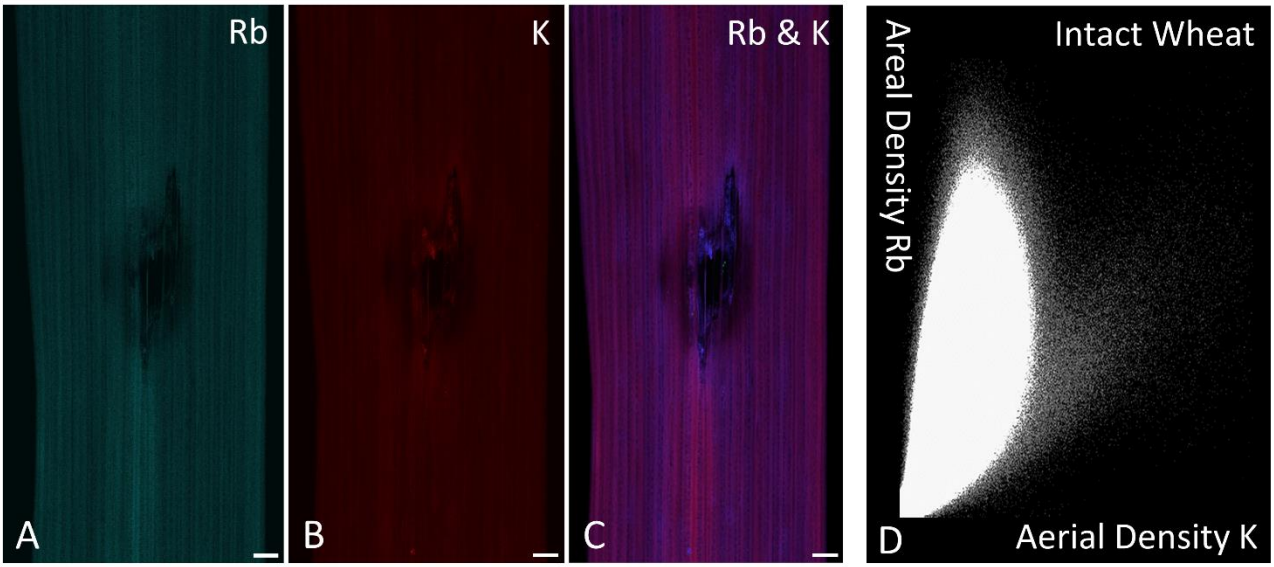

Figure 60: *Triticum aestivum cv Scout wheat samples analysed via 2D Maia XFM. False colour images showing distribution of Rb^+ (blue) (A) K^+ (red) (B) and an overlay image of both Rb^+ and K^+ (blue and red) (C) highlighting the overlap of Rb^+ and K^+ localisation. Areal density distribution of Rb^+ and K^+ in wheat display a heavier density of Rb^+ than K^+. Scale bar = 1mm*

To further exemplify the use of Rb^+ as a biomarker of K^+ a case study involving Rb^+ dosed infected and control wheat (cv Scout) was undertaken, highlighting advantages of Rb^+ due to its high Kα emission energies (13395 eV) and therefore negligible self-absorption. In this case, sample areas the size of the necrotic lesion were taken for greater clarity in identifying anatomical regions of the leaf. Infected and control leaves were analysed in triplicate, and not unexpectedly it was found that in general a much stronger Rb^+ signal was present in both the infected and healthy tissue when comparing K^+ signal (due to self-absorption of K^+ signal), as seen in (Figure 61 (**B-D**). Most importantly, both Rb^+ and K^+ displayed similar changes in relative content when comparing healthy tissue versus infected / damaged tissue. Specifically, the necrotic lesion can be clearly visualised in all Rb^+ and K^+ images on the basis of reduced elemental content, relative to surrounding non-infected tissue, or elemental maps from a control leaf (Figure 61). Within the infected lesion, greater definition of the veins can be seen in Rb^+ maps relative to K^+ (Figure 61), which is attributed to signal arising from the veins within the leaf and below the infected lesion on the leaf

surface, and therefore the maps reflect differences in self-absorption between Rb^+ and K^+ emissions.

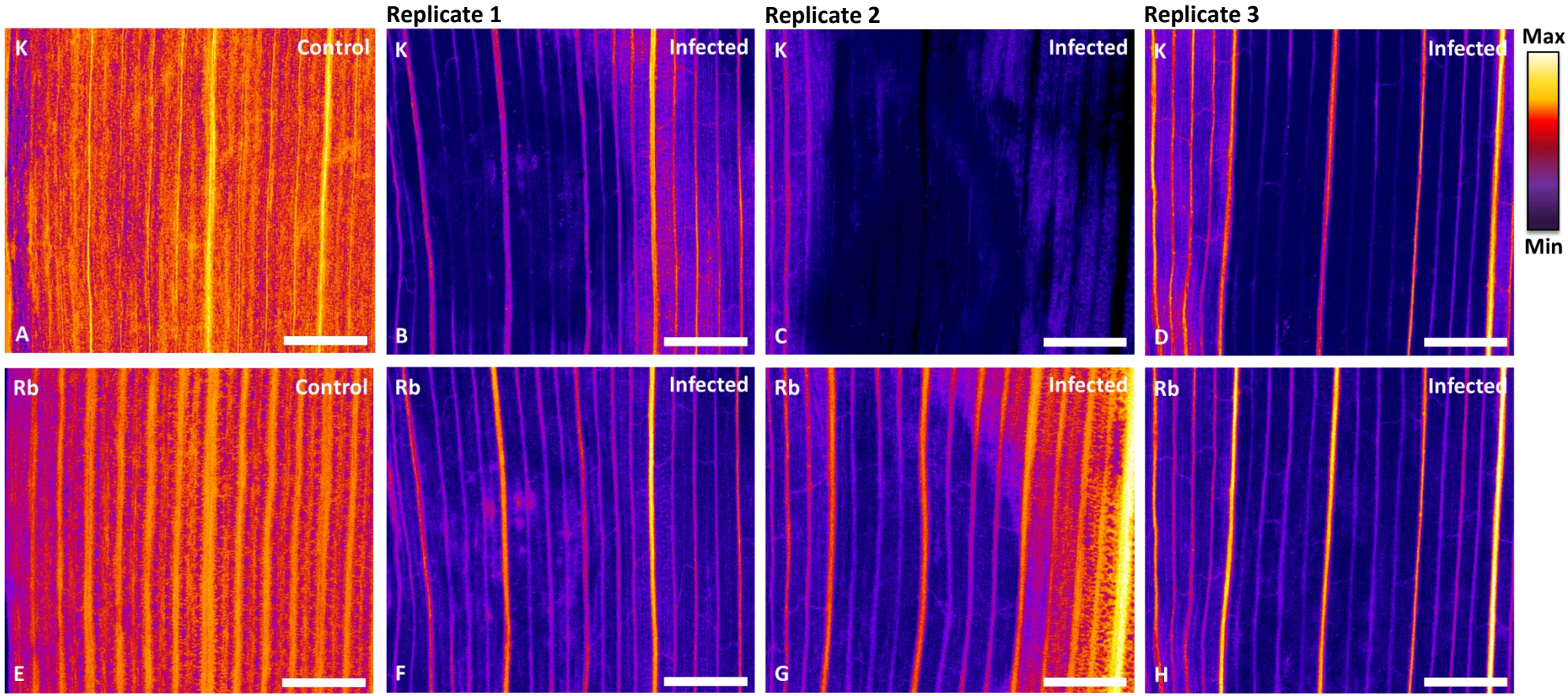

Figure 61: *Wheat (cv Scout) samples analysed using 2D Maia XFM. False colour images of paired control tissue displaying K^+ (A) and Rb^+ (E) intensity differences in whole wheat tissue. Triplicate false colour images displaying signal intensity of K^+ (B-D) and Rb^+ (F-H) in infected wheat. Scale bar = 1mm*

The results have demonstrated that potential to use Rb^+ as an elemental biomarker of K^+ for XFM elemental mapping of whole intact leaves, where the Rb^+ map (as a marker of K^+) represents signal form the entire leaf, and therefore, more comparable with elemental maps of transition metal ions. This capability can now be used to better associate alterations in transition metal ion homeostasis with changes in holistic plant health / pathology (as revealed by changes in Rb^+ distribution). In addition, the successful use of Rb^+ as a biomarker of K^+ in whole leaves, highlights the potential for an investigation into the use of Rb^+ to study K^+ distribution via confocal XFM. The ability to use Rb^+ as a tracer for K^+ enables capabilities to not only obtain chemical information from the surface of wheat but from the depths of the inner plant tissue. This could prove beneficial when looking at studies relating to growth and development via K^+ channels and potassium enzyme activation which happens within internal plant tissue, and not just the leaf surface which would otherwise not be picked up through direct XFM analysis of K^+. This allows for a better understanding of the effects on wheat via varying external factors such as infections, nutrition and drought. (189) Unfortunately, due to COVID restrictions and interruptions this could not be investigated fully in the time constrains of this PhD thesis and remains an area for future work.

5.3 Conclusions

This chapter has investigated changes in Ca^{2+} and K^+ in wheat leaves, during yellow spot disease, the results of which can provide valuable insights into plant health and fitness during disease. The initial studies of Ca^{2+} density on the surface of Ptr infected wheat revealed concomitant results in line with IRM data presented in Chapter 4.2.10. The distinct presence of Ca^{2+} on the surface of Ptr infected tissue must be further studied to elucidate whether these changes are a result of the hosts defence mechanism, Ptr leeching nutrients from the host or, a result of artificial inoculation leading to calcium oxalate crystals on the surface of fungal hyphae. The use of 3D confocal XFM revealed altered Ca^{2+} presence during Ptr infection on the surface, as well as, deep within the wheat tissue (100 µm). Unveiling the capability to potentially identify metabolic process' that could be affected as a result of wheat being infected. The use of 2D Maia XFM was utilised when comparing thin tissue samples (15 µm) to whole wheat tissue. It was found that the K^+ and Rb^+ signals in thin tissue samples had

identical overlap, in comparison to whole wheat tissue that differ due to K^+ self-absorption. This led to a signal being obtained from only the surface of wheat in comparison to Rb^+ signal being from almost the entire tissue and leading to an overall stronger signal with greater clarity. Using Rb^+ as a biomarker of K^+ during Ptr infection also displayed that both nutrients are affected in a similar fashion in symptomatic and asymptomatic tissue, further solidifying using Rb^+ as a surrogate of K^+. The use of Rb^+ as a biomarker of K^+ provides a holistic approach for monitoring the pathways that K^+ takes which would otherwise not be possible in whole tissue due to its low emission energy.

CHAPTER 6

Conclusions and Future Work

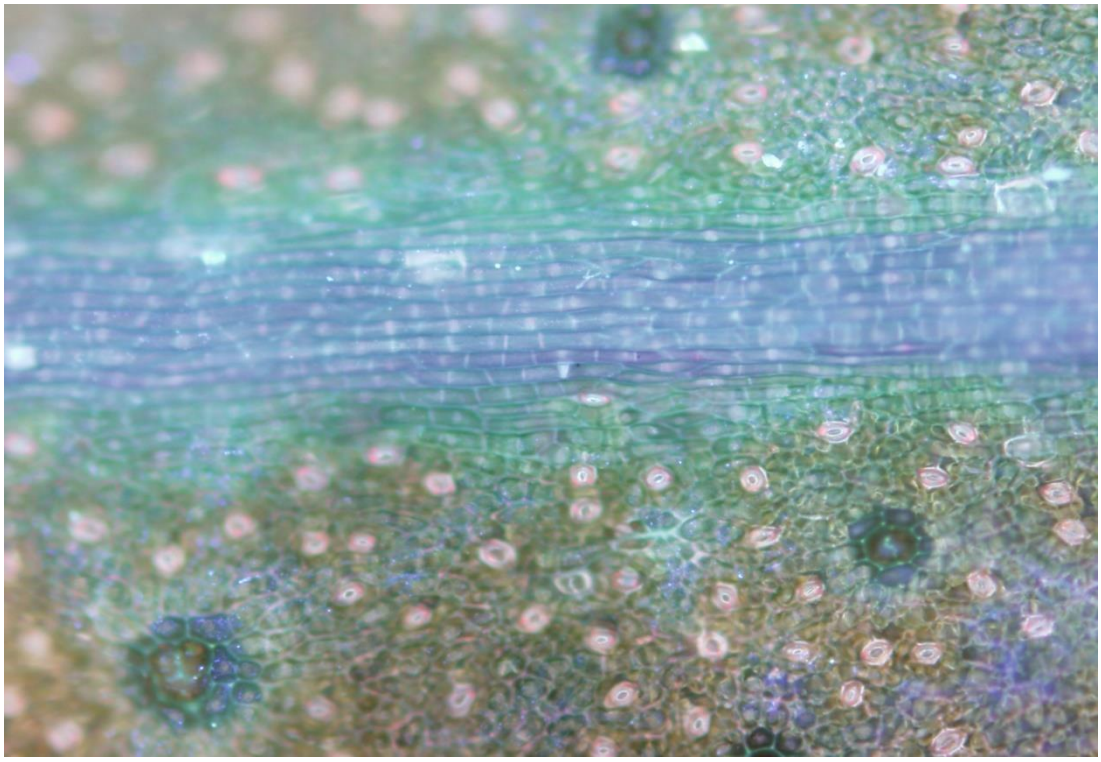

6.1 Conclusions

This thesis demonstrates the development, and applications of infrared (FTIR) and X-ray spectroscopic (XFM) techniques to study variation in epicuticular wax (FTIR) and distributions of diffusible metal ions such as K^+ and Ca^{2+} (XFM) within plants. The methods have been developed to enable future work to be understand the physiology of crop disease, with the ultimate aim of future knowledge gain being used to improve crop yields. The outcomes from the three results and discussion chapters (Chapters 3, 4 and 5, are described below).

In Chapter 3, ATR-FTIR spectroscopy was used to validate that the FTIR spectrum is sensitive to changes in the epicuticular wax coating on the surface of leaves, with changes observed between plant species and also changes in plant physiology (leaf maturation). These changes could be observed at a bulk level (bench top ATR-FTIR with thermal globar source), and prompted investigation at higher resolution using Synchrotron ATR-FTIR microspectroscopy. The synchrotron ATR-FTIR microspectroscopy studies demonstrated the potential to correlate wax constituents with plant anatomical structures such as, the cell well, and stoma cells. While these studies were important to validate assessment of plant epicuticular waxes as a biochemical marker, they also highlighted several limitations of ATR-FTIR spectroscopy. Firstly (and not surprisingly), the intensity of the ATR-FTIR spectroscopic signal was shown to be influenced by the surface topology of the leaf (confirmed by SEM imaging of the leaf surface). Secondly, and of particular relevance to the aims of this thesis, ATR-FTIR spectroscopy was shown to be destructive to the leaf surface, and therefore, not compatible with longitudinal time course monitoring.

Following from the outcomes of Chapter 3, Chapter 4 investigated FTIR reflectance spectroscopy as a non-destructive approach for the analysis of epicuticular waxes. Fortuitously, a pronounced FTIR-reflectance spectroscopic signal was observed from the surface of plant leaves, including shifts in the position of the (CH) bands as a function of changes to plant physiology (seasonal change and leaf maturation). More importantly, FTIR reflectance spectroscopy was shown capable of *in vivo* time-course monitoring of changes to plant epicuticular waxes, which is the first time this capability has been achieved However, this thesis has also highlighted that interpretation of FTIR reflectance spectra must be made with care. Variation in the

reflectance signal is known to occur as function of surface topology and refractive index, which can result in shifts or distortions to absorbance bands. (53, 54, 190, 191) Furthermore, it is unlikely that the spectra obtained are pure specular reflectance spectra, and some contribution from diffuse reflectance and transflection processes are probable, which complicates in-depth spectral interpretation. (190-193) In addition, the reflectivity of the surface is governed by film thickness, angle of incidence of the light source, and molecular orientation. (50, 53-55) Consequently, Lambert Beer law is not obeyed, and direct measurement of relative concentration is difficult, if not impossible using the reflectance signal. (55) Nonetheless, this thesis has highlighted the use of FTIR reflectance spectroscopy in a number of scenarios, and has been proven beneficial for the analysis of epicuticular waxes in relation to varying plant physiology and responses in relation to disease. Specifically, FTIR reflectance spectroscopy was shown capable of detecting changes in response to early stages of crop disease.

While using FTIR reflectance spectroscopy to investigate changes to the surface of wheat leaves during crop disease (yellow spot), an FTIR reflectance signal from Ca oxalate was observed. Further study of the Ca oxalate signal (as a marker of Ca homeostasis) indicated apparent differences in Ca homeostasis, during Ptr infection between two different cultivars of wheat, Magenta and Scout cultivars. This investigation then prompted studies into X-ray fluorescence microscopy to further study Ca^{2+} homeostasis (and other elements) during wheat infection (Chapter 5).

In Chapter 5, Initial studies of metals looking into Ca^{2+} density on the surface of wheat using X-ray fluorescence spectroscopy revealed concomitant results with infrared spectroscopy studies (specifically, increased Ca^{2+} accumulation in the wheat cultivar most resistant to yellow spot disease, Magenta cultivar). Furthermore, the use of 3D X-ray fluorescence imaging reveals Ca^{2+} distribution being present on both the surface, and deeply (100 µm) within the symptomatic leaf tissue. This points towards Ptr affecting plant process' and defense mechanisms not only on the surface, but deep within plant tissue. In addition to studies of Ca^{2+}, a method was developed to use Rb^{+} as a biomarker of K^{+}, circumventing image artifacts that arise as a result of the low X-ray emission energy and self-absorption. The ability to image Rb^{+} distribution throughout the whole plant leaf, as a marker of K^{+} better helps associate holist changes

in plant health (for which K^+ is a biomarker) with changes in transition metal ion homeostasis. Being able to monitor changes in metal concentrations and redistribution during plant infection provides valuable insights into plant metabolism and defense mechanisms alongside the fungal infections response to inhabiting a host.

6.2 Future Work

6.2.1 Future Work to Increase the Chemical Specificity of FTIR Reflectance Analysis of Epicuticular Waxes

Possibilities of future work using FTIR reflectance may enable more detailed information on the chemical composition and surface orientations of epicuticular waxes to be obtained, based on the peak positions and relative intensities observed in the reflectance spectra. These studies could possibly incorporate polarised light and angle resolved measurement to investigate molecular orientation, which may reveal new biochemical markers of plant physiology or pathology. At this stage however, regardless of the origin of the band shifts, their existence provides the ability to spatially and temporally resolve changes in the epicuticular wax layer, which in itself offers immense potential to study plant physiology and the effects of plant disease.

6.2.2 Studying Effects of Fruit Ripening on Epicuticular Wax Layers Using FTIR Reflectance Methods

Food wastage as a consequence of untimely fruit ripening is a massive economic concern, and US $1 trillion of fruit and vegetables are wasted around the world every year. (194) The mechanisms of wax bio-synthesis in fruit has been reported to be similar to leaves, and it appears that in addition to varying response to plant stress, the epicuticular wax layer of fruit influences sensing and signalling pathways, involved in fruit ripening. (195) Specifically, immediately prior to fruit ripening, there is a decrease in the amount of epicuticular wax on the surface of fruit, according to previous research using bulk extraction methods. (195) The reported thinning of the epicuticular wax layer is of significance, due to the role of ethylene gas diffusion in stimulating fruit ripening. Therefore, understanding the internal plant physiology and how this drives thinning of the epicuticular wax layer, and importantly, being able to detect such changes and how they vary in response to plant stress, may provide greater

control of the ethylene-induced ripening process. The agriculture industry is heavily invested in methods to control fruit ripening, therefore, improved understanding of the role of epicuticular waxes in fruit ripening, and improved ability to study the epicuticular wax layer of fruit, could be of immense value to the agriculture industry.

6.2.3 Investigating the Effects of Ptr on Different Calcium Compounds Using XANES

With a more expansive analysis using XANES to investigate Ca^{2+}, possibilities looking at different Ca^{2+} compounds existing in wheat also arise. Different Ca^{2+} compounds have a greater effect and change during fungal infection, looking into different regions of the wheat not directly correlated to the site of infection and observing how these Ca^{2+} compounds change in effect to Ptr may also be of great insight when analysing cultivar susceptibility. Lastly, building a spectral library and correlating FTIR reflectance data with overlapping XFM and XANES data (as previously observed with Ca^{2+} studies) to see if changes are concomitant in both inorganic and organic circumstances will provide a better link between processes involved as either a defence mechanism of the plant, or invasive methods that Ptr has in effect.

6.2.4 Using 3D Confocal XFM to Investigate Effects on K^+ Using Rb^+ as a Biomarker

While initial studies looking at 3D Confocal XFM revealed the depth of penetration that Ptr has effect on wheat tissue using calcium as a biomarker, the analysis of other diffusible ions such as K^+ (using Rb^+ as a marker) are of interest. As previously discussed, K^+ is one of the largest macronutrients contributing to plant health and fitness. Being able to measure distinct biomarkers such as K, Ca, Fe, Mn, Mg, Zn (Table 1) to differentiate between external plant stressors such as Ptr fungal infections and its effects on different cultivars as well as different defence mechanisms from the plants as a result will enable greater insight as to which wheat cultivar would be least susceptible to external plant stressors and therefore, optimal for mass agricultural consumption.

7.0 References

1. Sturtevant D, Lee Y-J, Chapman KD. Matrix assisted laser desorption/ionization-mass spectrometry imaging (MALDI-MSI) for direct visualization of plant metabolites in situ. Current Opinion in Biotechnology. 2016;37:53-60.

2. Vrkoslav V, Muck A, Cvačka J, Svatoš A. MALDI Imaging of Neutral Cuticular Lipids in Insects and Plants. Journal of the American Society for Mass Spectrometry. 2010;21(2):220-31.

3. Buschhaus C, Herz H, Jetter R. Chemical Composition of the Epicuticular and Intracuticular Wax Layers on Adaxial Sides of Rosa canina Leaves. Annals of Botany. 2007;100(7):1557-64.

4. Ribeiro da Luz B. Attenuated total reflectance spectroscopy of plant leaves: a tool for ecological and botanical studies. New Phytol. 2006;172(2):305-18.

5. Koch K, Barthlott W. Superhydrophobic and superhydrophilic plant surfaces: an inspiration for biomimetic materials. Philosophical Transactions of the Royal Society A: Mathematical, Physical and Engineering Sciences. 2009;367(1893):1487.

6. Andrae JW, McInerney FA, Tibby J, Henderson ACG, Hall PA, Marshall JC, et al. Variation in leaf wax n-alkane characteristics with climate in the broad-leaved paperbark (Melaleuca quinquenervia). Organic Geochemistry. 2019;130:33-42.

7. Medeiros CD, Falcão HM, Almeida-Cortez J, Santos DYAC, Oliveira AFM, Santos MG. Leaf epicuticular wax content changes under different rainfall regimes, and its removal affects the leaf chlorophyll content and gas exchanges of Aspidosperma pyrifolium in a seasonally dry tropical forest. South African Journal of Botany. 2017;111:267-74.

8. Harrington C, C. Carlson W. Morphology and Accumulation of Epicuticular Wax on Needles of Douglas-fir (Pseudotsuga menziesii var. menziesii)2015. 401-8 p.

9. Buschhaus C, Jetter R. Composition and Physiological Function of the Wax Layers Coating Arabidopsis Leaves: β-Amyrin Negatively Affects the Intracuticular Water Barrier. Plant Physiology. 2012;160(2):1120-9.

10. Figueiredo K, Oliveira M, Arruda E, C. F. Silva B, Santos M. Changes in leaf epicuticular wax, gas exchange and biochemistry metabolism between Jatropha mollissima and Jatropha curcas under semi-arid conditions 2015.

11. Shepherd T, Wynne Griffiths D. The effects of stress on plant cuticular waxes. New Phytologist. 2006;171(3):469-99.
12. Guo J, Xu W, Yu X, Shen H, Li H, Cheng D, et al. Cuticular Wax Accumulation Is Associated with Drought Tolerance in Wheat Near-Isogenic Lines. Frontiers in Plant Science. 2016;7:1809.
13. Huggins TD, Mohammed S, Sengodon P, Ibrahim AMH, Tilley M, Hays DB. Changes in leaf epicuticular wax load and its effect on leaf temperature and physiological traits in wheat cultivars (Triticum aestivum L.) exposed to high temperatures during anthesis. Journal of Agronomy and Crop Science. 2017;204(1):49-61.
14. Marom Z, Shtein I, Bar-On B. Stomatal Opening: The Role of Cell-Wall Mechanical Anisotropy and Its Analytical Relations to the Bio-composite Characteristics. Frontiers in Plant Science. 2017;8.
15. Kirkham MB. Chapter 24 - Stomatal Anatomy and Stomatal Resistance. In: Kirkham MB, editor. Principles of Soil and Plant Water Relations (Second Edition). Boston: Academic Press; 2014. p. 431-51.
16. Arya GC, Sarkar S, Manasherova E, Aharoni A, Cohen H. The Plant Cuticle: An Ancient Guardian Barrier Set Against Long-Standing Rivals. Frontiers in Plant Science. 2021;12.
17. Ziv C, Zhao Z, Gao YG, Xia Y. Multifunctional Roles of Plant Cuticle During Plant-Pathogen Interactions. Frontiers in Plant Science. 2018;9.
18. Bargel H, Neinhuis C. Tomato (Lycopersicon esculentum Mill.) fruit growth and ripening as related to the biomechanical properties of fruit skin and isolated cuticle. Journal of Experimental Botany. 2005;56(413):1049-60.
19. Woloshuk CP, Kolattukudy PE. Mechanism by which contact with plant cuticle triggers cutinase gene expression in the spores of Fusarium solani f. sp. pisi. Proceedings of the National Academy of Sciences. 1986;83(6):1704-8.
20. Wang B, Liang X, Gleason ML, Zhang R, Sun G. Genome sequence of the ectophytic fungus Ramichloridium luteum reveals unique evolutionary adaptations to plant surface niche. BMC Genomics. 2017;18(1):729.
21. Leroch M, Kleber A, Silva E, Coenen T, Koppenhöfer D, Shmaryahu A, et al. Transcriptome Profiling of Botrytis cinerea Conidial Germination Reveals Upregulation of Infection-Related Genes during the Prepenetration Stage. Eukaryotic Cell. 2013;12(4):614-26.

22. Lamari L, Bernier CC. Virulence of isolates of Pyrenophora tritici-repentis on 11 wheat cultivars and cytology of the differential host reactions. Canadian Journal of Plant Pathology. 1989;11(3):284-90.
23. Faris JD, Liu Z, Xu SS. Genetics of tan spot resistance in wheat. Theoretical and Applied Genetics. 2013;126(9):2197-217.
24. Manning VA, Chu AL, Steeves JE, Wolpert TJ, Ciuffetti LM. A host-selective toxin of Pyrenophora tritici-repentis, Ptr ToxA, induces photosystem changes and reactive oxygen species accumulation in sensitive wheat. Mol Plant Microbe Interact. 2009;22(6):665-76.
25. Pandelova I, Figueroa M, Wilhelm LJ, Manning VA, Mankaney AN, Mockler TC, et al. Host-Selective Toxins of Pyrenophora tritici-repentis Induce Common Responses Associated with Host Susceptibility. PLOS ONE. 2012;7(7):e40240.
26. Moolhuijzen P, See PT, Moffat CS. Exploration of wheat and pathogen transcriptomes during tan spot infection. BMC Research Notes. 2018;11(1):907.
27. Moffat CS, See PT, Oliver RP. Generation of a ToxA knockout strain of the wheat tan spot pathogen Pyrenophora tritici-repentis. Mol Plant Pathol. 2014;15(9):918-26.
28. Saur IML, Lawson AW, Schulze-Lefert P. Buy one, get two. Nature Plants. 2022;8(2):100-1.
29. Toruño TY, Stergiopoulos I, Coaker G. Plant-Pathogen Effectors: Cellular Probes Interfering with Plant Defenses in Spatial and Temporal Manners. Annu Rev Phytopathol. 2016;54:419-41.
30. Martelanc M, Vovk I, Simonovska B. Determination of three major triterpenoids in epicuticular wax of cabbage (Brassica oleracea L.) by high-performance liquid chromatography with UV and mass spectrometric detection. Journal of Chromatography A. 2007;1164(1):145-52.
31. Zeisler-Diehl V, Müller Y, Schreiber L. Epicuticular wax on leaf cuticles does not establish the transpiration barrier, which is essentially formed by intracuticular wax. Journal of Plant Physiology. 2018;227:66-74.
32. Weiglin C. Scanning electron microscopy of the leaf epicuticular waxes of the genus Gethyllis L. (Amaryllidaceae) and prospects for a further subdivision. South African Journal of Botany. 2001;67(2):333-43.

33. Grassl J, Taylor NL, Millar AH. Matrix-assisted laser desorption/ionisation mass spectrometry imaging and its development for plant protein imaging. Plant Methods. 2011;7:21-.
34. Infrared Spectroscopy. ACS Reagent Chemicals. ACS Reagent Chemicals: American Chemical Society; 2017.
35. Skoog DAHFJCSR. Principles of Instrumental Analysis. 2016.
36. Ozaki Y. Infrared Spectroscopy—Mid-infrared, Near-infrared, and Far-infrared/Terahertz Spectroscopy. Analytical Sciences. 2021;37(9):1193-212.
37. Vitha MF. Spectroscopy : principles and instrumentation. 2018.
38. Colthup NB, Daly LH, Wiberley SE. Introduction to Infrared and Raman Spectroscopy. In: Colthup NB, Daly LH, Wiberley SE, editors. Introduction to Infrared and Raman Spectroscopy (Third Edition). San Diego: Academic Press; 1990. p. xi-xii.
39. Griffiths PR. Fourier transform infrared spectrometry. Science. 1983;222(4621):297-302.
40. Nakano T, Kawata S. Evanescent-field scanning microscope with fourier-transform infrared spectrometer. Scanning. 1994;16(6):368-71.
41. Heredia-Guerrero JA, Benítez JJ, Domínguez E, Bayer IS, Cingolani R, Athanassiou A, et al. Infrared and Raman spectroscopic features of plant cuticles: a review. Frontiers in Plant Science. 2014;5(305).
42. Butler HJ, McAinsh MR, Adams S, Martin FL. Application of vibrational spectroscopy techniques to non-destructively monitor plant health and development. Analytical Methods. 2015;7(10):4059-70.
43. Vongsvivut J, Pérez-Guaita D, Wood BR, Heraud P, Khambatta K, Hartnell D, et al. Synchrotron macro ATR-FTIR microspectroscopy for high-resolution chemical mapping of single cells. Analyst. 2019;144(10):3226-38.
44. Miller LM, Dumas P. Chemical imaging of biological tissue with synchrotron infrared light. Biochimica et Biophysica Acta (BBA) - Biomembranes. 2006;1758(7):846-57.
45. Holman H-YN, Bechtel HA, Hao Z, Martin MC. Synchrotron IR Spectromicroscopy: Chemistry of Living Cells. Analytical Chemistry. 2010;82(21):8757-65.
46. Carr G, Reffner J, Williams G. Performance of an Infrared Micro Spectrometer at the NSLS. Review of Scientific Instruments. 1995;66:1490-2.

47. Chan KLA, Kazarian SG. New Opportunities in Micro- and Macro-Attenuated Total Reflection Infrared Spectroscopic Imaging: Spatial Resolution and Sampling Versatility. Appl Spectrosc. 2003;57(4):381-9.
48. Smith BC. Fundamentals of Fourier transform infrared spectroscopy. Boca Raton, FL: CRC Press; 2011.
49. Vongsvivut J, Pérez-Guaita D, Wood BR, Heraud P, Khambatta K, Hartnell D, et al. Synchrotron macro ATR-FTIR microspectroscopy for high-resolution chemical mapping of single cells. Analyst. 2019.
50. Yen YS, Wong JS. Infrared reflectance properties of surface thin films. The Journal of Physical Chemistry. 1989;93(20):7208-16.
51. Overs M, Hoffmann F, Schäfer HJ, Hühnerfuss H. Infrared Reflection−Absorption Spectroscopy of Racemic and Enantioenriched Methyl 17,18-Dihydroxyoctadecanoate at the Air−Water Interface. Langmuir. 2000;16(17):6995-8.
52. Hühnerfuss H, Hoffmann F, Simon-Kutscher J, Alpers W, Gade M. New chemical insights into the structure and morphology of sea slicks and their geophysical interpretations. In: Gade M, Hühnerfuss H, Korenowski GM, editors. Marine Surface Films: Chemical Characteristics, Influence on Air-Sea Interactions and Remote Sensing. Berlin, Heidelberg: Springer Berlin Heidelberg; 2006. p. 37-44.
53. Gericke A, Michailov AV, Hühnerfuss H. Polarized external infrared reflection-absorption spectrometry at the air/water interface: Comparison of experimental and theoretical results for different angles of incidence. Vibrational Spectroscopy. 1993;4(3):335-48.
54. Mendelsohn R, Mao G, Flach CR. Infrared reflection-absorption spectroscopy: principles and applications to lipid-protein interaction in Langmuir films. Biochim Biophys Acta. 2010;1798(4):788-800.
55. Meinders MB, van den Bosch GG, de Jongh HH. Adsorption properties of proteins at and near the air/water interface from IRRAS spectra of protein solutions. European Biophysics Journal. 2001;30(4):256-67.
56. Kumar S, Kumar S, Mohapatra T. Interaction Between Macro- and Micro-Nutrients in Plants. Frontiers in Plant Science. 2021;12.
57. Tripathi DK, Singh S, Gaur S, Singh S, Yadav V, Liu S, et al. Acquisition and Homeostasis of Iron in Higher Plants and Their Probable Role in Abiotic Stress Tolerance. Frontiers in Environmental Science. 2018;5.

58. Rai S, Singh PK, Mankotia S, Swain J, Satbhai SB. Iron homeostasis in plants and its crosstalk with copper, zinc, and manganese. Plant Stress. 2021;1:100008.
59. Hauer-Jákli M, Tränkner M. Critical Leaf Magnesium Thresholds and the Impact of Magnesium on Plant Growth and Photo-Oxidative Defense: A Systematic Review and Meta-Analysis From 70 Years of Research. Frontiers in Plant Science. 2019;10.
60. Broadley MR, White PJ, Hammond JP, Zelko I, Lux A. Zinc in plants. New Phytologist. 2007;173(4):677-702.
61. Alejandro S, Höller S, Meier B, Peiter E. Manganese in Plants: From Acquisition to Subcellular Allocation. Frontiers in plant science. 2020;11:300-.
62. Alvarez-Fernández A, Díaz-Benito P, Abadía A, López-Millán AF, Abadía J. Metal species involved in long distance metal transport in plants. Front Plant Sci. 2014;5:105.
63. Clemens S, Palmgren MG, Krämer U. A long way ahead: understanding and engineering plant metal accumulation. Trends in plant science. 2002;7(7):309-15.
64. Colangelo EP, Guerinot ML. Put the metal to the petal: metal uptake and transport throughout plants. Current opinion in plant biology. 2006;9(3):322-30.
65. Puig S, Peñarrubia L. Placing metal micronutrients in context: transport and distribution in plants. Current opinion in plant biology. 2009;12(3):299-306.
66. Haydon MJ, Cobbett CS. Transporters of ligands for essential metal ions in plants. New Phytologist. 2007;174(3):499-506.
67. Pettigrew WT. Potassium influences on yield and quality production for maize, wheat, soybean and cotton. Physiol Plant. 2008;133(4):670-81.
68. Naim F, Khambatta K, Sanglard LMVP, Sauzier G, Reinhardt J, Paterson DJ, et al. Synchrotron X-ray fluorescence microscopy-enabled elemental mapping illuminates the 'battle for nutrients' between plant and pathogen. Journal of experimental botany. 2021;72(7):2757-68.
69. Oosterhuis DM, Loka DA, Kawakami EM, Pettigrew WT. The physiology of potassium in crop production. Advances in agronomy. 2014;126:203-33.
70. Marschner H. Marschner's mineral nutrition of higher plants: Academic press; 2011.
71. Hepler PK, Vidali L, Cheung AY. Polarized cell growth in higher plants. Annual review of cell and developmental biology. 2001;17:159.

72. Kaiser WM. Correlation between changes in photosynthetic activity and changes in total protoplast volume in leaf tissue from hygro-, meso-and xerophytes under osmotic stress. Planta. 1982;154(6):538-45.
73. Hocking B, Tyerman SD, Burton RA, Gilliham M. Fruit calcium: transport and physiology. Frontiers in plant science. 2016;7:569.
74. Hochmal AK, Schulze S, Trompelt K, Hippler M. Calcium-dependent regulation of photosynthesis. Biochimica et Biophysica Acta (BBA)-Bioenergetics. 2015;1847(9):993-1003.
75. Vadassery J, Oelmüller R. Calcium signaling in pathogenic and beneficial plant microbe interactions: what can we learn from the interaction between Piriformospora indica and Arabidopsis thaliana. Plant Signal Behav. 2009;4(11):1024-7.
76. Aras S, Keles H, Bozkurt E. Physiological and histological responses of peach plants grafted onto different rootstocks under calcium deficiency conditions. Scientia Horticulturae. 2021;281:109967.
77. Gerwien F, Skrahina V, Kasper L, Hube B, Brunke S. Metals in fungal virulence. FEMS Microbiol Rev. 2018;42(1):fux050.
78. Fernandez J, Marroquin-Guzman M, Wilson RA. Mechanisms of Nutrient Acquisition and Utilization During Fungal Infections of Leaves. Annu Rev Phytopathol. 2014;52(1):155-74.
79. Shao D, Smith DL, Kabbage M, Roth MG. Effectors of Plant Necrotrophic Fungi. Frontiers in Plant Science. 2021;12.
80. Faris JD, Friesen TL. Plant genes hijacked by necrotrophic fungal pathogens. Curr Opin Plant Biol. 2020;56:74-80.
81. Morina F, Küpper H. Trace metals at the frontline of pathogen defence responses in non-hyperaccumulating plants. Journal of Experimental Botany. 2022;73(19):6516-24.
82. Fones H, Preston GM. The impact of transition metals on bacterial plant disease. FEMS Microbiol Rev. 2013;37(4):495-519.
83. Alvarez ME, Pennell RI, Meijer PJ, Ishikawa A, Dixon RA, Lamb C. Reactive oxygen intermediates mediate a systemic signal network in the establishment of plant immunity. Cell. 1998;92(6):773-84.
84. Torres MA, Jones JDG, Dangl JL. Reactive Oxygen Species Signaling in Response to Pathogens. Plant Physiology. 2006;141(2):373-8.

85. Bose J, Pottosin I, Shabala S, Palmgren M, Shabala S. Calcium Efflux Systems in Stress Signaling and Adaptation in Plants. Frontiers in Plant Science. 2011;2.
86. Aldon D, Mbengue M, Mazars C, Galaud JP. Calcium Signalling in Plant Biotic Interactions. Int J Mol Sci. 2018;19(3).
87. Hood MI, Skaar EP. Nutritional immunity: transition metals at the pathogen–host interface. Nature Reviews Microbiology. 2012;10(8):525-37.
88. Núñez G, Sakamoto K, Soares MP. Innate Nutritional Immunity. J Immunol. 2018;201(1):11-8.
89. Cabot C, Martos S, Llugany M, Gallego B, Tolrà R, Poschenrieder C. A Role for Zinc in Plant Defense Against Pathogens and Herbivores. Frontiers in Plant Science. 2019;10.
90. Thomma BPHJ, Nürnberger T, Joosten MHAJ. Of PAMPs and Effectors: The Blurred PTI-ETI Dichotomy. The Plant Cell. 2011;23(1):4-15.
91. Poschenrieder C, Tolrà R, Barceló J. Can metals defend plants against biotic stress? Trends in Plant Science. 2006;11(6):288-95.
92. Liu G, Greenshields DL, Sammynaiken R, Hirji RN, Selvaraj G, Wei Y. Targeted alterations in iron homeostasis underlie plant defense responses. Journal of Cell Science. 2007;120(4):596-605.
93. Dutton MV, Evans CS. Oxalate production by fungi: its role in pathogenicity and ecology in the soil environment. Canadian Journal of Microbiology. 1996;42(9):881-95.
94. Yang J, Tewari JP, Verma PR. Calcium oxalate crystal formation in Rhizoctonia solani AG 2-1 culture and infected crucifer tissue: relationship between host calcium and resistance. Mycological Research. 1993;97(12):1516-22.
95. Ma W, Berkowitz GA. The grateful dead: calcium and cell death in plant innate immunity. Cellular Microbiology. 2007;9(11):2571-85.
96. Williams B, Kabbage M, Kim H-J, Britt R, Dickman MB. Tipping the Balance: Sclerotinia sclerotiorum Secreted Oxalic Acid Suppresses Host Defenses by Manipulating the Host Redox Environment. PLOS Pathogens. 2011;7(6):e1002107.
97. Donner E, Punshon T, Guerinot ML, Lombi E. Functional characterisation of metal(loid) processes in planta through the integration of synchrotron techniques and plant molecular biology. Anal Bioanal Chem. 2012;402(10):3287-98.

98. Kopittke PM, Punshon T, Paterson DJ, Tappero RV, Wang P, Blamey FPC, et al. Synchrotron-Based X-Ray Fluorescence Microscopy as a Technique for Imaging of Elements in Plants. Plant Physiol. 2018;178(2):507-23.
99. van der Ent A, Przybyłowicz WJ, de Jonge MD, Harris HH, Ryan CG, Tylko G, et al. X-ray elemental mapping techniques for elucidating the ecophysiology of hyperaccumulator plants. New Phytol. 2018;218(2):432-52.
100. Rodrigues ES, Gomes MHF, Duran NM, Cassanji JGB, da Cruz TNM, Sant'Anna Neto A, et al. Laboratory Microprobe X-Ray Fluorescence in Plant Science: Emerging Applications and Case Studies. Frontiers in Plant Science. 2018;9.
101. Kawakami Y, Bhullar NK. Potential Implications of Interactions between Fe and S on Cereal Fe Biofortification. International Journal of Molecular Sciences. 2020;21(8):2827.
102. Cheah ZX, O'Hare TJ, Harper SM, Bell MJ. Variation in zinc concentration of sweetcorn kernels reflects source-sink dynamics influenced by kernel number. Journal of experimental botany. 2020;71(16):4985-92.
103. Wang P, Menzies NW, Lombi E, McKenna BA, de Jonge MD, Donner E, et al. Quantitative determination of metal and metalloid spatial distribution in hydrated and fresh roots of cowpea using synchrotron-based X-ray fluorescence microscopy. Sci Total Environ. 2013;463-464:131-9.
104. Li C, Wang L, Wu J, Blamey FPC, Wang N, Chen Y, et al. Translocation of Foliar Absorbed Zn in Sunflower (Helianthus annuus) Leaves. Frontiers in Plant Science. 2022;13.
105. Punshon T, Paterson D, Tappero R, Wang P, Blamey P, Ent A, et al. Synchrotron-Based X-Ray Fluorescence Microscopy as a Technique for Imaging of Elements in Plants. Plant physiology. 2018;178.
106. Balerna A, Mobilio S. Synchrotron Radiations: Basics, Methods and Applications. Introduction to synchrotron radiation Springer, Berlin. 2015;799.
107. Wiedemann H. Synchrotron radiation. Particle Accelerator Physics: Springer; 2003. p. 647-86.
108. Mobilio S, Boscherini F, Meneghini C. Synchrotron Radiation: Springer; 2016.
109. Howard DL, de Jonge MD, Afshar N, Ryan CG, Kirkham R, Reinhardt J, et al. The XFM beamline at the Australian Synchrotron. Journal of Synchrotron Radiation. 2020;27(5):1447-58.

110. Wallwork KS, Kennedy BJ, Wang D, editors. The high resolution powder diffraction beamline for the Australian Synchrotron. AIP Conference Proceedings; 2007: American Institute of Physics.
111. Thomlinson W, Berkvens P, Berruyer G, Bertrand B, Blattmann H, Brauer-Krisch E, et al. Research at the European Synchrotron Radiation Facility medical beamline. Cellular and molecular biology (Noisy-le-Grand, France). 2000;46(6):1053-63.
112. Carr G, Smith R, Mihaly L, Zhang H, Reitze D, Tanner D. High-resolution far-infrared spectroscopy at NSLS beamline U12IR. Infrared physics & technology. 2008;51(5):404-6.
113. Plathe R, Martin D, Tobin M, Puskar L, Appadoo D, editors. The far-infrared/thz beamline at the Australian Synchrotron: Performance & applications. 2011 International Conference on Infrared, Millimeter, and Terahertz Waves; 2011: IEEE.
114. Willmott P. An Introduction to Synchrotron Radiation: Techniques and Applications. 2011:341-52.
115. Brown TL. Chemistry: the central science: Pearson Education; 2009.
116. Wiedemann H. Synchrotron Radiation Physics. In: Jaeschke EJ, Khan S, Schneider JR, Hastings JB, editors. Synchrotron Light Sources and Free-Electron Lasers: Accelerator Physics, Instrumentation and Science Applications. Cham: Springer International Publishing; 2016. p. 3-49.
117. Boldeman JW, Einfeld D. The physics design of the Australian synchrotron storage ring. Nuclear Instruments and Methods in Physics Research Section A: Accelerators, Spectrometers, Detectors and Associated Equipment. 2004;521(2):306-17.
118. Willmott P. Synchrotron physics. An Introduction to Synchrotron Radiation. 2011:39-86.
119. Margaritondo G. Characteristics and properties of synchrotron radiation. Synchrotron Radiation: Springer; 2015. p. 29-63.
120. Thompson RQ. Encyclopedia of Analytical Science, Second Edition (Worsfold, Paul; Tonshend, Alan; Poole, Colin). Journal of Chemical Education. 2005;82(9):1313.
121. Eichert D. X-ray Microscopy. Synchrotron Radiation: Springer; 2015. p. 409-36.

122. Pushie MJ, Pickering IJ, Korbas M, Hackett MJ, George GN. Elemental and Chemically Specific X-ray Fluorescence Imaging of Biological Systems. Chemical Reviews. 2014;114(17):8499-541.
123. Hare DJ, New EJ, de Jonge MD, McColl G. Imaging metals in biology: balancing sensitivity, selectivity and spatial resolution. Chemical Society Reviews. 2015;44(17):5941-58.
124. Van Grieken R. X-ray fluorescence spectrometry and related techniques: an introduction2013.
125. Szczerbowska-Boruchowska M. Sample thickness considerations for quantitative X-ray fluorescence analysis of the soft and skeletal tissues of the human body–theoretical evaluation and experimental validation. X-Ray Spectrometry. 2012;41(5):328-37.
126. Adams F. X-ray fluorescence and emission-synchrotron X-ray fluorescence. Encyclopedia of analytical science: vol 9/Worsfold, Paul J[edit]2005. p. 458-63.
127. Margui E, Van Grieken R. X-ray fluorescence spectrometry and related techniques: an introduction: Momentum press; 2013.
128. Skoog DA, Holler FJ, Crouch SR. Principles of instrumental analysis: Cengage learning; 2017.
129. Potts PJ. X-RAY FLUORESCENCE AND EMISSION| wavelength dispersive x-ray fluorescence. 2005.
130. Lindon JC, Tranter GE, Koppenaal D. Encyclopedia of spectroscopy and spectrometry: Academic Press; 2016.
131. Bergmann U, Bertrand L, Edwards NP, Manning PL, Wogelius RA. Chemical mapping of ancient artifacts and fossils with X-ray spectroscopy. Synchrotron Light Sources and Free-Electron Lasers: Accelerator Physics, Instrumentation and Science Applications. 2020:2393-455.
132. Kanngießer B, Malzer W, Mantouvalou I, Sokaras D, Karydas A. A deep view in cultural heritage—confocal micro X-ray spectroscopy for depth resolved elemental analysis. Applied Physics A. 2012;106(2):325-38.
133. See PT, Marathamuthu KA, Iagallo EM, Oliver RP, Moffat CS. Evaluating the importance of the tan spot ToxA–Tsn1 interaction in Australian wheat varieties. Plant Pathology. 2018;67(5):1066-75.

134. Moffat CS, See PT, Oliver RP. Generation of a ToxA knockout strain of the wheat tan spot pathogen P yrenophora tritici-repentis. Mol Plant Pathol. 2014;15(9):918-26.
135. Scouten CW, Cunningham M. Freezing biological samples. Microscopy Today. 2006;14(1):48-.
136. Jehl B, Bauer R, Dörge A, Rick R. The use of propane/isopentane mixtures for rapid freezing of biological specimens. Journal of Microscopy. 1981;123(3):307-9.
137. Sakura. Tissue-Tek O.C.T Compound Safety Data Sheet. 2008.
138. Ryu M, Balčytis A, Wang X, Vongsvivut J, Hikima Y, Li J, et al. Orientational mapping augmented sub-wavelength hyper-spectral imaging of silk. Scientific reports. 2017;7(1):1-10.
139. Summers KL, Fimognari N, Hollings A, Kiernan M, Lam V, Tidy RJ, et al. A multimodal spectroscopic imaging method to characterize the metal and macromolecular content of proteinaceous aggregates ("amyloid plaques"). Biochemistry. 2017;56(32):4107-16.
140. de Jonge MD, Holzner C, Baines SB, Twining BS, Ignatyev K, Diaz J, et al. Quantitative 3D elemental microtomography of *Cyclotella meneghiniana* at 400-nm resolution. Proceedings of the National Academy of Sciences. 2010;107(36):15676-80.
141. Wirthensohn M, Sedgley M. Epicuticular Wax Structure and Regeneration on Developing Juvenile *Eucalyptus* Leaves. Australian Journal of Botany. 1996;44(6):691-704.
142. Knight TG, Wallwork MAB, Sedgley M. Leaf Epicuticular Wax and Cuticle Ultrastructure of Four Eucalyptus Species and Their Hybrids. International Journal of Plant Sciences. 2004;165(1):27-36.
143. JEFFREE CE, BAKER EA, HOLLOWAY PJ. ULTRASTRUCTURE AND RECRYSTALLIZATION OF PLANT EPICUTICULAR WAXES. New Phytologist. 1975;75(3):539-49.
144. de Brito PS, Sabedotti C, Flores TB, Raman V, Bussade JE, Farago PV, et al. Light and Scanning Electron Microscopy, Energy Dispersive X-Ray Spectroscopy, and Histochemistry of Eucalyptus tereticornis. Microscopy and Microanalysis. 2021;27(5):1295-303.

145. Guzmán-Delgado P, Fernández V, Graça J, Cabral V, Kayali N, Khayet M, et al. Chemical and structural analysis of Eucalyptus globulus and E. camaldulensis leaf cuticles: A lipidized cell wall region. Frontiers in Plant Science. 2014.
146. Amsbury S, Hunt L, Elhaddad N, Baillie A, Lundgren M, Verhertbruggen Y, et al. Stomatal Function Requires Pectin De-methyl-esterification of the Guard Cell Wall. Curr Biol. 2016;26(21):2899-906.
147. Wu HC, Bulgakov VP, Jinn TL. Pectin Methylesterases: Cell Wall Remodeling Proteins Are Required for Plant Response to Heat Stress. Front Plant Sci. 2018;9:1612.
148. Naika H RN, Bhavana S, Teixeira da Silva J, Lingaraju K, Chandramohan V, V K. In silico and in vivo wound healing studies of ursolic acid isolated from Clematis gouriana against GSK-3 beta. Nusantara Bioscience. 2016;8:232-44.
149. Palu D, Bighelli A, Casanova J, Paoli M. Identification and Quantitation of Ursolic and Oleanolic Acids in Ilex aquifolium L. Leaf Extracts Using 13C and 1H-NMR Spectroscopy. Molecules. 2019;24(23):4413.
150. Annan K, Jackson N, Dickson R, Sam G, Komlaga G. Acaricidal effect of an isolate from Hoslundia opposita vahl against Amblyomma variegatum (Acari: Ixodidae). Pharmacognosy research. 2011;3:185-8.
151. Samuels L, Kunst L, Jetter R. Sealing plant surfaces: cuticular wax formation by epidermal cells. Annual review of plant biology. 2008;59(1):683-707.
152. Steinbauer MJ, Davies NW, Gaertner C, Derridj S. Epicuticular waxes and plant primary metabolites on the surfaces of juvenile Eucalyptus globulus and E. nitens (Myrtaceae) leaves. Australian Journal of Botany. 2009;57(6):474-85.
153. Shimojima M, Ohta H. Critical regulation of galactolipid synthesis controls membrane differentiation and remodeling in distinct plant organs and following environmental changes. Progress in lipid research. 2011;50(3):258-66.
154. Chan KA, Kazarian SG. Attenuated total reflection Fourier-transform infrared (ATR-FTIR) imaging of tissues and live cells. Chemical Society Reviews. 2016;45(7):1850-64.
155. Dubois M, Van den Broeck L, Inzé D. The pivotal role of ethylene in plant growth. Trends in plant science. 2018;23(4):311-23.
156. Abeles FB, Morgan PW, Saltveit Jr ME. Ethylene in plant biology: Academic press; 2012.

157. Willick IR, Lahlali R, Vijayan P, Muir D, Karunakaran C, Tanino KK. Wheat flag leaf epicuticular wax morphology and composition in response to moderate drought stress are revealed by SEM, FTIR-ATR and synchrotron X-ray spectroscopy. Physiologia plantarum. 2018;162(3):316-32.
158. Vijayan P, Willick IR, Lahlali R, Karunakaran C, Tanino KK. Synchrotron radiation sheds fresh light on plant research: the use of powerful techniques to probe structure and composition of plants. Plant and Cell Physiology. 2015;56(7):1252-63.
159. Gierlinger N, Schwanninger M. Chemical imaging of poplar wood cell walls by confocal Raman microscopy. Plant physiology. 2006;140(4):1246-54.
160. Kerr JL, Baldwin DS, Tobin MJ, Puskar L, Kappen P, Rees GN, et al. High spatial resolution infrared micro-spectroscopy reveals the mechanism of leaf lignin decomposition by aquatic fungi. PloS one. 2013;8(4):e60857.
161. Thumanu K, Sompong M, Phansak P, Nontapot K, Buensanteai N. Use of infrared microspectroscopy to determine leaf biochemical composition of cassava in response to Bacillus subtilis CaSUT007. Journal of Plant Interactions. 2015;10(1):270-9.
162. Dokken KM, Davis LC, Marinkovic NS. Use of infrared microspectroscopy in plant growth and development. Applied Spectroscopy Reviews. 2005;40(4):301-26.
163. Zhu X, Zhang Y, Du Z, Chen X, Zhou X, Kong X, et al. Tender leaf and fully-expanded leaf exhibited distinct cuticle structure and wax lipid composition in Camellia sinensis cv Fuyun 6. Scientific reports. 2018;8(1):1-12.
164. Gollnow B, Faragher J, Worrall R, Turton L, Joyce D. Quality specifications for Australian wildflowers and revised manual of postharvest treatments for wildflowers: RIRDC; 2010.
165. Dawson IA, King RW. Effect of environment and applied chemicals on the flowering and form of Geraldton Wax (Chamelaucium uncinatum Schauer). Scientia Horticulturae. 1993;54(3):233-46.
166. McGarry R, Ozga JA, Reinecke DM. The effects of ethephon on saskatoon (Amelanchier alnifolia Nutt.) fruit ripening. Journal of the American Society for Horticultural Science. 2005;130(1):12-7.
167. Norberg O, Mason S, Lowry S. Ethephon influence on harvestable yield, grain quality, and lodging of corn. Agronomy journal. 1988;80(5):768-72.
168. Shekoofa A, Emam Y. Plant growth regulator (ethephon) alters maize (Zea maps L.) growth. J Agron. 2008;7(1):41-8.

169. Li Y, Solomon S. Ethephon: a versatile growth regulator for sugar cane industry. Sugar Tech. 2003;5(4):213-23.
170. Ascough GD, Nogemane N, Mtshali NP, van Staden J, Bornman CH. Flower abscission: environmental control, internal regulation and physiological responses of plants. South African Journal of Botany. 2005;71(3):287-301.
171. Reid A. Diseases of waxflower and their control. 2003.
172. Đinh Q, Joyce D, Irving D, Wearing A. Histology of waxflower (Chamelaucium spp.) flower infection by Botrytis cinerea. Plant Pathology. 2010;60:278-87.
173. Kenea FT. Role of Ethylene in Horticulture–A Review. GP GLOBALIZE RESEARCH JOURNAL OF CHEMISTRY. 2021:81.
174. Sisler EC, Serek M. Inhibitors of ethylene responses in plants at the receptor level: recent developments. Physiologia plantarum. 1997;100(3):577-82.
175. Joyce DC. Postharvest characteristics of Geraldton wax flowers. Journal of the American Society for Horticultural Science. 1988;113(5):738-42.
176. Franceschi VR, Horner HT. Calcium Oxalate Crystals in Plants. Botanical Review. 1980;46(4):361-427.
177. O'Connell AM, Malajczuk N, Gailitis V. Occurrence of calcium oxalate in karri (Eucalyptus diversicolor F. Muell.) forest ecosystems of south western Australia. Oecologia. 1983;56(2-3):239-44.
178. H. Valido I, Resina-Gallego M, Yousef I, Luque-Gálvez MP, Valiente M, López-Mesas M. Calcium oxalate kidney stones, where is the organic matter?: A synchrotron based infrared microspectroscopy study. Journal of Biophotonics. 2020;13(12):e202000303.
179. Erica Donner, Tracy Punshon, Mary Lou Guerinot a, Lombi E. Functional characterisation of metal(loid) processes in planta through the integration of synchrotron techniques and plant molecular biology. Analytical and Bioanalytical Chemistry. 2012;402:3287-98.
180. Dolgova NV, Nehzati S, Choudhury S, MacDonald TC, Regnier NR, Crawford AM, et al. X-ray spectroscopy and imaging of selenium in living systems. Biochimica et Biophysica Acta (BBA)-General Subjects. 2018;1862(11):2383-92.
181. Kopittke PM, Lombi E, Van Der Ent A, Wang P, Laird JS, Moore KL, et al. Methods to visualize elements in plants. Plant Physiology. 2020;182(4):1869-82.

182. Heller A, Witt-Geiges T. Oxalic acid has an additional, detoxifying function in Sclerotinia sclerotiorum pathogenesis. PLoS One. 2013;8(8):e72292.
183. Foster J, Luo B, Nakata PA. An Oxalyl-CoA Dependent Pathway of Oxalate Catabolism Plays a Role in Regulating Calcium Oxalate Crystal Accumulation and Defending against Oxalate-Secreting Phytopathogens in Medicago truncatula. PLoS One. 2016;11(2):e0149850.
184. Arnott HJ. Calcium oxalate in fungi. Calcium oxalate in biological systems: CRC Press; 2020. p. 73-111.
185. Terzano R, Denecke MA, Falkenberg G, Miller B, Paterson D, Janssens K. Recent advances in analysis of trace elements in environmental samples by X-ray based techniques (IUPAC Technical Report). Pure and Applied Chemistry. 2019;91(6):1029-63.
186. Ertl K, Goessler W. Grains, whole flour, white flour, and some final goods: an elememntal comparison. European Food Research and Technology. 2018;244:2065-75.
187. Valdez-Aguilar LA, Reed DW. Influence of Potassium Substitution by Rubidium and Sodium on Growth, Ion Accumulation, and Ion Partitioning in Bean under High Alkalinity. Journal of Plant Nutrition. 2008;31(5):867-83.
188. El-Sheikh AM, Ulrich A, Broyer TC. Sodium and rubidium as possible nutrients for sugar beet plants. Plant physiology. 1967;42(9):1202-8.
189. Xu X, Du X, Wang F, Sha J, Chen Q, Tian G, et al. Effects of Potassium Levels on Plant Growth, Accumulation and Distribution of Carbon, and Nitrate Metabolism in Apple Dwarf Rootstock Seedlings. Frontiers in Plant Science. 2020;11.
190. Bassan P, Byrne HJ, Lee J, Bonnier F, Clarke C, Dumas P, et al. Reflection contributions to the dispersion artefact in FTIR spectra of single biological cells. Analyst. 2009;134(6):1171-5.
191. Bassan P, Lee J, Sachdeva A, Pissardini J, Dorling KM, Fletcher JS, et al. The inherent problem of transflection-mode infrared spectroscopic microscopy and the ramifications for biomedical single point and imaging applications. Analyst. 2013;138(1):144-57.
192. Bassan P, Kohler A, Martens H, Lee J, Byrne HJ, Dumas P, et al. Resonant Mie scattering (RMieS) correction of infrared spectra from highly scattering biological samples. Analyst. 2010;135(2):268-77.

193. Filik J, Frogley MD, Pijanka JK, Wehbe K, Cinque G. Electric field standing wave artefacts in FTIR micro-spectroscopy of biological materials. Analyst. 2012;137(4):853-61.
194. FaAOotU N. Food wastage footprint Full-cost accounting 2014 [Available from: http://www.fao.org/3/a-i3991e.pdf.
195. Lara I, Belge B, Goulao LF. A Focus on the Biosynthesis and Composition of Cuticle in Fruits. Journal of Agricultural and Food Chemistry. 2015;63(16):4005-19.

8.0 Appendix

^{1}H NMR Spectrum (400 MHz, DMSO)

Crude - Fraction 1: Marri Extraction

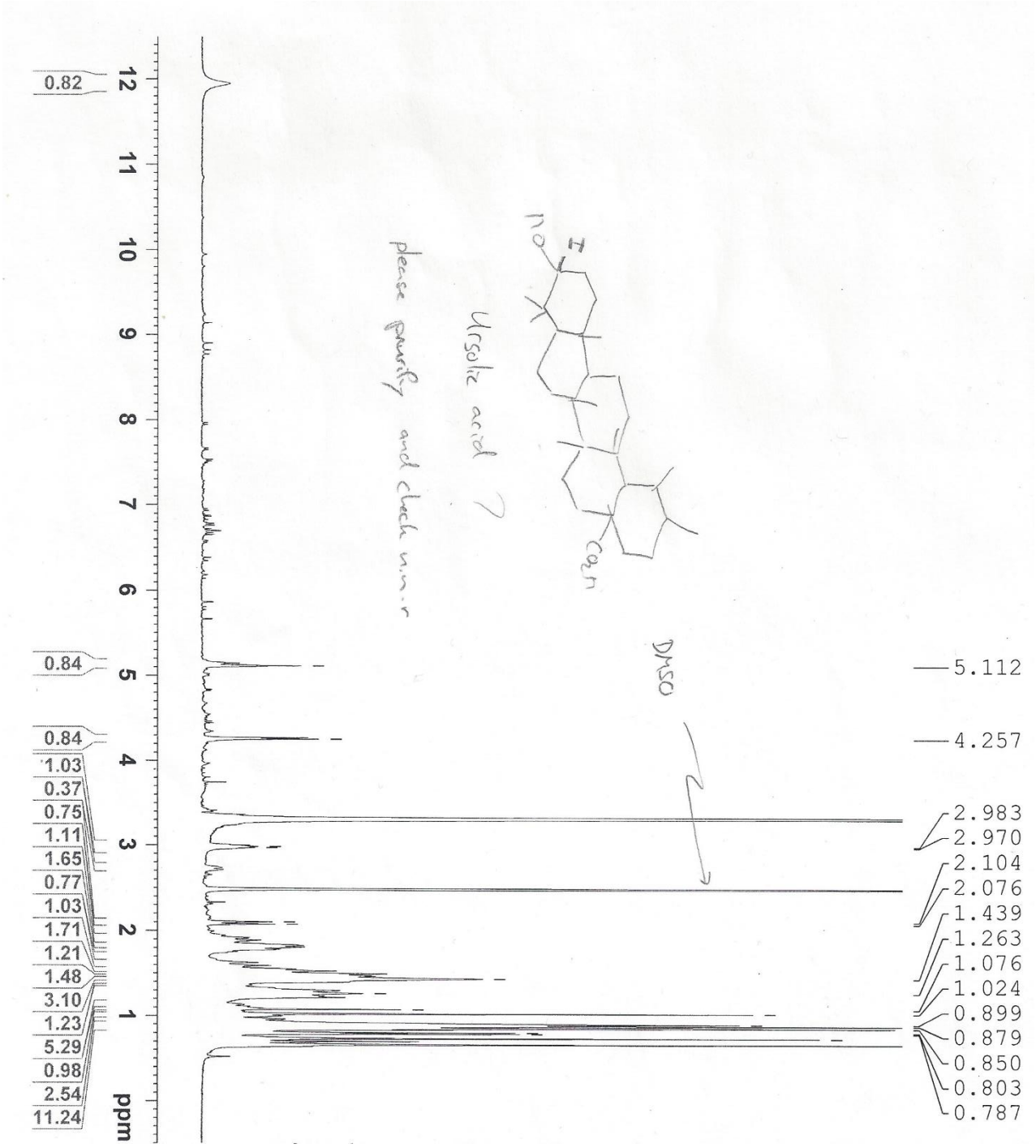

^{1}H NMR Spectrum (400 MH_z, $CDCl_3$)

"Purified" - Fraction 1: Marri Extraction